Responses of Alternating Current Field Measurement (ACFM) to Rolling Contact Fatigue (RCF) Cracks in Railway Rails

by

Jialong Shen

A thesis submitted in partial fulfilment of the requirements for the degree of

Doctor of Philosophy

University of Warwick, Warwick Manufacturing Group (WMG)

January 2017

Table of Contents

List of Figures

List of Tables

Acknowledgements

I would like to express my sincere thanks to Professor Claire Davis, my supervisor, who is always willing to help, to guide and to advise my academic studies. The suggestions she gave lead me to establish a correct and constructive methodology for doing the research; the ideas she gave induce me to always have a critical thinking not only about my project but about everything in everyday life. I am also grateful to Dr Lei Zhou, my co-supervisor, for his demonstration of the experiment and the modelling; for his analysis skills and feedback through all of my project; and more importantly the encouragement and confidence when needed.

To Dr Hamed Rowshandel and Dr Gemma Nicholson in University of Birmingham, who have been a supportive influence and shared their valuable knowledge to my research, which are importance to my success.

I would also like to acknowledge to Dr Jay Warnett and Professor Mark Williams for the help doing X-ray tomography and analysing the result. My special thanks also go to Eric Magel for the provision of rail sample and to TSC Inspection System, UK for constructive technical discussion and provision of equipment.

Tanks must go to Chinese Scholarship Council (CSC) for providing the great opportunity for me to study PhD in UK and supporting me with living expenses.

Thanks also go to all of my friends and colleagues at the University of Warwick and University of Birmingham: Carl, Jun, Jacky, Daniel, Fei, Mo, Mohsen and Will for kindly helps and enjoy days we have been through together.

Finally, I would like to thank my parents for endless understanding and tolerance. Without my parents supports I would never be able to finish my PhD and to write the thesis right now. Most of all, to my wife Hongyu Wang, thank you for enlightening me with different perspectives and thank you for taking care of my life.

Declaration

This thesis is submitted to the University of Warwick in partial fulfilment of the requirements for the degree of Doctor of Philosophy.

The author declares that except where acknowledged, the work contained in this thesis is his own work and has not been submitted for a degree at any other university.

Parts of this thesis have been and will be published by the author:

1. J. Shen, L. Zhou, J. Warnett, et al. The influence of RCF crack propagation angle and crack shape on the ACFM signal. 19th World Conference on Non-Destructive Testing, 2016. Munich, Germany.

2. J. Shen, L. Zhou, H. Rowshandel, G. Nicholson, C. Davis. Determining the propagation angle for non-vertical surface-breaking cracks and its effect on crack sizing using an ACFM sensor, Measurement Science and Technology. 2015, 26 (11): 115604.

3. J. Shen, L. Zhou, G.L. Nicholson, H. Rowshandel, C.L. Davis. An assessment of the ACFM response to the propagation angle of RCF cracks in rail, The 54th Annual Conference of BINDT Telford, UK, 2015.

4. J. Shen, L. Zhou, G.L. Nicholson, H. Rowshandel, C.L. Davis. Predicting RCF crack depths in rails taking into account multiple cracks and modelling for cracks length and vertical angle, under preparation for Proceedings of the Institution of Mechanical Engineers, Part F: Journal of Rail and Rapid Transit.

Abstract

Rolling contact fatigue (RCF) cracks are a widespread problem that impairs the service life of railway rails and wheels, with an associated high cost of labour and capital expenditure for remediation. Severe RCF cracks cause serious safety issues as they can turn down at a larger propagation angle into the rail potentially leading to a rail break. Rail grinding can effectively eliminate RCF cracks if they are detected when they are small enough to be removed. Alternating current field measurement (ACFM) is one of the electromagnetic (EM) techniques that can be used for defect detection and sizing in the rail industry. ACFM has been reported to be more accurate in providing length and depth information than conventional UT for small RCF cracks and is less sensitive to lift-off than eddy current methods.

The aim of the present research is to analyse the response of ACFM signals to single and multiple RCF cracks in railway rails using experimental measurements and FE based modelling tools, focusing on the influences of crack vertical angle and multiple cracks (number, spacing, size, uniformity) on the ACFM signal to improve the accuracy of dimension predictions.

A novel method (using the Bz signal) is proposed to determine the vertical angle of the RCF cracks, which then allows the crack vertical depth to be determined from the pocket length (standard output from ACFM measurements) and therefore the appropriate amount of rail grinding to remove the RCF cracks. It was found that the vertical angle influences the pocket length determined from the measured $\Delta Bx_{max}/Bx$ value when the cracks are shallow (vertical angles < 30°), therefore greater accuracy can be obtained when compensating the $\Delta Bx_{max}/Bx$ value using the determined vertical angle. It is shown that the variations of crack surface length, crack inner spacing and crack number for multiple cracks also influence the $\Delta Bx_{max}/Bx$ values determined for multiple cracks. The influences of asymmetrical crack shapes on crack sizing are discussed, in general it has been found that for accurate sizing of RCF cracks using a single ACFM scan the cracks should be regular, where the assumption of semi ellipse shapes is appropriate.

The methods developed in the project were assessed using calibration samples (machined cracks with different sizes and vertical angles) and rails removed from service containing single and multiple RCF cracks. It was found that the new approach proposed in this work allowed the vertical angle to be predicted well for single and multiple RCF cracks (difference to measurements < 14.3 %). In addition the error in pocket length prediction is greatly decreased when using the sizing method including compensation determined from the crack vertical angle.

List of Abbreviations

ACFM	Alternating Current Field Measurement
ACPD	Alternating Current potential drop
ADC	Analogue to Digital Conversion
AE	Acoustic Emission
ATQ	Acoustic Track Quality
ECML & WCML	East and West Coast Mainlines
ECM	Electrochemical Machining
EDM	Electrical Discharge Machining
EM	Electromagnetic
EMATs	Electromagnetic Acoustic Transducers
ERB	Earth Return Brush
FEM	Finite Element Method
FMB	Full Mesh Boundary
GCC	Gauge Corner Cracking
HC	Head Checking
IB	Impedance Boundary
MFL	Magnetic Flux Leakage
MPI	Magnetic Particle Imaging
NDT	Non-destructive Testing
PA	Phased Array
PL	Pocket Length
PoD	Probability of Detection
RASCAL	Rail Surface Condition Alert
RCF	Rolling Contact Fatigue
RSSB	Rail Safety & Standards Boards
SCC	Stress Corrosion Cracking
SL	Surface Length
SMFM	Surface Magnetic Field Measurement
SNCF	National society of French railways
UCL	University College London
UT	Ultrasonic Testing

VA	Vertical angle
VD	Vertical Depth
VI	Visual Inspect
VIS	Visual Inspection System
WEL	White Etching Layer
WLRM	Whole Life Rail Model
1-D	One Dimensional
2-D	Two Dimensional
3-D	Three Dimensional

1. Introduction

1.1 Background

Rolling contact fatigue (RCF) cracks are a widespread problem that impairs the service life of railway rails and wheels, with an associated high cost of labour and capital expenditure for remediation [1, 2]. RCF cracks initiate on the surface of rails, propagating at shallow angles into the rail where, at a characteristic depth, they can turn down potentially leading to the rail failure [3]. The economic cost of rail fatigue fracture amounts up to 2 billion euros per year in the European Union alone [2]. Extensive research has been carried out on RCF mitigation in the UK since 2000, after the Hatfield derailments, caused by RCF cracks, resulted in casualties and economic loss exceeding £1 billion [4].

With the increase of axle load and train speed, RCF cracks are and will continue to be a major cause for, from a railway maintenance point of view, rail grinding [5]. Rails are regularly inspected using various non-destructive testing (NDT) techniques (e.g. visual, ultrasonic and electromagnetic) for defect detection and sizing before rail grinding is carried out. Visual inspection (VI) is a widely used NDT approach in the rail industry, where an experienced rail inspector walks along the rail track to assess the surface condition subjectively by eye and the visibility of surface breaking defects can be enhanced by dye penetrant or magnetic particle imaging (MPI). With the development of photography and image processing technology, various visual camera-based inspection systems have been installed on trains for crack detection, missing component detection and corrugation inspection [6, 7].

Ultrasonic testing (UT) is the most frequently used NDT technique either employed on an inspection train/vehicle or mounted on a manually operated trolley, known as Sperry Sticks in the rail industry [8]. Conventional UT sensors have a relatively low probability of detection (PoD) for surface-breaking or sub-surface cracks and multiple transducers need to be employed at various angles to enhance detection of surface-breaking and near-surface defects [9]. New techniques (e.g. ultrasonic phased arrays, laser ultrasonics, long-range ultrasonics, etc.) based on ultrasound have been also developed and used for rail inspection to maximise the possibility of crack detection and sizing [10-12].

Electromagnetic (EM) based NDT, for example magnetic flux leakage (MFL) and eddy current (EC) methods are usually employed in the test trains as a complementary technique to UT [8, 13]. These hybrid systems are superior when inspecting for surface-breaking or sub-surface cracks in comparison to UT in isolation. However the MFL signal is sensitive to the train speed and is adversely influenced by noise signals when the speed exceeds 32 km/h [8]; the eddy current technique is strongly affected by the sensor lift-off and this means that EC sensors need to be installed at a close and constant position to the rail surface [14].

Alternating current field measurement (ACFM) is an electromagnetic technique developed in the UK for crack detection and sizing. ACFM can provide information on the surface length and depth of small cracks and it relatively insensitive to lift-off variations allowing detection through coating, paint or contamination [15]. ACFM sensors are already used in a walking stick system for rail inspection and have also been reported to show the capability to make measurements when moving at high speed over a rail [16, 17]. Whilst crack detection and sizing can be carried out for single cracks, and some empirical correlations have been developed for multiple cracks further work is required to improving these approaches.

1.2 Motivation

RCF cracks usually initiate at the rail surface, caused by the lateral and longitudinal traction between rails and wheels from repeated loading. This results in RCF cracks propagating at a shallow angle (normally less than 30°) into the rail [3, 18, 19], known as the vertical angle as shown in Figure 1.1, until they reach a critical depth (typically around 5 mm) before turning down at a larger vertical angle and potentially leading to a rail break. They also extend at an angle to the rail running direction, the horizontal angle, typically occurring at about 30°-75° [1, 3, 20]. RCF cracks usually present in the form of clusters, with a range of spacings (0.8-20 mm) between individual cracks in a cluster [3, 20].

Despite the fact that significant research has been carried out to study the RCF crack dimensions and its relationship with ACFM signals [3, 20-22], there are still several aspects that cannot be determined, for example the vertical propagation angle cannot be measured. From a rail maintenance point of view, it is more important to know the crack vertical depth, which varies depending on the crack vertical angle and crack pocket length (as shown in Figure 1.1), as this determines the amount of rail to be ground off to eliminate the RCF cracks before they grow to a severe size.

In addition, RCF cracks often appear in the form of clusters with cracks that are closely spaced, leading to an interaction between ACFM signals from each crack. Sizing for crack clusters using an algorithm based on ACFM predictions for single cracks inevitably leads to errors [21]. The relationships between ACFM signals and multiple cracks are not fully understood. To improve the ACFM capability for multiple cracks inspection, the response of ACFM signals to the variations of crack surface length, crack spacing, crack number and crack vertical angle should be investigated.

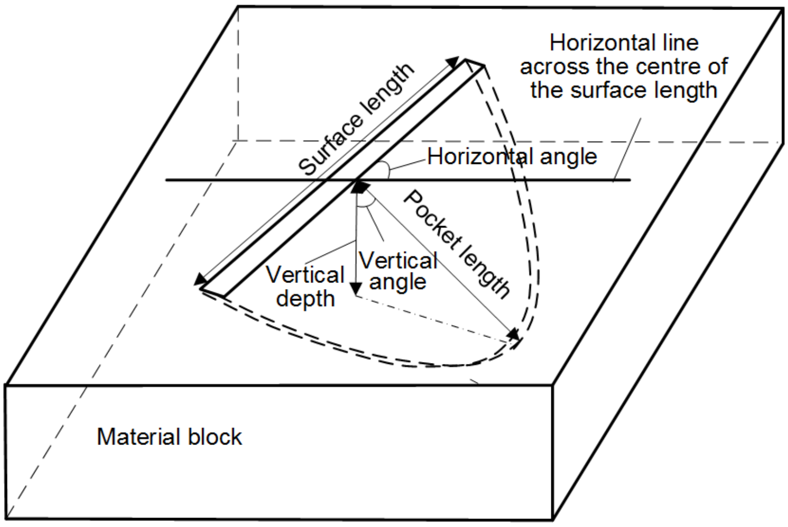

Figure 1.1 Schematic diagram of a single semi-elliptical surface-breaking crack propagating at an angle (vertical angle) into the material.

1.3 Aims and objectives

The aim of the present research is to analyse the response of ACFM signals to single and multiple RCF cracks in railway rails using experimental measurements and modelling. The research focuses on the influence of crack vertical angle and multiple cracks on the ACFM signal to improve the accuracy of dimension predictions for RCF cracks. The main objectives of the research are as following:

- Modelling the response of ACFM signals to variations in vertical angle of RCF cracks using an FEM model [23] and establishing the relationship between the ACFM signals and crack vertical angle.
- Measuring single calibration cracks with different vertical angles using a commercial ACFM probe sensor (TSC Inspection Systems) to verify the modelling results.
- Modelling the response of ACFM signals to the variations in crack surface length, crack inner spacing, crack number and crack vertical angle for uniformly sized crack clusters; investigating the influence of non-uniformly sized cracks in clusters on ACFM signals.
- Measuring calibration samples containing multiple cracks with different crack arrangements using a commercial ACFM probe sensor (TSC Inspection Systems) to verify the modelling results.
- Case study on dimension prediction of single and multiple RCF cracks in railhead samples taken from service; compare and analyse the predicted and actual dimensions through destructive inspection (i.e. X-ray tomography and progressive milling), thus giving suggestions to improve real rail inspection using ACFM sensors.

1.4 Thesis structure

The structure of the present thesis is summarised as follow:

Chapter 1 provides a brief background of the research, including the requirement of RCF crack inspection and NDT techniques used in rail inspection. The motivation of the research and the aim and objectives are also given in this chapter.

Chapter 2 contains a literature review on RCF in rails and NDT techniques currently used for rail inspection both in industrial context and in academic research.

Emphasis is placed on the introduction of the ACFM technique and its application for crack detection both in modelling and experimental research.

Chapter 3 presents the modelling and experimental procedure used in the project. It describes the FEM model and assumptions used in this study, and introduces the samples used for calibrations and in the case study. The experimental procedure, including manual/robotic measurements and destructive inspection, are also presented with the analysis methods.

Chapter 4 presents the results of the study about the influences of the crack vertical angle on ACFM signals. The influences of crack vertical angle on Bx and Bz signals are analysed and the method of using the Bz signal to determine the vertical angle of RCF cracks is proposed.

Chapter 5 gives the results of ACFM response to uniformly sized RCF crack clusters. The relationships between the Bx signals with the variations in crack surface length, crack inner spacing, crack number and crack vertical angle for crack clusters are investigated. The influences of crack shapes on ACFM signals are also presented in this chapter.

Chapter 6 discusses the ACFM responses to non-uniformly sized crack clusters (uniformly sized crack cluster with the middle crack being larger), which represents the crack arrangement in the sample take from service. The ACFM responses to the variations in crack surface length, crack spacing and crack number are modelled and investigated.

Chapter 7 presents case studies of using ACFM signals to predict the dimensions of single and multiple RCF cracks on railhead samples taken from service. The predicted results are analysed in comparison to the actual dimensions, obtained through destructive inspections. Suggestions to improve the capability of ACFM sensors for RCF cracks sizing are proposed.

Chapter 8 presents the conclusions and key findings of the present research. The implications of the results are considered.

Chapter 9 presents the further work to improve the accuracy of ACFM prediction and its applications in the rail industry are also addressed.

2. Literature review

2.1 RCF initiation and propagation

RCF cracks initiate and propagate in rails due to a combination of various factors: loading from vehicle wheels, e.g. bending stresses, wheel-contact stresses, shear stresses; rail lay-out and rail geometry, e.g. high and low rails, curve diameter; rail metallurgy, e.g. inclusions, hardness; and operating conditions, e.g. temperature, lubrication, humidity [24-26]. Any irregularities in the form of stresses acting on the rails, locally exceeding the material ductile limit, can accelerate the propagation of RCF cracks [27]. The rail maintenance strategy (rail inspection and grinding) is also involved with the formation and propagation of RCF cracks. The crack propagates into the rail at a certain rate (magic wear rate [28]) then the loss of metal by both natural wear and grinding must be at least equal to this rate so that the crack can be removed [4]. Despite improvements in steel manufacture and railway maintenance to ensure the rail steel quality and defects removal, RCF is still a critical problem due to the increasing requirements of rail speed and axle load on the UK rail system [29].

The resultant of high stresses between rail and wheel deforms the microstructure at the rail surface and sub-surface in the direction of the applied stress, with repeated loading, unloading and changing stresses [30]. This plastic deformation can accumulate until the ductility is exhausted; in rails with a microstructure of pro-eutectoid ferrite and pearlite this often results in higher strains in the pro-eutectoid ferrite which initiates cracking, as shown in Figure 2.1 [27, 31-33]. Although the resistance of the rail steel to deformation is progressively increasing due to the work hardening caused by the strains, it is not enough to prevent crack formation and therefore, it is the properties developed in the work hardened rail that governs the resistance to RCF cracks [1, 34-36].

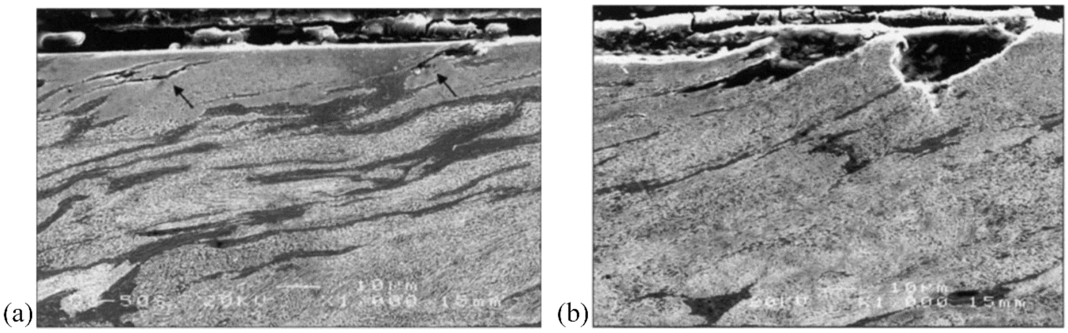

Figure 2.1 SEM images of a sectioned rail sample taken from service showing (a) microstructure having been plastically deformed under the rail surface with cracks initiated along thin and strained ferrite bands (arrowed); (b) detail of RCF cracks and subsequent surface micro-spalling [27].

Railway rails are subjected to highly complex loading conditions. A brief review of the loadings and stresses in rails is introduced below so that the stresses causing RCF crack initiation and propagation can be identified and discussed.

2.1.1 Bending stresses

The bending stress consists of vertical and lateral components corresponding to the vertical and the lateral loadings from the wheel, respectively [37]. The bending stress induced by the lateral force contributes to RCF but the bending stresses caused by the vertical loading dominate the later stages of fatigue crack growth and hence rail failure [25]. The vertical loading comes from the static axle load, which is normally 8-22.5 tonnes, and it is magnified due to the dynamic effect of a moving train. The motion of the sleepers, the weight of the rails, defects and irregularities in the running interface also influence the magnitude of the bending stress [38].

The bending stress can be computed based on the beam-on-elastic-foundation theory, which indicates that the maximum tensile stress at the rail surface occurs at a distance from the wheel position, rather than in the contact area with the wheel, a phenomenon designated as reverse bending. Figure 2.2 illustrates the stress state in a longitudinal section of a rail with a wheel rolling on it [39].

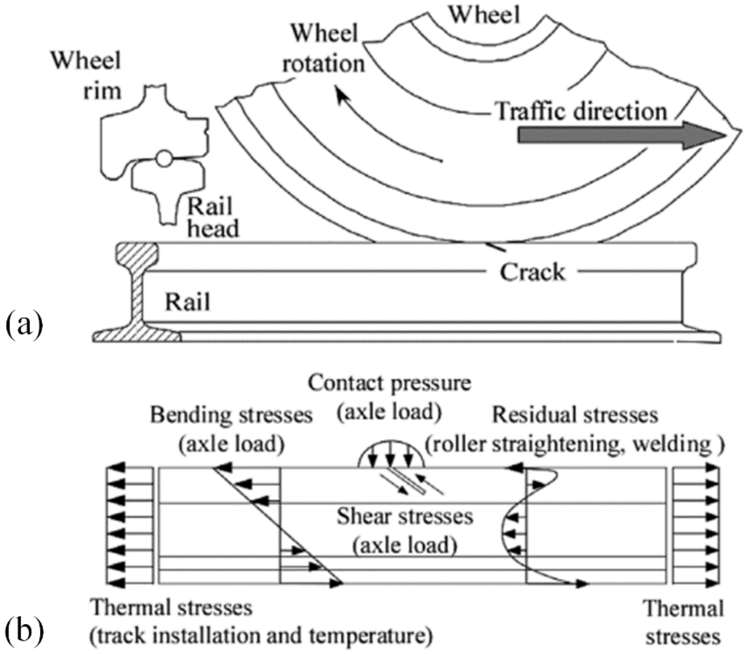

Figure 2.2 (a) Schematic diagram of a wheel rolling over a rail showing the movement direction and the crack propagation; (b) the stress distributions of bending, shear, contact stresses and bulk stresses in the longitudinal section of the rail [39].

A modelling study on growth of multiple RCF cracks driven by rail bending was carried out using the boundary element technique [40]. The study focused on the interaction between adjacent cracks that were at the beginning of the propagation phase caused by the bending stress. The multiple cracks usually show less stress intensity factors (40-55%) compared to the value predicted for a single crack. For multiple cracks, the area between adjacent cracks is usually relieved of stress in the running direction but the rail material at both ends of the multiple cracks can be highly stressed. The stresses between cracks are too low to drive the growth of cracks as the material is discontinuous and the stress is unable to transfer between adjacent cracks. However, this conclusion is only achieved in the consideration of a single bending stress being presented. The contact stresses between rail-wheel, the inclusions in the rail material and the residual stresses can contribute to the initiate and propagation of RCF cracks.

2.1.2 Shear stresses

Shear stress is generated in the contact area at the interface between the rail and the wheel as a result of the rail/wheel traction. Due to the acceleration and deceleration, for train starts and stops, a small relative slip, i.e. creep, between the rail and wheel is generated in the axial direction of the rail, while the lateral movement of the wheel gives transverse creep during the train curving or hunting [38].

These creep forces or traction can facilitate RCF formation as they generate high tangential stresses between the rail and train interface layer, which is a mixture of rust, dust, wear debris and environmental contaminants. Controlling the traction is therefore a process of interfacial layer optimization and creep minimizing [32]. The traction force is governed by the vertical loading from the wheel and the friction coefficient of the interface. It can be dramatically reduced by using a lubricant at the interface, compared to a dry surface, and therefore effectively controls the wear rate of the rail at the rail gauge side. Note that the friction coefficient should be larger than 0.3 at the top of the rail surface to ensure efficient braking and steering [32, 41].

Shear stress is also induced because of the relative movement at the crack surfaces, as shown in Figure 2.2 (b). This plays an important role in vertical crack propagation with a major fracture mode II (shearing mode: a shear stress acting parallel to the plane of the crack and perpendicular to the crack front) as the wheel rolling over the rail surface.

2.1.3 Rail-wheel contact stresses

The forces between the rail and wheel at the contact patch can induce extremely high contact stresses that dominate the formation of the surface-breaking RCF cracks and the early stage of crack propagation. A RCF crack initiates at the rail surface and its propagation can roughly follow two stages, as shown in Figure 2.3 [39]. The cracks initially grow at a shallow angle of 10-40° into the rail at stage 1, where the contact stress field dominates the crack propagation; the crack can change its propagation direction after reaching a critical depth (usually 5 mm [42]) either downwards at a steep angle of 60-80° potentially causing rail break, or upwards to the rail surface causing surface spalling [39]. Note that crack propagation and its size are influenced by the presence of lubricant, water or grease [43, 44].

The rail-wheel contact stresses depend on the dynamic axle loads, contact area profile, presence of welds or other discontinuities, train braking or steering, etc. and it decreases rapidly as the crack propagates in the depth direction. The Hertzian model is the most well-known calculation for the wheel-rail contact stresses, which was established based on elastic contact. It accurately describes the local stresses for the most common wheel-rail contact problems in terms of the Hertzian contact, conformal contact, non-Hertzian elastic contact, elastoplastic contact and the influence of roughness [45-49]. The rail-wheel contact stresses are decided by the wheel diameter, the wheel load, the transverse rail profile and the transverse wheel profile. Doubling of the wheel load, for example, can increase the contact stress by 27 % and a tripling of load increases the contact stress by 44 % [32].

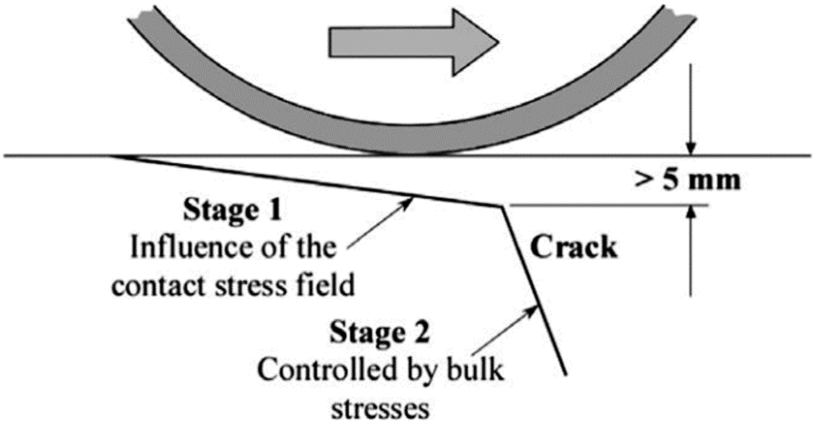

Figure 2.3 Schematic diagram showing two stages of RCF crack propagation, governed by contact stresses and bulk stresses, respectively.

In the UK, a Whole Life Rail Model (WLRM) [50, 51], funded by the Rail Safety & Standards Boards (RSSB), was developed to understand and predict the various stages of RCF crack growth from early surface initiation, shallow growth and final vertical growth. The model can analyse the rail-wheel forces and vehicle behaviours through site-specific dynamic simulations for a range of vehicle and wheel profiles; the magnitude of the critical forces responsible for generating RCF can also be obtained. The model can be used to determine the rail inspection intervals by evaluating the interaction between the wear and RCF crack growth and if the crack has not yet initiated, the model can be used to assess the likelihood of crack initiation, based on an algorithm that RCF and wear are functions of the Contact Patch Energy (each has a different threshold and rate of accumulation) [50-52].

2.1.4 Residual stresses

Residual stresses can be found in any location within the rail due to the manufacturing process and welding of rails during production or in-situ welding during installation in the field and can be high enough to cause rail failure with the presence of cracks [37]. Residual stresses generated during the manufacturing process, because of heating treatment and roller straightening, are generally characterised with tensile residual stress in the railhead and the centre of the rail foot but compressive residual stress is observed in the web and the foot ends. This situation can be altered because the running wheel passing over the rail surface generating plastic deformation, leads to compressive residual stress in the centre of the railhead [46, 53, 54].

Residual stress introduced during rail welding usually presents with compressive stress in the centre of the railhead and tensile stress at the area near the gauge and field sides. The rail web is usually subjected to tensile residual stress while the rail foot is compressed by the welding residual stress [55, 56]. Report [57] shows that rail grinding also contributes to the build-up of residual stresses due to the heat supplied during the maintenance process.

FEM modelling has been carried out to investigate the residual stress state in the rail with consideration of manufacturing process, welding process and loading in service [46, 53, 54, 58]. X-ray and neutron diffraction are also reported as non-destructive methods to measure the residual stresses in rails [59, 60]. Improvements in the manufacturing process (roller straightening) and welding methods in terms of cooling rate have been developed to reduce residual stresses [57, 61].

2.1.5 Thermal stresses

Thermal stresses are generated in rails mainly because of the difference between ambient temperature and the rail neutral temperature (the temperature at which there is no thermal stresses in the rail), which can be set during the rail installation. When the ambient temperature is higher than the neutral temperature, for example during hot days in the summer, the rail is compressed as it is prevented, by adjacent rail sections, from expanding in the axial direction. This stress may be relieved by buckling in the rail with the risk of derailment [25, 39].

When the ambient temperature is lower than the neutral temperature, a tensile thermal stress is induced and it acts as a component of static loading with the wheel loads and residual stresses. Research shows that the tensile thermal stress reaches a maximum in cold winter nights thus increasing the possibility of rail fracture, with the highest rail fracture possibility in the first cold night at the beginning of the winter [25].

2.2 RCF defects in rails

Various defects can occur in the railhead, in the web, in the foot of in-service rail due to: quality control in manufacturing, e.g. kidney defect initiated from hydrogen shatter cracks; inappropriate installation and use, e.g. wheel-burn defect; and exhaustion of the resistance to fatigue damage of the rail steel, e.g. RCF cracks [2, 25]. The defects in rails can be identified according to their position as follow [25]:

- Railhead - typical railhead cracks with surface origin caused by the rolling contact fatigue are gauge corner cracks (head checks), spalling, shelling and squats, as shown in Figure 2.4 [1, 25]; railhead cracks with internal origin are kidney-shaped cracks, as shown in Figure 2.5 [4].

- Rail web - vertical longitudinal cracks (known as piping) and horizontal cracks in the web are usually caused by inappropriate manufacturing; rail web cracks also occur at the fishbolt holes used for rail section joints instead of welding. All these web cracks can lead to rail fracture, as shown in Figure 2.5 [25].

- Rail foot - rail foot cracks can be longitudinal and transverse, as shown in Figure 2.6 [25]. Since the location of rail foot is difficult for inspection these cracks frequently caused rail fracture.

- Welds and switches - modification of material properties happens when rails are welded and welding residual stresses, rail straightness and alignment influence the loading at welds, therefore cracks are easily initiated and propagate at welds, as shown in Figure 2.6 [25]; Cracks at switches are influenced by the geometry of the switch rails with a high possibility of formation at the high bending stresses zone of the switch rail with an asymmetric profile [25].

Improvements in rail quality and management have greatly reduced rail failure caused by inappropriate manufacturing and installation but defects associated with RCF have been increasing over decades due to the high axle load and high train speed, for example causing the Hatfield disaster in 2000 [2, 14]. Although in the network the total number of broken rails decreased from 171 (year 2010/11) to 98 (year 2014/15), the length of rolling contact fatigue cracks in plain line classified as heavy and severe (needs immediately remediation) increased from 438.7 km (year 2009/10) to 793.0 km (year 2014/15) [62]. RCF cracks are of academic and industrial interest in terms of control, inspection and removal.

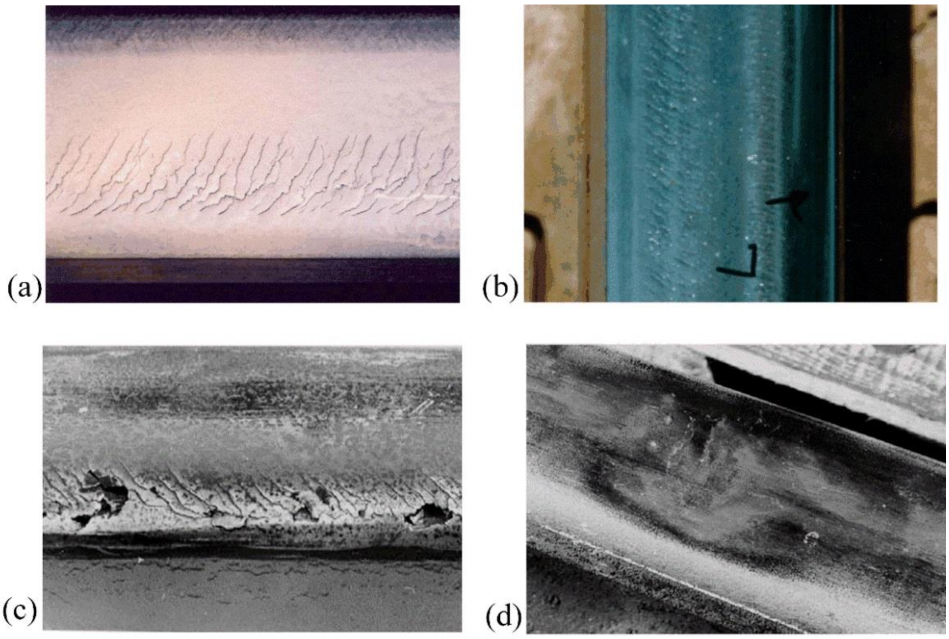

Figure 2.4 Typical RCF defects: (a) and (b) well defined gauge corner cracking and head checking [1]; (c) spalling originating at gauge corner cracks; (d) squat defect on the running surface [25].

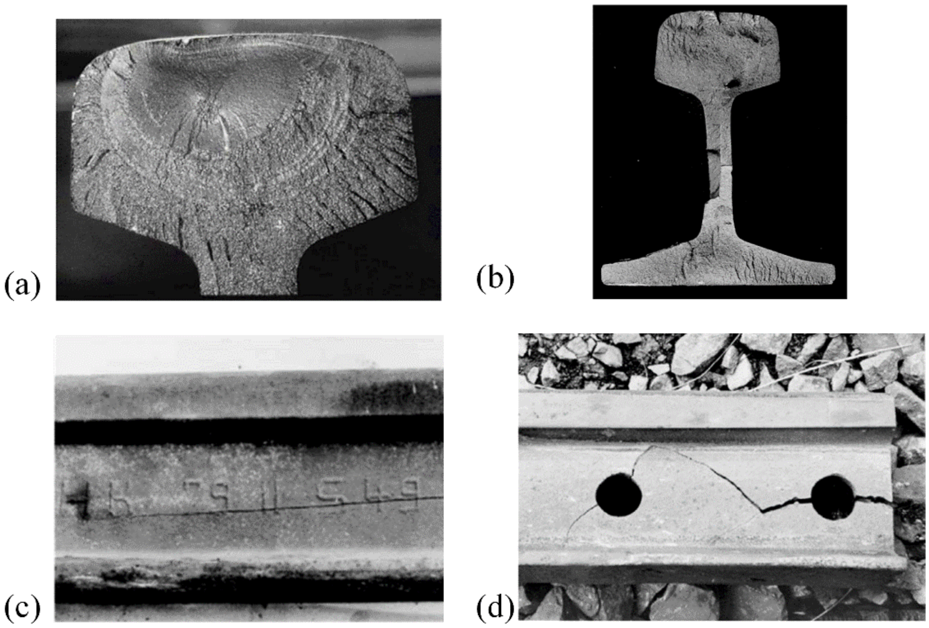

Figure 2.5 (a) Rail fracture caused by the kidney-shaped crack [4]; (b) longitudinal vertical web crack; (c) horizontal web crack; (d) rail web cracks occurring at fishbolt holes [25].

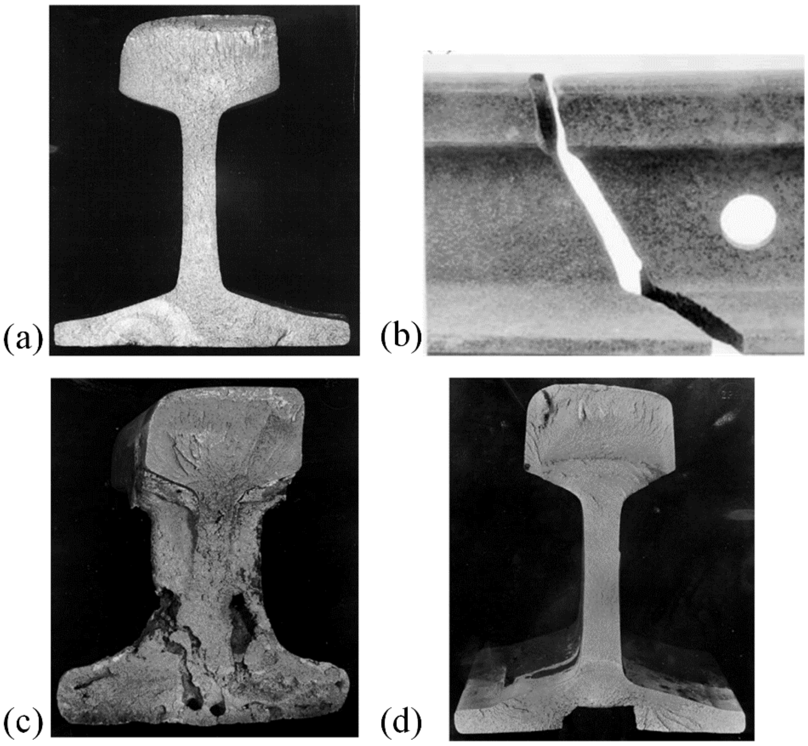

Figure 2.6 (a) Transverse rail foot crack initiating at a corrosion pit; (b) side view of a fracture due to a longitudinal crack in the foot; (c) fracture of an alumina-thermite weld due to the weld crack in the foot; (d) fracture caused by a crack initiated at a cutout in the foot [25].

2.2.1 Gauge corner cracking (head checking)

Gauge corner cracking (GCC) or head checking (HC) are names for surface-breaking RCF cracks that appear at the gauge corner of the railhead, mostly for the outer rails of curves or sometimes on tangent rails, as described in section 1.2 and shown in Figure 2.4 [1]. These fine and regularly spaced cracks are dangerous to the integrity of the rail, as they can steeply turn into the rail causing transverse cracks, which potentially lead to fracture of the rail; or they can propagate upward, sometimes connecting with adjacent cracks, to cause spalling. They always propagate in the direction of plastic deformation in the subsurface when the wheel passes.

A simple method has been reviewed in [4] to distinguish GCC and HC, referring that surface-breaking cracks originating within an area up to 10 mm from the gauge side are GCC while cracks present further towards the rail crown are HC. In UK, RCF cracks are classified as ‘light’, ’moderate’, ‘heavy’ and ‘severe’ according to the visible crack surface length, as shown in Figure 2.7 [70]. This guidance diagram, used by Network Rail, shows only a general correlation between the crack surface length and the crack vertical depth, therefore, vertical depth cannot be accurately determined by measuring the surface length of RCF cracks.

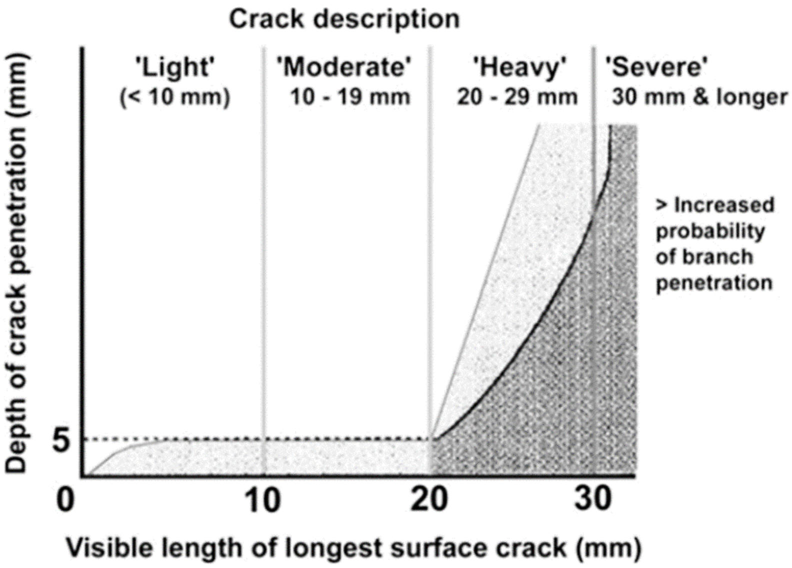

Figure 2.7 The visual length-depth guidance diagram for RCF cracks currently in use by Network Rail, UK [70].

The research [3] reporting on RCF crack shapes and propagation characteristics based on an extensive survey of experimental data in rails removed from service showed that the investigated RCF cracks data all fit in the UK rail system guidance diagram (Figure 2.7). Figure 2.8a shows a series of RCF cracks on a railhead sample taken from service being vertically sectioned to investigate crack profiles and Figure 2.8b shows the reconstruction of these cracks on a transverse plane [3]. It shows that the crack shape can vary for these cracks with the crack subsurface extending beyond the surface-breaking component (crack 6). It should be noted that some heavy and severe cracks (crack 1 and crack 5) propagate beyond the angled straight line turning to a ‘S shape’ or ‘mirror S-shape’ (shown as the surface-breaking component) [3]. In general for light and moderate categorised cracks, it was shown that the crack shape can be represented by a semi-ellipse (elliptical ratio from 1 to 1.75) and this approximation provides a more simple way for modelling studies on RCF cracks [71, 72]. Figure 2.9 shows the reconstructed three dimensional views of a moderate (surface length of 12.92 mm) and a light (surface length of 4.93 mm) RCF crack overlaid with the semi-ellipses used to approximate them. The approximate semi-ellipses are with surface length of 14 (pocket length of 4.2 mm) and 4.9 mm (pocket length of 1.9 mm), respectively [22].

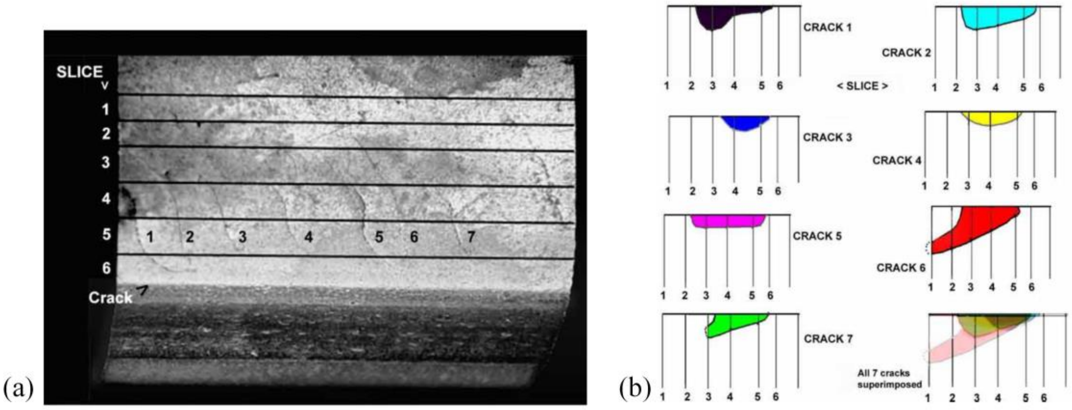

Figure 2.8 (a) Multiple axially aligned, vertical sections (along black lines) through a series of seven RCF cracks on a used rails; (b) the multi-slice axial sectioning and analysis of crack shapes on each slices allowed reconstructions of crack shapes on a transverse plane for the seven cracks and six sections from (a) [3]; probable traffic direction from left to right.

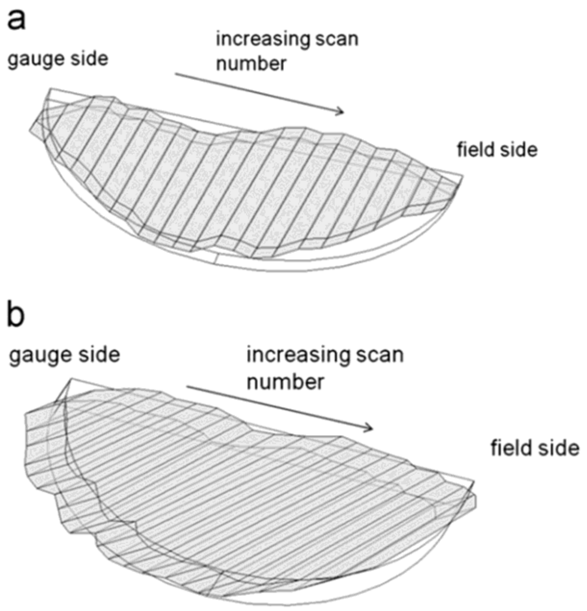

Figure 2.9 Semi-ellipse shapes used to approximate a (a) moderate and (b) a light RCF cracks, where the cracks were observed using X-ray tomography in samples removed from a rail [22].

The Rail Surface Condition Alert (RASCAL) program reported an investigation on RCF crack morphology for standard metallurgy and head hardened rail samples, provided by BNSF and Canadian Pacific Railways [73]. The cross-sectioning work reported that the crack morphology for the standard and head hardened rails to be very different; the standard rails showed the conventional inclined cracks caused by plastic flow and fatigue, but the head-hardened rails were relatively less plastically deformed, with cracks propagating at small horizontal angles to the running direction and being almost vertical into the railhead (< 1 mm in depth) [73]. A study [74] shows the MPI visualizing of the formation of head checks on different rail grade after a total load of 60 MGT; the rail grade (R260) with the lowest hardness has the longest head checks (0.8 mm) and the largest crack spacing (1.0 mm), whereas the hardest rail grade (370LHT) in the test has the shortest in the crack length and the smallest in the crack spacing. Other tests confirm that head checks are finer, shorter and have smaller crack spacing by increasing rail hardness [75]. Therefore, the rail steel grade has an influence on the crack characteristics including the crack size, crack shape and crack spacing.

2.2.2 Shelling (spalling)

Shelling is usually identified as the loss of horizontal large chunks of metal at the rail gauge corner as a result of either subsurface cracks linking up with other cracks such that the metal above is separated from the rail, or gauge corner collapse due to the excessive loading and shear stresses, as shown in Figure 2.10 [1].

The shelling develops because of poorly restrained high rails, well-lubricated rail with a particularly high-stress gauge corner shape and even some rails in a dry environment. Shells from gauge corner collapse usually occur at the high rails on heavy haul railroads. However some tangent rails with local cross level (this is a measurement of the difference in elevation between the top surface of the two rails at any point in the railway track) errors or poor wheel-rail profile matching rails with even light axle loads being reported to show shelling defects [1].

Spalling is a similar defect as shelling that occurs at the gauge side of the rail, leading to material separating from the rail; extended shelling is sometimes misleadingly designated as spalling [37, 63]. Spalling is known as some shallow chip of rail material falling out due to surface initiated crack development and linkage with other similar shallow cracks in the gauge corner area, as shown in Figure 2.4. It is also reported that spalling frequently occurs in cold climates as rail steel stiffness increases (i.e. elastic modulus increases as temperature decreases; elastic modulus is a measure of the stiffness of a solid material, defining the relationship between stress and strain in a material) [63].

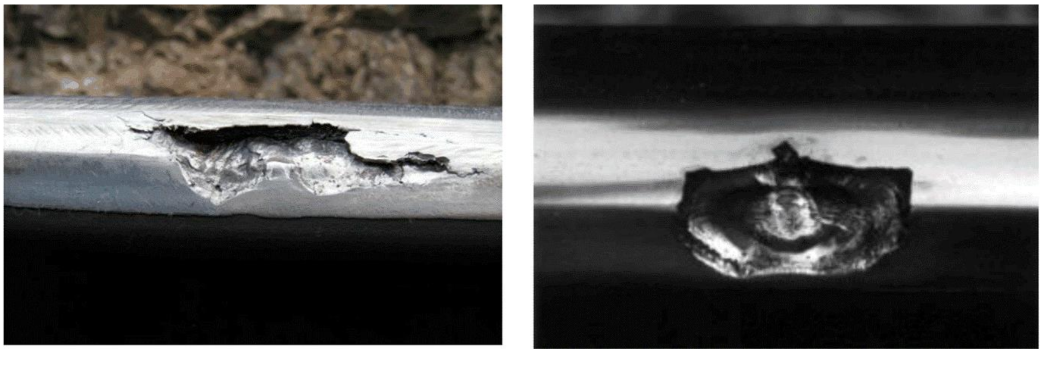

Figure 2.10 Examples of shelling (large chunks of metal falling out) from gauge corner collapse [1].

2.2.3 Squats

Rail squats are surface or sub-surface initiated defects propagating longitudinally and laterally caused by RCF generally arising on the crown, rather than the gauge corner, of the railhead. It is characterised as a shallow depression normally on tangent and gently curved rails, but recent research shows that rail squats can be found in almost every type of rail in either passenger or heavy haul traffic for low, medium and high speed trains all over the world [64]. The depression is caused by sub-surface crack propagation reducing the strength of the material, and the accumulation of dirt and debris in the depression gives the appearance of a dark spot, as shown in Figure 2.11 [1].

It can be observed from the cross section of a squat (shown in Figure 2.11b) that it consists of two major cracks: one short leading crack (in the travel direction) and the other longer trailing crack propagating in the opposite direction. These cracks normally occur at 10-30° to the horizontal and propagate 3-5 mm below the rail surface [1, 65-67]. Small cracks from branching at the end of the trailing crack will prevent an ultrasonic signal from detecting the deepest crack (the shadowing effect, see section 2.3.2); these cracks may turn downwards causing a transverse fracture of the rail.

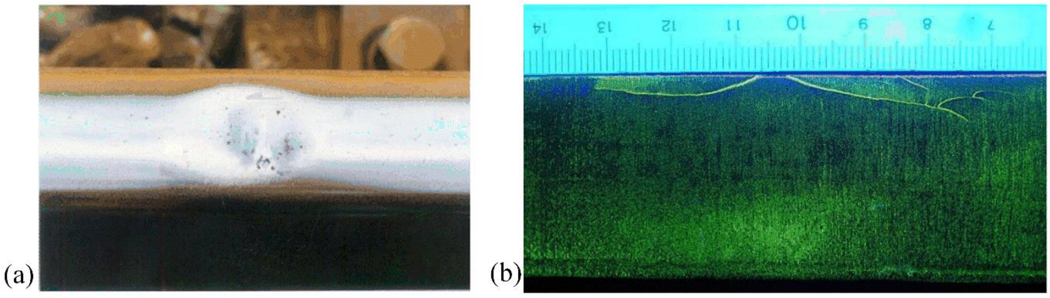

Figure 2.11 (a) A rail squat showing with the dark spot containing dirt and debris; (b) cross section of a rail squat showing a leading crack (left hand side) and trailing crack (right hand side) propagating in an opposite direction with small branching [1].

Two different mechanisms of squat formation have been reported and therefore, two types of squat are considered [66-68]:

1. The classic squat defect is formed because of plastic deformation (ratchetting) of the surface layer from wheel-rail traction (slip). The propagation of the sub-surface cracks is influenced by hydraulic entrapment (water or liquid lubricant) with tensile and shear modes of crack growth.
2. Squat type defects defined as studs, which can develop without any significant plastic deformation of the rail surface. The initiation and propagation of studs are closely associated with the formation of white-etching layer (WEL), due to thermal damage caused by wheel-rail slip. There is no evidence that hydraulic entrapment is required for crack propagation in this case.

Details of differences and similarities between squats and studs can be found in [69], which reviewed historical work on squats and recent findings on studs. This also provided the basis for research [67] on studs with original observations from track and metallurgical examinations of specimens.

2.3 NDT techniques for rail inspection

Non-destructive testing of rails is very important to railway risk management and maintenance planning. Rail defects such as RCF cracks are dangerous, as shown in Figure 2.7, such that if the RCF cracks exceed 20 mm in length and the propagated depth is beyond 5 mm there is a high possibility that the cracks are rapidly increasing in depth and will not be removable by rail maintenance procedures. This will cause serious safety problems, therefore control of RCF cracks requires the identification of cracks in their early stage of propagation, when they are relatively small in size and can easily be removed by rail grinding.

Rail grinding is the effective treatment for rail maintenance to increase rail life by removal of surface damage from the rail [2]. The priority of rail grinding is sometimes driven by the severity of RCF cracks and this information can be acquired by NDT techniques including visual inspection, ultrasonic related inspection and electromagnetic related inspection, etc. The main NDT methods for inspecting rail defects are discussed below:

2.3.1 Visual inspection

Visual inspection (VI) is usually implemented by an experienced worker walking along the rail tracks physically looking for defects. Manual visual inspection for RCF cracks can be improved by using dye penetrate or magnetic particle imaging that enhances the visibility of the fine and closely spaced cracks. VI is also used for rail manufacturing for protrusions, hot marks, seams and scratches, etc [2].

With advancements in photography and computer processing, automated visual systems are being developed by installing high speed cameras onto trains for inspection of rails to meet the demand for high speed and high efficiency inspection. SNCF (National society of French railways) inspects the rail network using a high speed camera (frame rates in excess of 250 frames per second) installed on a train with speed varies from 60 km/h to 320 km/h depending on the type of inspection carried out and the resolution required (high inspecting speed can be achieved by increasing the length of the rail that each image can cover). This inspection is performed at high speed every 15 days for visual surface defects [9]. Figure 2.12 shows the principle of automated visual inspection for rail track [9]. It shows that the high speed inspection system is based on the use of high-speed cameras which can record videos or images of the track when the train moves over it; images are then analysed automatically using algorithms designed for identification of rail components or surface defects [9, 14]. The performance of the system is mainly dependant on the resolution of the image, for example identification of small defects on the railhead is of interest, and the processing algorithm associated with the data storage and the computing time when high speed inspection is required. However, higher resolution of the image means a greater amount of data processing and storage and thus more computational time is needed to complete the analysis. As a results the inspection speed needs to be compromised to keep in pace with data analysis. VI cannot provide any information about the presence of any internal defects; the relationship between crack surface length and crack vertical depth is not guaranteed, therefore the RCF crack depth information from VI is not accurate.

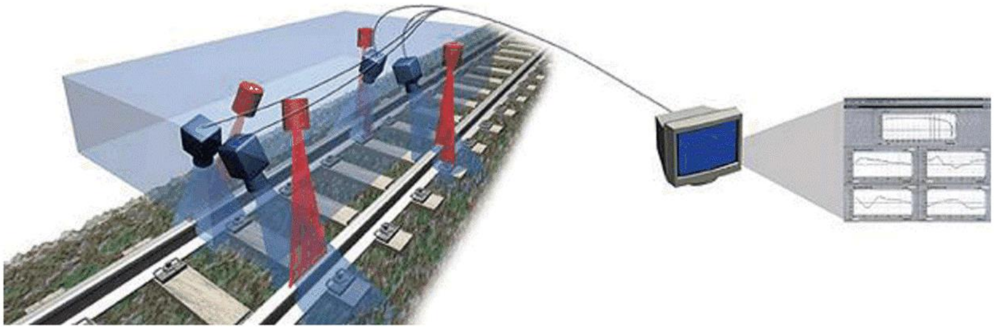

Figure 2.12 Automated visual inspection for rail track using high speed cameras; cameras are set up to different positions and different angles achieving full coverage of rail track components [9].

Automated visual based systems for real-time inspection have been developed to not only detect defects such as cracks, flakes and corrugation on the railhead but also the irregularities relating to the ballast, fasteners, rail anchors and turnout components [76-79]. For example, a real-time visual inspection system (VIS) [7] was developed for discrete surface defects (appear in a random manner without common texture or shape features, unlike RCF cracks that have periodic texture features). The system is made up of a high speed and high resolution camera and four LED lights as the illumination. The inspection procedure including rail image acquisition, rail track extraction, image contrast enhancement and defect localization with an algorithm (longitudinal and transversal position localization, defect recognition). The VIS can detect small discrete defects (with defect area between 80-314 mm^2) with an accuracy of 80.41 % and large discrete defects (with defect area > 314 mm^2) with an accuracy of 93.1 %. The processing time for a single rail image is less than 20 ms allowing the detection speed to be about 216 km/h based on the setup of VIS that can obtain a single image covering 1.2 m of a rail [7]. A visual inspection based on the geometrical defect locating algorithm was also proposed for railhead surface defect, such as RCF defects [80]. The algorithm can locate a series of RCF defects and identify the length and width of the defect area (rectangle). This may represent either multiple light to moderate gauge corner cracks with small inner spacing or large portion of shelling and squat, of which the defective area can be considered approximately as a consecutive region on the rail surface. Discrete individual RCF cracks however cannot be distinguished due to the fine crack width.

The rail track inspection with automated visual system is also used for finding missing clips [81] and measuring the rail gauges [82]. The images algorithms have been optimized [7, 83] to improve the PoD and to reduce the processing time for high speed inspection.

2.3.2 Ultrasonic testing

Ultrasonic testing is the most widely used NDT technique in railway inspection for defect detection. The ultrasonic probes can be either installed on a manual push-trolley or used for high speed inspection by being installed on a train/vehicle running over the rail [8]. For the conventional ultrasonic technique, piezoelectric transducers generate high frequency acoustic waves and transmit them into the sample with the help of couplant (usually water in rail inspection) between the transducers and sample surface. Discontinuities present at the surface or within the tested component reflect or scatter the ultrasonic waves and the transducer receives the “echo”. The result can be obtained by analysing the amplitude of this “echo” corresponding to the crack characteristics and the “echo” travel time which is proportional to the location of the crack [84]. The refracted angles in the transducer are usually 0, 37, 45 and 70° so that the PoD for rail defects is a maximum and array ultrasonic transducers are positioned to cover the whole area of the railhead for longitudinal defects [8, 14].

Ultrasonic transducers have been developed for rail inspection conducted by Sperry trains (UTU1 and UTU2 models) in many countries [9]. The UTU1 model had a problem of too many false readings due to an inappropriate detection threshold and detection criteria, but the UTU2 model has resolved these problems and has a greater probe array that can provide wider ultrasonic coverage. The system can achieve a success defect identification (specific defects or severity of defects have not been reported) rate of 90-95 % and can run at a speed up to 65 km/h. However a review in 2008 [14] reported that the actual inspection speeds can decrease down to 15 km/h due to the detected defect needing to be verified by manual inspection.

The UT technique used in rail inspection still suffers from several drawbacks: UT sensors must be calibrated before any tests, therefore, a calibrated sample with the same properties as the rail is needed; UT signals are sensitive to the rail surface condition and small surface cracks (< 4mm in depth) are not detected because the noise signal from the near surface is large and complex and the systems generally ignore the noise signal to focus on internal inspection [1]; larger surface breaking or internal defects can be masked by small surface cracks and thus give a false signal of the structural integrity of the rail when using high-speed UT systems, known as the shadowing effect shown in Figure 2.13 [85]; different microstructures reflect different signals which decreases the accuracy of ultrasonic testing of rails, for example, the reflection and refraction data of ultrasonic inspection on used rails indicate the material properties are anisotropic and a calibrated system based on isotropic ‘new’ rail may not be effective in finding transverse defects in railheads [86].

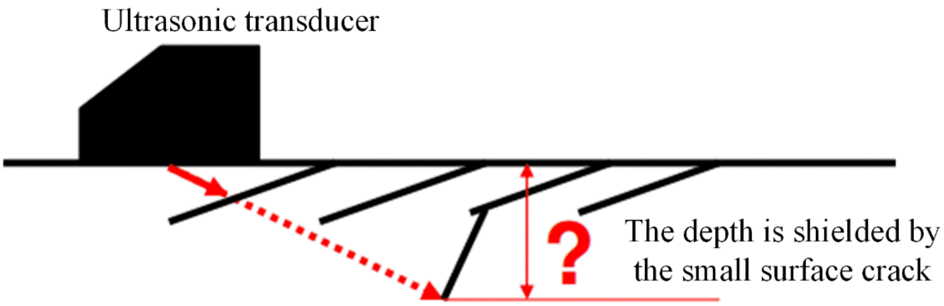

Figure 2.13 Illustration of the shadowing effect [85].

Novel NDT techniques based on ultrasonics are being developed for high speed rail inspection. Ultrasonic phased array (PA), with adjustable refracted beam angle and focus, is sensitive to small cracks particularly for transverse cracks across the railhead [10, 87]. This is particularly beneficial for defects detection in alumina-thermic rail welds, as in this case the ultrasonic beam can be steered to be perpendicular to the defects [14]. However the inspection speed using the PA system reported in [14] is about 5-6 km/h due to the large amount of data generated and data processing. Long-range ultrasonics (guided waves) is used to detect defects and welds that cause cross section change (typically 20 % of the railhead cross section area is required for detection) in long and narrow structures (pipes and rails) by employing surface waves such as Lamb, Plate and Rayleigh [14, 88-90]. A commercial long-range detecting vehicle, known as Prism, has been reported to be capable of detecting large transverse cracks (i.e. equivalent to 20% of the cross section of the railhead) at a maximum speed of 15 km/h [12].

Electromagnetic acoustic transducers (EMATs) have been developed based on the principle that a Lorentz force generated in a magnetic field has the ability to produce ultrasonic waves in materials. It is a non-contact (several millimetres above sample surface), non-couplant UT technique which is suitable for rail defects inspection. It is reported that EMATs can detect gauge corner cracking with 1.5-15 mm depth and could characterize cracks at speeds of up to 100 mph if data acquisition and analysis are improved [91-93]. A commercial hi-rail vehicle inspection system based on EMATs system has been developed in Canada and it can successfully detect different types of defects, including horizontal and vertical head split, bolt hole crack, defective weld and transverse defect (machined slot 12.7×16.1 mm) in a calibration track (150 metre) at speeds between 10-15 km/h [14, 94]. RCF defects such as head check and shelling can be detected by the system however the details of detect/sizing have not been reported. EMATs has been reported to determine the vertical depth for angled surface-breaking cracks by measuring the in-plane and out-of-plane velocity components of the Rayleigh wave in the vicinity of cracks [95]. In the procedure for charactering cracks, image analysis carried out first to determine whether the vertical angle is in the near-90° range or inclined to the surface; the vertical depth can be determined if the crack is near the 90° range by using the 90° depth calibration curve; F_{ER} (the ratio of the in-plane to the out-of-plane enhancements of the Rayleigh wave measured by the EMATs) then should be calculated for inclined cracks; The F_{ER} then can be used to estimate the vertical angle and a correct depth calibration curve can be selected to determine the depth [95]. In this research, however only two depth calibration curves (for 90° and 45°) have been studied and tests on natural inclined cracks have not been shown; the relationship between F_{ER} and vertical angle is non-monotonic (i.e. one value of F_{ER} may correspond to two vertical angles) for vertical angle less than 40°. This may cause misestimate of the dimension RCF cracks, which vertical angle usually less than 30°.

Laser ultrasonics is also a non-contact technique by generating ultrasound using a pulsed laser. Laser ultrasonics combined with the air-coupled acoustic transducers (LAHUT) was developed for detecting surface-breaking and internal cracks located in the railhead, web and foot. It is reported that the system was installed on a hi-rail vehicle designed for running over the rail at speeds between 8-15 km/h [11, 14, 96].

In a test using the LAHUT for the inspection of vertical split head and rail foot cracks, the success rate is 100 % and 90 % for the vertical head split defects and rail base cracks, respectively at walking speed [97].

2.3.3 Acoustic emission

Deformation or cracking events, such as plastic deformation, crack initiation and propagation, etc. occurring from a materials surface or interior are usually accompanied by a sudden elastic strain release. Acoustic emission (AE) relates to the ultrasonic waves generated in this process. AE monitoring is employed to detect a broad frequency range of such ultrasonic waves between 20 kHz and 1 MHz and can be easily differentiated from conventional vibration (lower frequency up to kHz range) and from electrical noise (above 2MHz) [14, 98]. Therefore, AE techniques have been used to evaluate the structural integrity of large industrial structures such as bridges, oil tanks and the detection of gas and liquid leaking [14, 99].

Although AE is not a new technique, AE applied to real-time monitoring for crack propagation (crack growth) in rails is a relatively novel method. Kostryzhev et al. [100] experimentally verified that the AE signal shows a good response to crack growth in rail steels and the pattern of signal changes correspond to fracture mode. Ductile fracture gives a high duration, low frequency signal and low duration, high frequency signal corresponds to brittle fracture. Yilmazer et al. [101] pointed out that by developing more suitable filtering techniques for signal processing of acquired AE waveforms, rolling noise associated with the wheel may not be a barrier for crack growth detection in the field. Research [98, 102] using AE to measure the rail-wheel interaction (influence by axle loads, wheel roundness, speed and tractions) for cumulative damage by wear and contact fatigue have also been reported. However, most of this research has been carried out in lab experiments, as AE signals are usually affected by environmental noise, mechanical noise and electric noise, etc. The most important research field therefore will be AE signal processing, i.e. how to filter the AE signal from noise signals by using optimised algorithm and advanced software [14].

A review on NDT in rail in 2008 [14] reported that NoiseMon, based on an AE system developed for detection and evaluation of the noise between wheel-rail interfaces when the train moves along the rail, is promising for detection of rail breaks, squats, wheel burns, track alignment, gauging problems. The sensor is protected by foam windshields and placed in the aerodynamically dead area to reduce the influence of airflow on the received signals, therefore the inspection speed can be increased up to 160 km/h for certain defects. A research [103] in 2013 reported that NoiseMon system has been employed to evaluate the acoustic track quality (ATQ), a measure of the surface roughness of the running rails, across over the Great Britain's railway network; based on the analysis of MoiseMon data, the average ATQ value decreases 8 dB relative to 2004 because of a new preventative maintenance rail grinding strategy to address RCF; The result indicated that the majority of GB's East and West Coast mainlines (ECML & WCML) have rails with roughness levels below the TSI roughness limit. However no research has been reported using the NoiseMon system for RCF cracks detection. More recent work [104, 105] using acoustic emission have been focused on online monitoring of railway axle bearing defects and wheelset defects; laboratory and field tests showed that the AE can effectively distinguish faulty axle bearings from defect-free bearings by using appropriate frequencies and signal processing methodologies, but for lightly to mildly damaged bearings (specific dimensions not provided), due to the low signal to noise ratio, AE is unable to detect the types of cracks present (wheel flat, lubricant contamination, outer race and inner race defects) [105].

2.3.4 Magnetic flux leakage

MFL technique is used in the rail industry for detection of surface or near surface cracks especially for transverse cracks. MFL sensors can operate with permanent magnets or DC electromagnets that generate magnetic flux that can be coupled into the rail surface. It has similar principles with magnetic particle inspection (MPI) depend on detecting the magnetic flux change caused by surface or subsurface defects as the magnetic flux will leak from the surface breaking component of the defects. Instead of using magnetic powder to indicate the presence of defects (MPI), MFL employed a magnetometer to conduct quantitative measurement of the leakage field near a defect [106].

MFL systems can be classified into two group, according to the magnetic flux distribution in relation to the positon of the defects: circumferential MFL used for detecting and sizing longitudinal defects; and axial MFL used for volumetric or metal-loss type defects, particular for defects with a circumferential extension [107]. In rail inspection, MFL sensors can detect transverse cracks such as RCF cracks but defects with an orientation parallel to the magnetic flux lines are not detectable as well as some internal cracks being far away from the sensor. It is also adversely affected by increasing inspection speed as the magnetic flux density decreases as the speed increases, consequently the signal is too weak to detect for small cracks; in addition, the magnetic field is also influenced by the generated eddy currents due to the relative movement of the probe and specimen, which induces variation in the MFL signals. A hybrid inspection system combining ultrasonic probes and MFL sensors has reported [8] and the inspection speed is normally at 32 km/h. The system was used to inspect the "coal territory" of North America-mountains, curves, severely worn rail and variable weather conditions; the system helps to find more defects at an earlier point in the defect's growth cycle, results in over 50 % reduction of railhead defects; an analysis of defects detected by the system on one freight railroad showed that 20 % of the defects can only indicated by the use with induction [8].

Research [107] based on a 2D FEM model was carried out to investigate the responses of MFL signals to probe velocity (0-30 m/s) and the relationships between the x-component of the MFL signals and the defect depths (4-8 mm; vertical slot into a conductive specimen). Figure 2.14 shows the results where MFL signals decrease as the probe speed increases whilst they increase as the crack depth increases. The asymmetrical signals caused by the probe speed (signal is symmetrical when the probe is static) can be used to indicate the probe movement direction.

Further research [108] using 3D magnetic field sensing (i.e. by employing a three-axis magnetic field sensor to include the y-axis, orthogonal to the testing surface and the applied field) for MFL signals was carried out to characterise a machined slot and a naturally occurring surface breaking crack ("L shaped" crack consisted of a horizontal, diagonal and a perpendicular sections) close to the gauge side of the railhead. The x-component (parallel to the rail surface and the applied field) and the z-component (perpendicular to the rail surface) of the MFL signal give a good indication of the position of the perpendicular section of the crack and the ends of the crack, respectively. The y-component (parallel to the rail surface but orthogonal to the applied field) is useful in detecting the diagonally orientated section of the cracks. The sensor currently only tested with the sample in laboratory and it suggested that 3D magnetic field sensing can be used to improve the defect characterisation using the MFL signals, especially for defects with irregular surface-breaking components. However the study focused on the locating of the crack and the information about the crack sizing was not provided.

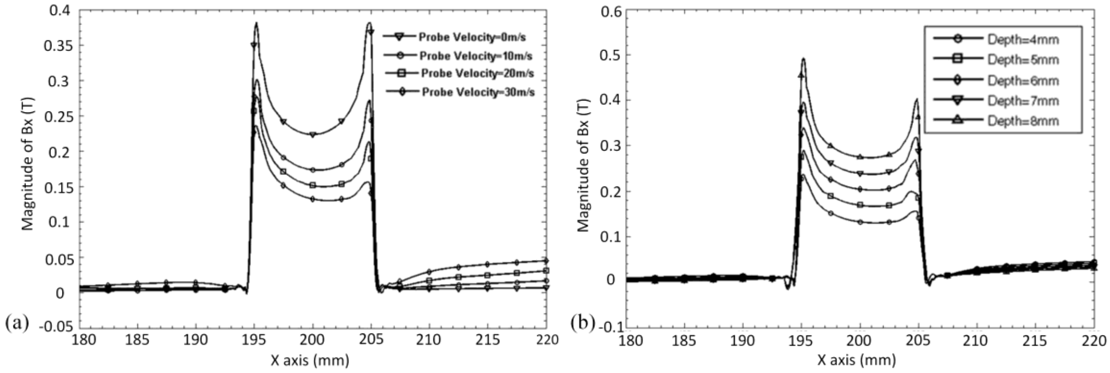

Figure 2.14 X-component of the MFL signals against (a) probe velocity; (b) crack depth for probe velocity at 30 m/s [107].

2.3.5 Eddy currents

The technique of eddy currents is based on the principle of electromagnetism that an exciting coil with an alternating current can generate a magnetic field around the rail surface when placed perpendicular to the rail component; then the eddy currents are induced within the skin depth of the rail surface layer and the eddy currents also generate a secondary magnetic field opposite to the first magnetic field, as shown in Figure 2.15a [109]. The sensing coil can measure the impedance change of the system and any defects present at the surface or sub-surface of the rail can lead to a disturbance in the secondary magnetic field, causing the impedance deviate from Z_1 to Z_2, as shown in Figure 2.15b [18].

As the eddy current technique, based on the skin effect, is sensitive to any changes at the surface or near-surface of the rail, it has been used in rail inspection system, as a supplementary technique to the conventional ultrasonic transducer for surface crack detection and sizing. The technique has better ability, compared with ultrasonics, of detecting defects such as RCF cracking, squats, shelling and surface corrugation [13, 18, 110, 111]. A summary of the ability of eddy currents in detecting various surface defects of rails is shown in Table 2.1 but the details of accuracy were not given in [13] .

A hybrid inspection system has been developed and used by Deutsche Bahn DB (German Rail) AG that combines ultrasonic techniques with eddy current sensors for surface and sub-surface defects inspection [13, 18, 112]. The system consists of 10 ultrasonic probes at angles from -70° to 70° and 4 eddy current sensors located at the gauge side 25 mm of the railhead where RCF cracks usually occur (as shown in Figure 2.16 [13]). The inspection speeds can be up to 100 km/h with the eddy current signal remaining unaffected by speed [14]. The eddy current sensors have also been implemented on a grinding train focusing on the detection of head checking and providing position and depth information to on-line control of the rail grinding machine [113].

In order to give accurate depth of the damage in rails, the inspection system was calibrated by grinding a rail with gauge corner defects at a relative low material removal rate; eddy current measurements and cross-sectional measurements were performed to determine the signal and associated amount of material removed. As a result a calibration curve was established which allows the crack depth determined on the basis of the detected eddy current signal [114]. The system was not able to identify cracks with crack spacing smaller than 2 mm as the calibration curve was based on single cracks. A statistical method of practical field measurements was used to compensate the signal allowing the assessment of multiple cracks. However, the research [115] mentioned that the crack propagating angle (vertical angle) is necessary for determination of the crack depth but the details of how vertical angle can be measured was not given, or whether an assumed value was used. The system, known as HC Grinding Scanner, has been continually developed under Speno International SA.

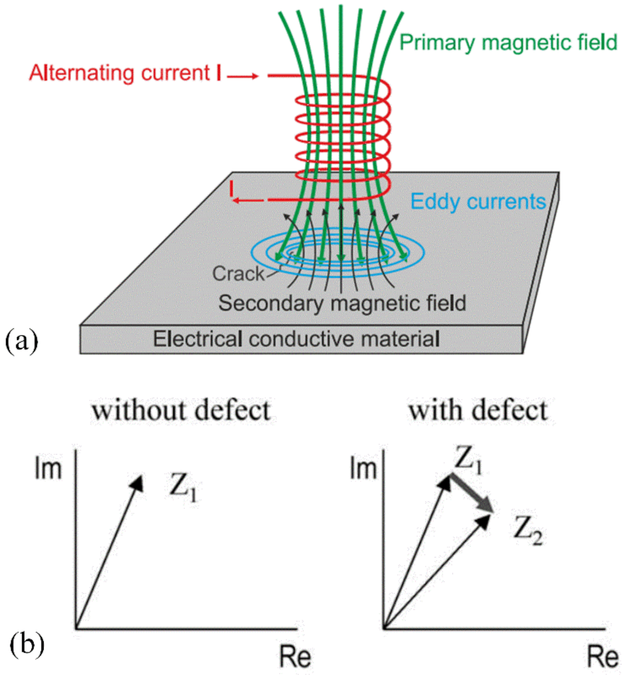

Figure 2.15 (a) Illustration of eddy current generation [109]; (b) variation of the sensing coil's impedance due to the presence of a crack (vertical and horizontal axis represent the imaginary and real part of the impedance, respectively) [18].

Table 2.1 Sensitivity of eddy current sensors to defects summarised by German Rail (details of accuracy was not provided; belgrospi's refers to indentations and cracks on crests of short wave corrugation) [13].

Category	detectability	Statement
Head checking	Very good	Quantity, location, depth
Wheel-burns	Very good	Location, extent
Grinding marks	Very good	Quantity, location, period
Rail joints	Very good	Location, kind
Indentures	Very good	Quantity, location, period
Squats	Good	Quantity, location
Short/long pitch corrugation	Good	Location, period
Welds	Good	Location, kind, lack of fusion
Belgrospi's	Good	Quantity, location

Unlike conventional ultrasonic techniques, EC does not require any contact with the rail surface, which makes it suitable for high-speed inspection. However, as the exciting coil is normally perpendicular to the inspected surface, the magnetic flux that can penetrate into the surface decreases rapidly as the senor lift off increases. The eddy current signal subsequently diminishes with sensor lift-off; lift-off of eddy current sensors is typically no more than 2 mm for rail defect inspection [14]. It is a drawback for analysing EC signals that calibration blocks are needed to estimate the detected crack characteristics.

Instead of the empirical methods being used at present, the mathematical models for eddy current systems have allowed accurate predictions of the sensor responses to crack characterisation. Burke [116] reviewed the crack sizing modelling method (the swept-frequency method), which uses the absolute values of the change in the coil impedance due to the crack as a function of the coil position and frequency; the method measures over a range of frequency and uses an approximate solution to Maxwell's equations for the determination of the crack depth. The method was tested for a range of single rectangular and semi-elliptical EDM slots (vertical angle of 90°) in Al alloy plates and results showed that the depth was determined within about 15 %; it was also tested for a range of fatigue cracks in compact tension specimens but the depth of smaller cracks was underestimated due to the crack-face contact effects (i.e. two crack surfaces connected and eddy currents flow through the connection rather than the crack tip, resulting in underestimate of the crack depth); no results about any crack vertical angle measurement or the performance predicting angled cracks were reported. Bentoumi, et al. [111] compared three signal processing algorithms for on-line evaluation of minor rail defects (shellings and welded joints) with a design of a double-coils and double-frequencies sensor in a subway train that give 8 complementary eddy current signals; the wavelet approach showed best results but wrongly classified a shelling defect as a welded joint.

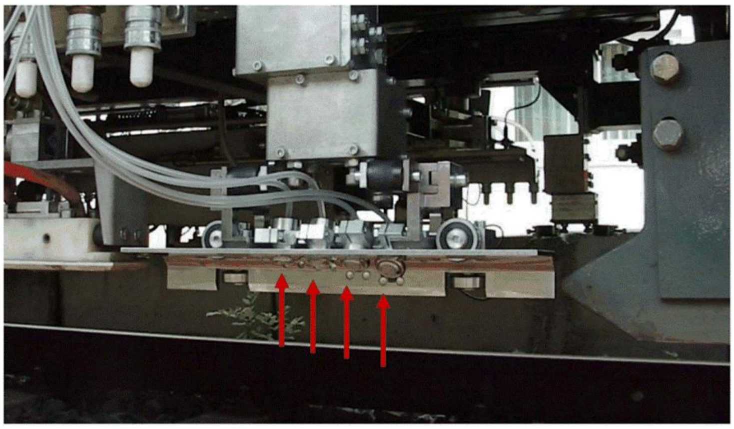

Figure 2.16 A set of 4 eddy current sensors (arrowed) installed on the inspection train combined with the ultrasonic technique as the high speed inspection system used in German Rail [13].

2.3.6 Alternating current field measurement

Alternating current field measurement (ACFM) is a novel electromagnetic technique based on the principle of skin effect that the alternating current flow concentrates in a thin layer at the surface of a conductive material and will be disturbed by the presence of cracks [117]. ACFM technique shares a similar principle with the eddy current technique that both are detecting the field change because of the induced current being disturbed by the presence of cracks, but instead of detecting the electrical impedance the sensing coil of ACFM directly detects the variations in the magnetic field. In addition, ACFM sensors are designed to generate a uniform current flow around the defect with the exciting coil being parallel with the inspected surface, while for conventional EC techniques a swirled current is usually generated around the defect due to the exciting coil being vertical to the inspected surface. This character of ACFM gives the signal a good tolerance to sensor lift-off as the current induced by the magnetic flux of a horizontal coil decreases slower when the sensor is lifted than that of the magnetic flux of a vertical coil, which is the case of the eddy current approach. It is reported that the signal strength of ACFM diminishes with the square of lift-off rather than its cube (the eddy current) and a maximum operating lift-off of 5 mm is allowed without significant signal loss when using ACFM sensors [15]. The ACFM technique is therefore a topic of interest for research and is an alternative to eddy currents for rail inspection.

The ACFM sensor is not only capable of detecting cracks, but can also provide accurate size information (experimental and modelling results for crack pocket length have been reported to be within 2.5 % difference for the single moderate crack and 2.0 % for the single light RCF crack, respectively [22]) for surface-breaking crack if the sensor is placed parallel with the crack orientation (more results and discussions is given in chapters 4-7). Figure 2.17 shows the principle of ACFM operation and the signals used for crack dimension estimation [118]. As the ACFM sensor is positioned above the inspected surface, the horizontal coil with alternating current in the exciting sensor works as a solenoid and, therefore can induce a uniform current in the surface layer of the conductive material with no crack present. Any existence of a defect will disturb the current and force it to flow around the ends and down the faces of the crack; this causes the magnetic field generated by the induction current above the surface to become non-uniform and the ACFM sensor measures these variations in the field.

The current flows clockwise and anti-clockwise when it passes the ends of the crack generating the peak and trough in the Bz signal, which can be used to give an estimation of crack surface length. The current that flows down the crack surface generates the trough in the Bx signal which can be used to estimate of the crack pocket length.

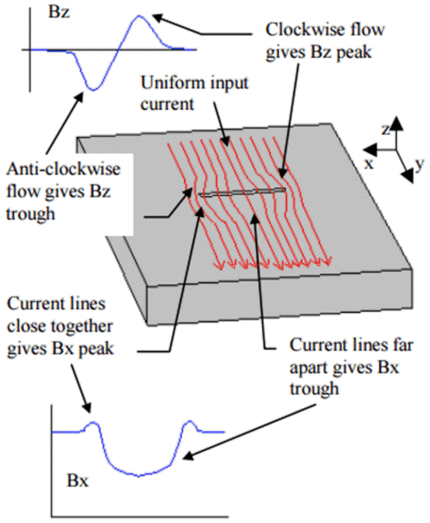

Figure 2.17 Illustration of the ACFM principle where the uniform current is disturbed by the presence of the crack giving the Bx and the Bz signals which can be used for the crack pocket length and the crack surface length estimation [118].

The theory of ACFM was developed by researchers at University College London (UCL) in the mid 1980’s, as driven by the need of oil companies to find a substitute for the A.C. potential drop (ACPD) method for estimating the depth of fatigue cracks during underwater weld inspection. Instead of maintaining very good electrical contact between the surface and the probe used in ACPD, ACFM can induce rather than inject uniform currents into the inspected surface. Based on the existing theoretical model of the uniform current flow distribution around semi-elliptical surface-breaking defects [117], researchers at UCL extended the analysis to calculate the associated magnetic fields above the surface. The length and depth of the crack can be determined by comparing the results of ACFM measurements with theoretical predictions. The ACFM technique is relatively insensitive to lift-off and material property (permeability) changes, and, as it does not rely on contact, it has been widely used in underwater, oil drilling, pipeline and rail industries, especially for inspecting through paint and other coatings or in welded structures without surface preparations.

2.3.7 Summary

Despite the fact that conventional NDT techniques used for rail inspection have been greatly improved and novel techniques have continued to emerge and be incorporated into the railway inspection system, there is no single NDT method that can meet the requirement of high-speed inspection without a compromise in reliability and efficiency. Ultrasonic techniques are still the main inspection method all over the world but hybrid inspection systems that combined ultrasonic techniques with induction methods can inspect rail internal defects at a high speed while effectively increasing the PoD of surface and sub-surface cracks. ACFM is one of the induction techniques being developed in the UK and numerous research programmes have shown the promise of utilization of ACFM in the rail industry. Table 2.2 briefly summarises the NDT techniques that are currently used in railway inspection [9, 14, 85].

Table 2.2 Comparison of some NDT techniques used in the railway system [9, 14, 85].

Method	Defect detected	Advantages	limitations
Visual inspection	Surface defects, railhead profile, missing parts	Convenient and can be automated with high speed (up to 320 km/h); reliable in detecting big defects and missing parts	Can only be applied to surface; cannot reliably detect small defects at high-speed
Acoustic emission	Rail breaks, wheel burns, squats, worn rail profile	Experimental manual and high-speed systems	Limited development; miss internal defects
Ultrasonics	Surface defects and internal defects in railhead, web and foot	Can be automated (up to 70 km/h); can penetrate thick materials	Misses surface cracks (<4 mm) and internal defects at high speed
Electromagnetic acoustic transducers	Surface defects and internal defects in railhead, web and foot	Reliable for surface and internal cracks	Low speed inspection (< 10 km/h); sensitive to lift-off
Laser ultrasonics	Railhead, web and foot defects	Reliable for internal defects	Low speed inspection (< 10 km/h); adversely affected by lift-off; difficult to deploy at high speeds
Long range ultrasonics	Surface defects, railhead internal defects, rail web and foot defects	Reliable for large transverse defects	Low speed inspection (< 10 km/h)
Magnetic flux leakage	Surface defects and sub-surface crack in railhead	Reliable in detecting surface defects; high-speed inspection (up to 32 km/h)	Misses small cracks due to the high-speed

Eddy current	Surface and sub-surface crack	Can be automated and used for high-speed inspection (up to 70 km/h); reliable in detecting surface defects	Sensitive to lift-off variations and cannot detect sub-surface defect
ACFM	Surface breaking defect	Reliable in detecting and sizing surface breaking cracks; high-speed inspection under development; less sensitive to lift-off than EC	Cannot detect sub-surface defect

2.4 ACFM for crack detections

Standard ACFM probes usually consist of a horizontal solenoid or yoke above the sample surface, with two orthogonal magnetic coils underneath but close to the surface allowing the measurement of the two components of the magnetic field. During operation the probe is moved over the inspected component, parallel to the expected orientation of defects to collect the data required for dimension estimation. Figure 2.18 shows a typical response from the ACFM pencil probe to a crack [119]. The trough in Bx gives an indication of pocket length and the positive and negative peaks in Bz indicate the crack surface length. The Bx signal is plotted against the Bz signal to give a distinctive butterfly pattern (shown in Figure 2.18) to indicate the presence of a crack as well as to eliminate the dependence on probe moving speed.

The ACFM technique is available in the form of either a single pencil probe or multiple-element array probes. The pencil probe can detect the presence of surface-breaking cracks at any orientation, however the probe should be moved in a direction within 0-30° to the crack surface-breaking component in order to accurately size the crack [120]. ACFM array probes can overcome this drawback by deploying various field inducers to cover other orientations at the surface. This is particular useful for situations when the presence and orientation of the crack is unknown [120]. ACFM array probes can also be customised to conform with the inspected component geometry so that the inspection time can be greatly reduced whilst increasing the PoD of defects.

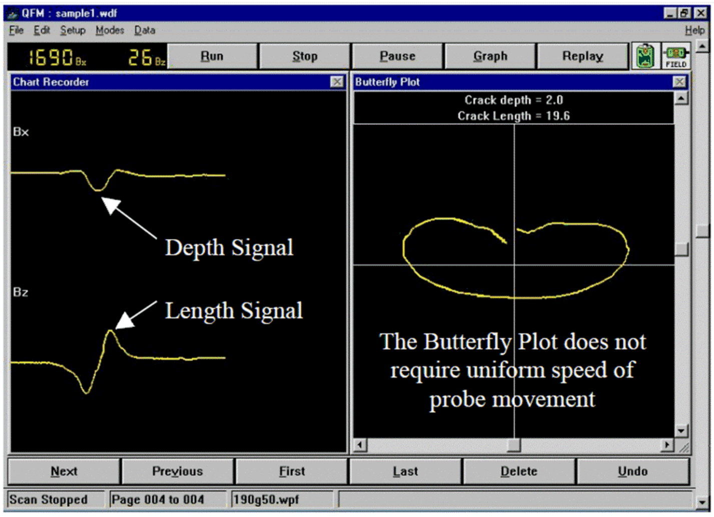

Crack depth = 2.0
Crack Length = 19.6

The Butterfly Plot does not require uniform speed of probe movement

Scan Stopped | Page 004 to 004 | 190g50.wpf

Figure 2.18 A screen shot from the commercial ACFM software showing ACFM signal response to a defect [119].

2.4.1 Underwater inspection

The first ACFM application was originally developed as a substitution of ACPD for sizing depth of cracks discovered by MPI for subsea welds on offshore installations [121]. In 1991, the first ACFM subsea instrument (the U11) was built after experimental demonstrations that ACFM was at least as good as MPI in detecting cracks whilst also providing crack depth information with an accuracy of ±15 % [121]. The ACFM technique was also shown to give a more accurate prediction on the depths of short (in length) and deep (in depth) surface cracks than ACPD in welded components [122]. The fact that ACFM does not require good visibility and can work through paint and rust means it was soon adopted by the offshore industry for not only ferritic steels but also duplex stainless steel and titanium [123].

The U11 was then upgraded to model U21 with developments in electronics, which greatly reduced the size and weight of the subsea unit. It was also improved with multiple sensors, motors and encoders included [121]. In 2002 the U31 system was created with much lower current consumption and again, a further reduction in the size and weight of both the subsea and topside units, which allowed much easier transportation of the ACFM equipment and deployment by smaller remotely operated underwater vehicles [121].

The development and application of the ACFM technique for subsea and topside weld inspection either manually or deployed by an underwater roving vehicle have been reported [124, 125]. An integrated system combining ACFM and electrochemical machining (ECM) was developed to inspect the welded component and then carry out removal of any defective zone; the system sampling/removal operation can be implemented at speeds up to 3 mm/min [126]. In order to interpret the results measured by ACFM probes, a software package, FACTS, which has all the analytical tools and databases of experimental results, was developed to calculate the fatigue crack growth behaviour using fracture mechanics while provide a user-friendly interface for fatigue crack analysis [127]. The underwater inspection of ACFM was modelled using FEM and the results, verified by experimental measurements under seawater environment, show a detection accuracy higher than 85 % with the maximum relative error for crack depth prediction less than 12 % [128]. For these applications the fatigue cracks usually have a large surface length to depth and grow perpendicular to the surface, making them very different from the RCF cracks seen in rails.

2.4.2 Petroleum industry

ACFM applications in the petroleum industry are mainly focused on inspecting for drill string thread and stress corrosion cracking (SCC) on pipeline string. Following the successful application of underwater ACFM, oil companies began to look for other areas where the technique would be beneficial. The inspection of the thread connection of the drill string, for example is one such area once inspected by MPI. However MPI is difficult to deploy in the complex geometry of the thread connection especially for the female box threads. ACFM inspection can be carried out using replaceable shoes to fit different thread geometries and the relative uniform geometry within the thread gives a relative uniform background signal allowing the software to detect and size automatically [121]. The array probe can also be used in such application in order to greatly decrease the inspection time with a single 360° scan [121].

A software package, FADS, was developed to conduct precise calculation and prediction of performance by using the detected data from the ACFM sensor in terms of fatigue and fracture mechanics analysis of the thread connection in the drill string [127]. It was reported, in 1996, that an ACFM system called ATI was developed to inspect pin and box threads of drill string components with sizing of defects greater than 8 mm in length and 0.75 mm in depth [121, 129]. An experimental study was carried out to investigate the influence of residual stress on ACFM crack measurements and the suggestion was given that the ACFM performance was compromised when the defects presented in, or near, large residual stress fields, for example the cold rolling area of the thread root, because the magnetic properties are changed or the crack surfaces contact before the actual crack tip giving a false reading [130].

The ACFM technique also plays an important role in detecting defects in pipeline string and oil tanks. The advantage of ACFM probes being used to inspect material at high temperature, up to 1000 ºC, helps the fabrication of thick wall stainless steel pipeline; each weld run can be inspected using ACFM soon after completion rather than waiting for the weld component to cool down (to allow inspection with MPI or dye penetration); by using the ACFM inspection the weld time can be reduced from 12 hours per weld to 2 hours per weld [123].

SCC is the major threat to the integrity to oil and gas pipelines that can extend by connecting with neighbouring cracks to give a critical size causing product leakage or rupture. ACFM has been successfully applied to SCC inspection in pipelines as ACFM can detect through the coating without surface preparation and provide high inspection speed compared to MPI [118, 131]. Modelling work was carried out to study the performance of a feed-through ACFM probe (cylindrical in shape to encircle the pipe) for detecting axial cracks in the surface of pipe string; the array sensor (consisting of a coaxial excitation coil and a sensing array covered the whole circumference) produced a uniform induced current over the full circumference of the pipe string and simultaneously scanned the full circumference with 18 probes equally spaced at 20° [132]. ACFM array sensors have also been installed on swimming and wall-climbing robots to inspect weld defects and floor corrosion of oil storage tanks while the tank is in-service full of oil [133].

2.4.3 Rail industry

Following the successful application use in underwater inspection and oil industry applications, the ACFM technique was introduced to the railway system to inspect surface-breaking cracks that occur in rail axles, bogies and railheads with cooperation between Bombardier Transportation (vehicle operators) and TSC Inspection Systems (ACFM sensor manufacturers). The first application of ACFM in the rail industry was for rail axle inspection, following a fatal accident involving a failure of an axle [119]. The ACFM system can inspect painted axles without the need to strip and re-paint, which can greatly decrease the time and costs of inspection while helping to keep the integrity of the part by not removing the original coating. ACFM was shown to be a successful substitution of MPI in a series of blind trials, in which several NDT techniques used in the rail industry were used, where the results showed that the ACFM technique outperformed the conventional MPI and the advanced eddy current methods [119]. Normally axles can be inspected either on or off the vehicle by using an ACFM single probe and array probe, respectively. In one development a custom ACFM array probe was designed and deployed to inspect an in-service axle under the Earth Return Brush (ERB), a device to transfer the return current away from rotating components (roller bearings) and lead it directly to the axle, where it is difficult to inspect with conventional techniques [119].

Railway bogies are regularly inspected using a combination of VI, MPI and UT. In the case of MPI or even VI, it requires the bogies to be stripped of all paint and to be cleaned at the inspection areas. It is not possible to gain access to some areas of an in-service bogie, but ACFM can still inspect many areas that are not accessible for MPI and ACFM can also assess the defect depth quantitatively [119]. TSC developed ACFM equipment for use on bogies inspection both at overhaul and in-service. Automated crack detection and sizing using the custom software was used in the experiment to inspect a crack of 5 mm length and 0.5 mm depth. ACFM gave 84 % PoD, 40 % greater than using MPI in which case the depth has to be subsequently determined by using eddy current inspection [15].

The ACFM technique has been used for inspecting RCF cracks on railheads and has been intensively investigated to not only detect but with a particular emphasis on sizing cracks. Conventional MPI inspection is unable to provide crack depth information and conventional ultrasonics is not sensitive to small surface cracks and the subsurface part of a deep crack may be shadowed by shallow cracks. The ACFM technique can estimate the pocket length of small surface-breaking cracks, corresponding to the early stage of the RCF crack development, without any influence of the shadow effect, as current usually flow along the crack surface within the skin depth. The vertical depth prediction from ACFM relies on the assumption that the vertical angle is known or calibration to reference samples. However, RCF cracks on rails are often closely spaced and they normally extend at angles to the running direction as well as the rail surface. The subsurface portion of the cracks may extend to a greater width than the surface-breaking component and sometimes can be deeper than the surface length (elliptical ratio less than 1). The morphology of RCF cracks is complex (see the introduction in section 2.2.1 and more discussion about ACFM responses to RCF crack shapes will be shown in section 5.3) and there is poor correlation between the surface length and the depth, particularly as the cracks get larger. Therefore the morphology of RCF cracks is different to that of the fatigue cracks in subsea and pipe line applications ACFM was initially developed for, which tend to be have a high surface length to depth ratio. Therefore, the algorithm used for ACFM sizing, established for planer defects with semi-elliptical shapes and large aspect ratios, does not work for the case of RCF cracks.

To overcome the problem in sizing RCF cracks, empirical corrections were added to the existing theoretical model for the consideration of different types and sizes of cracks [119]. This required a large amount of data in terms of crack information, therefore extensive calibration experiments with destructive methods were carried out to investigate the dimensions of real RCF cracks and to calibrate (then validate) the results of ACFM inspection. The algorithm with empirical corrections was used to determine the crack size in a number of rails and the accuracy has been significantly improved in comparison to using the old model, as shown in Figure 2.19 [119]. This improved algorithm was integrated to the software which can automatically detect and report the deepest crack in the process of inspection using an ACFM array probe installed on a walking stick. It should be noted that if the rail steel grade or possible axle loading are changed then a different set of corrections might be needed as crack characteristics including crack shapes and crack spacings (for multiple cracks) are influenced by the rail steel grade (see discussion in section 2.2.1). A suggestion is that the FEM model may be used to provide a solution: the model is calibrated using one steel grade, then it can predict the ACFM signal responses to other steel grades effectively (by changing the steel magnetic properties) concerning different crack characteristics.

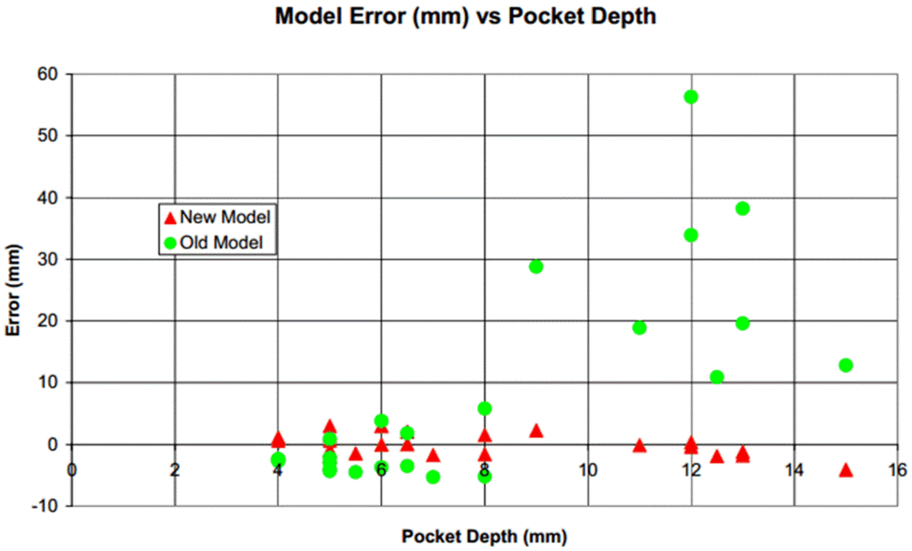

Figure 2.19 Comparison of the size errors for RCF cracks estimated using a model with empirical corrections and the old model developed for planar semi elliptical fatigue cracks [119].

2.5 ACFM for RCF cracks detection and sizing

In the Railway Research Centre at the University of Birmingham, experimental work has been conducted to investigate the ACFM capability for crack detection and sizing during high-speed inspection [17, 134-136]. The work showed that the ACFM sensor can accurately detect artificially induced surface-breaking defects without being affected by increasing speed when the ACFM sensor was installed above a rotary test piece at speeds up to 121.5 km/s. A 3.6 m-diameter spinning rig, constructed of curved rail segments, with rotating speeds up to 80 km/h was also used to simulate the ACFM performance in a condition close to reality. Eight 1.41 m long rails containing various shapes and sizes of artificial cracks, including vertical slots, clusters of angled slots and pocket defects, were installed on the rig and ACFM inspection was carried out. The recorded signals remain unaffected by increases in speed at a constant lift-off (< 5 mm). The ACFM responses to clustered cracks however were found to be influenced by the spacing and the order of cracks (for irregular shaped cracks) within the cluster; in addition, no sizing algorithm was available for crack cluster prediction making the ranking of severity difficult and complicated. An issue identified in the spinning rail rig experiments was that the variations of sensor lift-off became significant (> 7 mm) as the speed increased and the signal could not be compensated due to the limitations in the design of the trolley (used to hold the sensor); at speeds up to 48 km/h, the ACFM sensor could successfully detect some of the cracks (> 2 mm in depth with lift-off varying 1-7 mm) but ranking of the crack severity was not possible. It was also suggested that errors may have arisen for the multiple angled cracks because the machined slot surface opening (> 0.7 mm) is relatively large compared to actual RCF cracks [134].

A robotic inspection system was developed at the University of Birmingham to detect and characterise RCF cracks in rails [137-139]. The system consisted of an automatic trolley, a robot arm and commercial ACFM equipment, as shown in Figure 2.20 [140]. The inspection system can scan the rail with speeds up to 20 km/h and can automatically return to the location of an identified crack to perform a slower (up to 20 mm/s) but more detailed re-scan to provide data for crack depth prediction. A laser sensor is used prior to the ACFM scan to measure the rail profile so that the robotic arm with the ACFM sensor moves at a consistent speed and allows the ACFM sensor to conform to the railhead at a constant lift-off, thereby minimising any errors in measurement. A combined threshold and signature match (CTSM) method was incorporated to optimise the data processing to improve the PoD at high speed with the presence of noise and several lift-off changes during the field test. The advantage of using robotic control is that the sensor orientation can be adjusted through calculating the crack horizontal angle to the rail running direction based on the minimum and maximum positions of the Bz contour map, in which case the Bx perturbation of the ACFM signal is the maximum and therefore can be used for crack pocket length estimation. Static measurements (where the crack locations are known) and dynamic measurements (the system approaching a given crack location) showed the system has high reliability with PoD > 90 % and accuracy (sizing error < 20 %). Sizing was carried out using algorithms developed at the University of Birmingham and discussed below. The drawback of the system is the time required to complete the detailed scans (i.e. return to the location of an identified crack to perform a re-scan for crack depth information) and analyse the data if used in on-line rail inspection, but the system can be run autonomously and the data analysis can be quicker with improved computer processing capability. Trials in a laboratory and on rails with artificial defects have been reported [128].

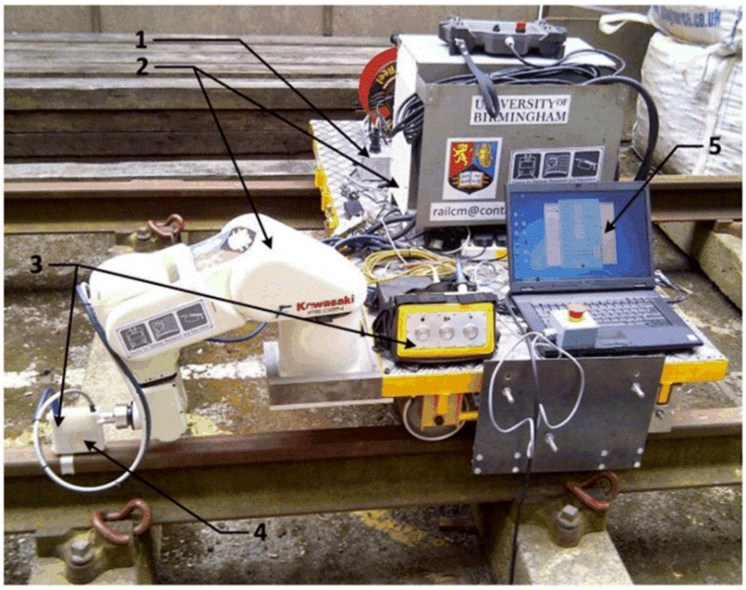

Figure 2.20 The automatic robotic ACFM inspection system (1-Motion controller, 2-Robotic arm, 3-ACFM sensor, 4-Laser sensor, 5-IUI software) [140].

A novel linear (1-D) ACFM array probe was developed for inspection of large metal surfaces [141]. Each element of the linear array consists of a linear sensing coil and a rhombic exciting coil arranged specifically for high sensitivity; the arrangement characterised by sequential switching allows the probe array to inspect large components with a length up to 2 meters. Structural optimization of the ACFM array probe (2-D) has been carried out with the installation of a double U-shape orthogonal inducer, which extends the inspected direction related to surface cracks and decreases the loss of magnetic flux in comparison to a single rectangular inducer [142]. The array probe is relative insensitive to lift-off up to 1 mm and experimental verifications showed that the probe has an accuracy of 5.5 % for sizing an artificial semi-elliptical crack with surface length of 47 mm and pocket length of 5 mm (crack machined vertically into the steel plate); the accuracy (average of 10 times results) was obtained by comparing the experimental measurements with the actual crack dimensions. A hybrid inspection system was also developed using an ACFM probe and surface magnetic field measurement (SMFM), which is an eddy-current based technique that can enhance the reliability of the ACFM sensor in real-time rapid scanning [143]. The interpretation of signals then become important as hybrid signals will present when detecting and sizing the crack. The developed signal processing technique was reported to work satisfactorily for deep cracks (> 5 mm) and a scan speed of 20 mm/s can be achieved.

The capability of the ACFM technique to monitor cracks growth was also reported [144]. ACFM array probes consisting of 8 sensing coils spaced at 10 mm was used to monitor crack growth in a weld in a high strength steel under four point bending at a frequency of 2 Hz and a stress range up to 200 MPa. The crack aspect ratio was 5 (the crack was found to be 50 mm in length and 10 mm in depth) and the weld toe stress concentration factor was absent, therefore the crack initiation position was not known and the ACFM system was unable to monitor the crack until the crack depth was significant (e.g. > 1 mm deep).

Evaluation of crack size using an ACFM pencil probe is most accurate when moving the probe along the single crack with the probe centre over the crack. However during inspection of real components the probe path inevitably deviates from the ideal position. The influence of scanning at different angles to the crack, scanning with the probe at an offset position to the crack centre, scanning with different lift-off values and scanning with the probe tilted on the evaluation of crack depth using an ACFM pencil probe was analysed [145]. Results indicated that defect sensitivity and detectability would not be seriously affected by the lift-off up to 2 mm with the 5 kHz probe (for a crack with 30 mm surface length and 2 mm depth); it was reliable to detect a crack (40 mm in length and 4 mm in depth) on scanning 10 mm away from the crack centre with a reduction of amplitude of 45 % at 0 mm lift-off; the angle between the probe travel direction and crack orientation could be 20° without there being a significant decrease in Bx signal; the probe tilted at an angle of 20° gave an accurate depth estimation (error of 1.3 %) for the crack with surface length of 40 mm and pocket length of 4 mm but the error increased to 20 % when the tilt angle was increased to 40°. The study was carried out based on investigation of single surface-breaking cracks that are vertical into the specimen only.

Modelling work has also been carried out at the University of Birmingham to study the ACFM response to RCF cracks occurring in rails [20-22]. A 3D FEM model was developed using Comsol Multiphysics to simulate experimental measurements on surface-breaking cracks using an ACFM pencil probe. The model was established based on three reasonable simplifications: by using a uniform current input field to represent the induced current on the rail surface generated by the magnetic field of the exciting coil; a simulated scan line (instead of the sensing coil) is used for data extraction mimicking the physical inspection using an ACFM pencil probe; the morphology of RCF cracks being considered as planar semi-ellipses with different ellipse ratios (the semi-major axis to the semi-minor axis), normally at 1-1.75. The semi-ellipse and elliptical ratios were determined through extensive investigations of RCF cracks in broken rails, discussed in section 2.2.1 [3]. Experimental measurements on single and multiple cracks on a calibration rail was used to verify the model and the model therefore can be used for different scenarios of ACFM inspection and RCF cracks arrangement. Single RCF cracks with ellipse ratios of 1, 1.25, 1.5 and 1.7 have been studied using the model. Crack dimensions were chosen from the guidance diagram for crack classification used by Network Rail UK (Figure 2.7). The result indicated that the ACFM sensor is able to differentiate and size cracks from the light to the moderate category of the classification system, as the Bx signal begins to saturate at longer surface length, as shown in Figure 2.21 [20]. Any mismatch between probe angle and crack orientation decreases the accuracy of the size estimation but an offset of ±10° was reported to have a minor influence on the Bx signals and hence crack sizing [20].

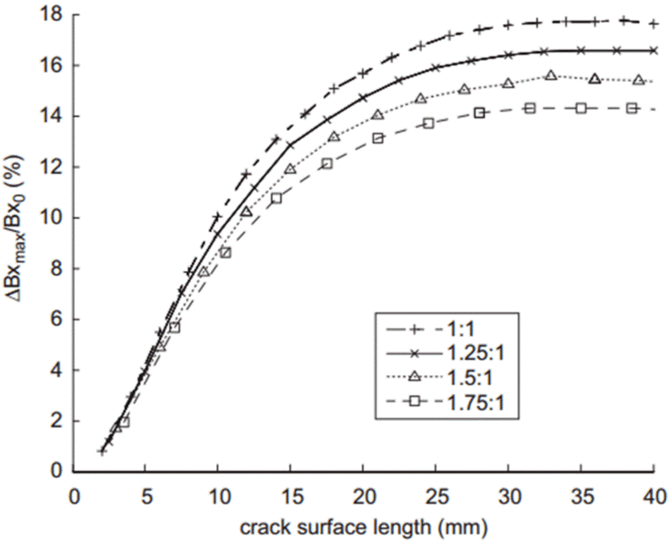

Figure 2.21 Normalised maximum Bx change with crack surface length for single RCF cracks with semi-elliptical ratios from 1 to 1.75 [20].

A further study has considered ACFM signal responses to multiple RCF cracks in a cluster [20, 21]. Figure. 2.22 shows that the Bx signals become deeper and wider when the crack number increases for a crack cluster with crack spacing of 1 mm, but the signal begins to saturate at a certain number of cracks (approximately 14-16 in Figure 2.22a). Furthermore, for closely spaced cracks (< 5 mm), the Bx signal will present a single trough whose depth is greater than that of the individual trough for a single crack with the same size (as shown in Figure 2.22b) for scanning at a lift-off of 0 mm. This will lead to an overestimation of the crack pocket length if the crack number in a cluster is not known and sizing based on the single crack algorithm is used. The Bx signal presents in the form of individual troughs for each crack within the cluster when the spacing is larger than 5 mm, for the other parameters studied (e.g. lift-off), but the depth predicted is still greater than that for an isolated crack of the same size as those in the cluster. Therefore, it is necessary to identify the crack number, the crack spacing and the crack surface length of crack clusters so that the pocket length of cracks in the cluster can be correctly sized. The modelling study was based on uniform sized cracks (semi-ellipse) in clusters with different crack spacing and crack number, however no research considering crack clusters with non-uniformly sized cracks (different lengths and depths of individual cracks and different spacings between individual cracks) has been reported.

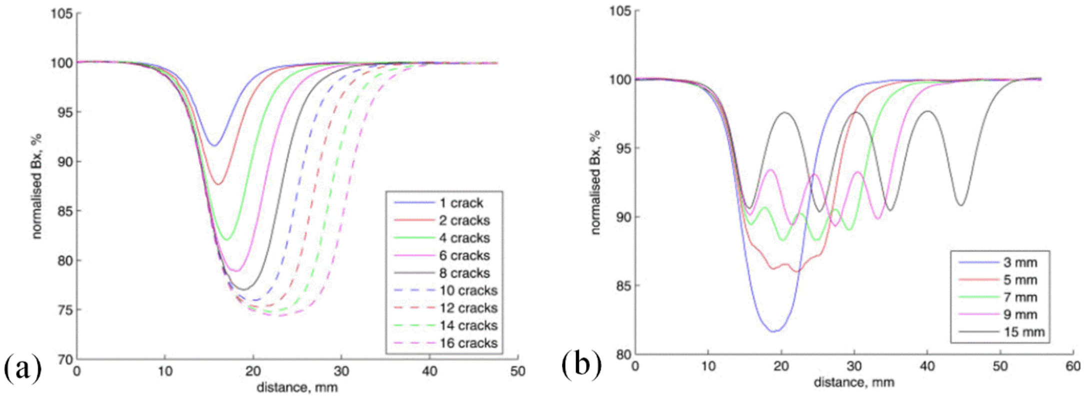

Figure 2.22 Normalised Bx signals with (a) crack number (crack spacing 1 mm); (b) crack spacing (4 cracks) for multiple cracks in a cluster where each crack has the same semi-ellipse (surface length 10 mm, pocket length 4 mm, width 0.5 mm, horizontal angle 32°, vertical angle 25°) [21].

It has been shown that the subsurface portion of a heavy or severe crack may propagate significantly beyond the surface-breaking component [3] (see discussion in section 2.2.1). A simulated ACFM scan over such crack was made along the surface-breaking component at 0 mm lift-off with the current flowing perpendicular to the surface component, and the result showed that the ACFM signal cannot detect the deepest part of the crack (i.e. not below the surface breaking component) with the Bx signal showing a similar level to that for a regular semi-ellipse crack with the same surface length. This indicated that large RCF cracks with complex shape may not be accurately estimated using ACFM and therefore accurate sizing should be limited to light to moderate cracks, which typically have semi-elliptical shapes [20].

A full ACFM probe model using a field generated by simulating the coils has also been developed (the modelling results discussion above have been for a uniform field model). The model more accurately simulates the field distribution generated by the exciting coil above the inspected sample and can be used to visualise how the generated field interacts with the sample and the crack, as shown in Figure 2.23 [146]. The probe model has been used to size surface-breaking cracks (a 50×5 mm^2 and a 20×2 mm^2 semi-elliptical EDM notch) in a welded steel sample. The modelling Bx shows a difference of approx. 1.1 % for the 50×5 mm^2 notch and a difference of approx. 0.8 % for the 20×2 mm^2 notch. Bx signal from a uniform field model agrees well with the experiment for the 50×5 mm^2 notch but shows a difference of approx. 3.2 % for the 20×2 mm^2 notch. The probe model gives a better prediction for the smaller surface-breaking crack (20×2 mm^2). However, the probe model can only evaluate the magnetic field where the sensing coil is located in a single model run and the geometry of the sensor needs to be re-located in order to simulate the physical probe measurement when the probe is moved along the surface-breaking component of the crack. In order to achieve continuous data, the model needs to be re-built and re-meshed which increases the solving time compared to the uniform field model if the crack is great in size and is locating in a component with complex structure.

The uniform field model has been used to investigate the ACFM responses through conductive coatings such as flame-sprayed aluminium or zinc galvanising [146]. The results show that for the case of the coated plate with the crack breaking through the coating, the current flow concentrates in the coating layer which means less current flows along the cracks surface, leading to a decrease of magnetic strength over the middle of the crack, where the sensing coil can pick up the data to evaluate the crack pocket length. This causes the sizing algorithm to overestimate the crack depth. For the case where the crack breaks through to the sample surface but does not break through the coating, the model shows that the current flows over the crack and the crack is not detected if the coating is too thick (> 240 µm). The trough and peak of the Bz signal can still be present at a certain thickness of coating (400 µm) as some current can flow around the ends of the crack.

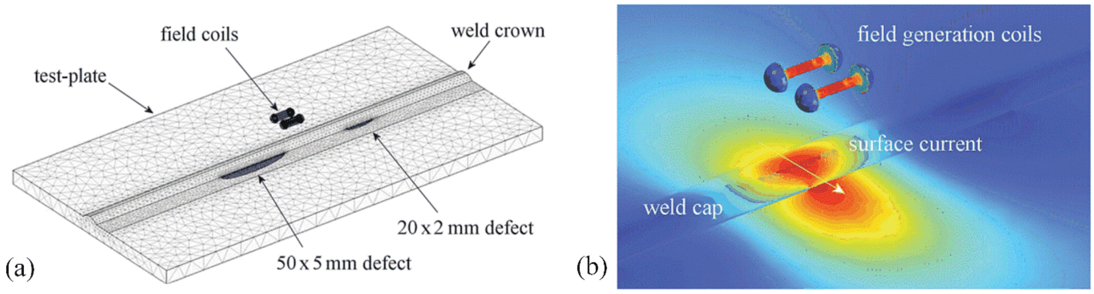

Figure 2.23 (a) Mesh of the ACFM probe model showing the geometry of the exciting coils above the weld component with surface-breaking cracks; (b) Contour plots showing the generated surface current across a weld [146].

Modelling the influences of induced frequency and lift-off have been carried out in order to design and build an ACFM prototype system with a U-shaped probe [147, 148]. The modelling results show that the induced magnetic field attenuates with an increase in inducing frequency while the sensitivity and crack quantification error can be improved. The optimum frequency used in the U-shaped prototype was determined as 6 kHz to guarantee the effectiveness of signals while achieving a satisfactory sensitivity and accuracy; the sensitivity is adversely influenced by an increase of probe lift-off and when the lift-off is small (< 3 mm), a slight variation will cause a large change in the signal.

As well as the modelling work being carried out to study how ACFM signals interact with RCF cracks, some research has focused on new approaches to the algorithms or “machine learning” for crack characterization using the ACFM signals [149-151]. A B-spline approach was proposed to filter noise in the raw ACFM signal obtained in a high-speed test for artificial notches. This approach can approximate a discrete signal using a continuous function while improving the ACFM signal reliability and the accuracy of characterisation by reducing the noise. The ACFM signal obtained through spinning rig tests (speed at 3.6 km/h) can be reproduced using a non-uniform B-spline approximation, which greatly reduced the noise in the raw signal and can be used to calculate the exact positions and the dimensions of artificial cracks on calibration rails [149]. A fuzzy learning approach was developed for estimating the depth and profile of fatigue cracks from ACFM signals. Three depth profiles were studied: semi-elliptical, symmetrical double-hump and asymmetric double-hump. The inversion technique showed accuracy and robustness in reconstructing the cracks of these shapes from both simulated and experimental ACFM signals [150]. A neural network was developed for characterization of multiple RCF cracks using simulated ACFM signals. The training signals for the neural network learning were obtained through the uniform field model in terms of the variations in crack number, crack spacing and crack size of clustered cracks. Validation showed that the neural network performed well in sizing uniformly sized crack clusters with an error of less than 20 % but the prediction errors for uneven clusters were slightly higher due to a lack of input data to train the neural network [151].

2.6 Summary

In this chapter the stresses causing RCF crack initiation and propagation in rails have been reviewed. The type and shape of RCF cracks occurring in the rail-wheel contact interface area have been reviewed with a focus on gauge corner cracking (GCG) and head checking (HC) cracks. The current state of rail NDT inspection methods were summarised and it has been shown that the ACFM technique shows advantages in detecting and sizing surface-breaking RCF cracks compared to other conventional methods such as ultrasonics and eddy currents. With the high sensitivity in inspecting small surface-breaking cracks as well as a good tolerance of sensor lift-off, ACFM can be used as instead of eddy currents or magnetic flux leakage to detect surface cracks in addition to ultrasonic methods for high-speed railway inspection. Therefore, the ACFM technique for crack detecting and characterization has been continuously developed experimentally and numerically not only for commercial application but also for the interpretation of ACFM signals for single or multiple RCF cracks.

Current work has been focused on the ACFM responses for single RCF cracks, with limited results reported for multiple cracks, and the relationship between ACFM signals and crack vertical angle (required for the determination of crack vertical depth for angled cracks) has not been reported. As RCF cracks usually propagate at shallow angles into rails presenting in the form of clusters, it is significant for the development of crack characterisation using NDT as well as the application of the ACFM technique that ACFM responses to multiple RCF cracks concerning variations in crack surface length, crack spacing and crack vertical angle, etc., should be investigated, which will be discussed in the following chapters of the present work.

3. Modelling and experimental procedure

The primary objectives of the current study are: to extend ACFM characterization for single RCF cracks to give information on the vertical propagation angle and hence the vertical depth, determined from the vertical angle and pocket length (shown in Figure 1.1) using an FEM model (Comsol Multiphysics); to model ACFM responses for multiple RCF cracks (uniformly and non-uniformly sized) together with the influence of crack vertical angle; to validate all modelling results using both artificial calibration cracks and railhead samples with real RCF cracks taken from service (where X-ray tomography and progress milling was carried out to investigate the crack profiles to compare to the model prediction).

3.1 Model description

3.1.1 Governing equations

Mathematical models have been established to calculate the current flow and thus the electromagnetic field distribution around surface-breaking cracks. The assumptions of these models mainly are: regular crack shapes (semi-ellipse or rectangle) and the skin depth of the electromagnetic field in the metal is relative small compared with the crack dimensions. The description of models and the solution of equations can be found in [152-154]. These mathematical models provide the theoretical foundation of more general FEM software (e.g. Comsol Multiphysics) for resolving of thin-skin electromagnetic problems. In the present project, a three dimensional FEM model was developed using the ac/dc module in Comsol Multiphysics [23]. The model is based on solving Maxwell's equations using certain boundary conditions. The Maxwell's equations, in differential form for general time-varying fields can be written as [23]

$$\nabla \times H = J + \frac{\partial D}{\partial t} \tag{1}$$

$$\nabla \times E = -\frac{\partial B}{\partial t} \tag{2}$$

$$\nabla \cdot D = \rho \tag{3}$$

$$\nabla \cdot B = 0 \tag{4}$$

$$\nabla \cdot J = -\frac{\partial \rho}{\partial t} \tag{5}$$

where E is the electric field intensity; D is the electric flux density; H is the magnetic field intensity; B is the magnetic flux density; J is the current density; ρ is the electric charge density. The constitutive relationships can be expressed as

$$D = \varepsilon_0 E + P \tag{6}$$

$$B = \mu_0 (H + M) \tag{7}$$

$$J = \sigma E \tag{8}$$

where ε_0 is the permittivity of vacuum, μ_0 is the permeability of vacuum and σ is the electric conductivity. P is the electric polarization vector, which describes how a material is polarized when E is present, and is generally a function of E. The magnetization vector M describes how a material is magnetized when a magnetic field H is present.

For nonlinear materials, a generalized form of the constitutive relationships is used and the relationship for electric fields is

$$D = \varepsilon_0 \varepsilon_r E + D_r \tag{9}$$

the relationship for magnetic fields is

$$B = \mu_0 \mu_r H + B_r \tag{10}$$

and equation (8) can be generalized as

$$J = \sigma E + J^e \tag{11}$$

where D_r is the displacement when no electric field is present and B_r is the magnetic flux density when no magnetic field is present; J^e is the externally generated current.

The boundary conditions between two media in an electromagnetic problem can be expressed as

$$n_2 \times (E_1 - E_2) = 0 \tag{12}$$

$$n_2 \cdot (D_1 - D_2) = \rho_s \tag{13}$$

$$n_2 \times (H_1 - H_2) = J_s \tag{14}$$

$$n_2 \cdot (B_1 - B_2) = 0 \tag{15}$$

where ρ_s and J_s are the surface charge density and surface current density, respectively, and n_2 is the outward normal from medium 2. From these equations the interface condition for the current density can be derived

$$n_2 \cdot (J_1 - J_2) = -\frac{\partial \rho_s}{\partial t} \tag{16}$$

For an AC power electromagnetic problem, the relevant interface condition is equation (14). The magnetic field boundary condition is

$$n \times H = n \times H_0 \tag{17}$$

the surface current boundary condition is

$$-n \times H = J_S \tag{18}$$

$$n \times (H_1 - H_2) = J_S \tag{19}$$

the perfect magnetic conductor boundary condition is

$$n \times H = 0 \tag{20}$$

the magnetic potential boundary condition is

$$n \times A = n \times A_0 \tag{21}$$

the magnetic insulation boundary condition is

$$n \times A = 0 \tag{22}$$

and the continuity boundary condition is

$$n \times \left(H_1 - H_2\right) = 0 \tag{23}$$

3.1.2 Model setup

The FEM model used in the study consists of a block representing a section of rail with cracks at the surface of, and propagating into, the rail block and an air block above the rail section. The model geometry with a single semi-elliptical crack and the standard Cartesian coordinates are shown in Figure 3.1a. The current flows in the y-direction, which is perpendicular to the crack surface length. A perpendicular current orientation is selected to give the maximum Bx and Bz signals and represents the standard experimental procedure where the ACFM sensor is oriented parallel to the crack. A uniform magnetic field is induced above the rail surface mimicking the operation of the physical ACFM sensor. The uniform field model (different with the probe sensor model discussed in section 2.5) is selected because it provides a good simulate to the experiments and greatly decreases the computing time and data processing procedure (see discussion in section 2.5). The uniform magnetic field is generated by applying surface current boundary condition along the front, up and rear surfaces of the air block shown in Figure 3.1a. This allows a uniform current distribution at the interface between the air and the rail block.

Figure 3.1b shows the details of the meshing of the whole model; areas of refined mesh are applied to the crack, the rail surface and the domain from which the signals are extracted. The maximum element size applied to the crack surface and the crack refined area, i.e. the refined mesh block with size of 25×25×5 mm^3 under the rail surface, are 0.1 mm and 0.5 mm, respectively and both have an element growth ratio of 1.5. The total number of elements for the model is in the order of 1.5×10^6. Crack width of 0.1, 0.3, 0.5, 0.7 and 1 mm were modelled; results shows that the difference of Bx value is 0.15 when the width increases from 0.1 to 0.5 mm whilst the difference is 0.65 when the width changes from 0.5 to 0.7 mm. It is impossible to introduce an extremely narrow crack (RCF cracks are of the order of several microns wide) into the model due to meshing and solving problems; therefore the crack width selected in the modelling is 0.5 mm, based on a compromise between solvability and the signal sensitivity to changes in crack width. This has previously been shown to give good results when comparing model and actual measurements for semi-elliptical cracks [20-22].

The crack shapes and dimensions used in the model are based on semi-ellipse shapes with certain ellipse ratios (e.g. 1, 1.25, 1.5 and 1.75) that have been shown to approximate real light to moderate RCF cracks (based on the Network Rail classification diagram, Figure 2.7) in rails removed from service [3, 20, 22]. The rail material considered in the model was 260 grade rail steel. It was assumed that the steel has an electrical conductivity of 5×10^6 S/m and relative permeability of 50 [22, 155]. The conductivity of air is assumed to be 50 S/m, as it aids the convergence of the model. The effect of varying the modelled permeability and conductivity values by 20% of their assumed values was relatively small: varying the permeability of 50 by ± 10 resulted in a change of Bx value of ± 0.18, and changing the electrical conductivity by $\pm 1\times10^6$ changed Bx value by ± 0.19 [22].

.

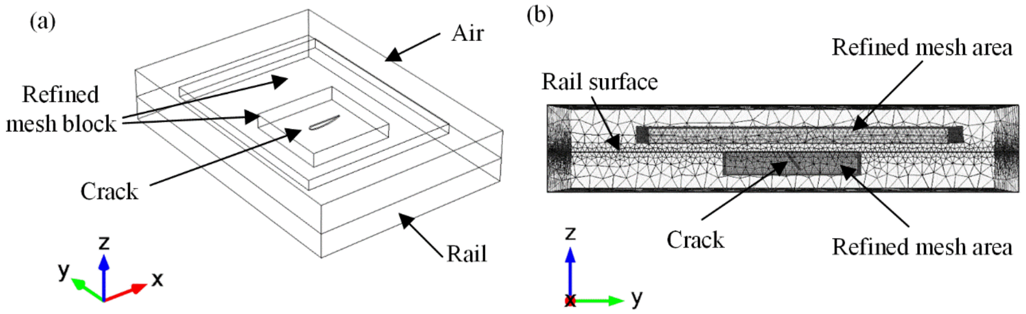

Figure 3.1 (a) Model geometry (for a single semi-elliptical crack) with two refined mesh blocks for the crack area and area of data extraction; (b) meshing of the model with refined mesh on the crack surface, crack area, rail surface and the area of data extraction.

In the present study, the full mesh boundary (FMB) condition is used rather than the impedance boundary (IB) condition, which was used in previous work [20, 22]. The impedance boundary condition can greatly reduce the meshing requirements and solving time by introducing current flowing only along the boundary, that is, the crack surface and the interface between air and rail surface. The IB method model was verified against experimental data for pocket length measurement, using the Bx signal, for cracks with vertical angles larger than or around 30° [20]. The FMB method meshes the whole domain with refined meshes for the area around the crack and the surface/near surface region. The FMB and IB models give comparable results for cracks with vertical angles larger than 30° but discrepancies are observed for shallow angle cracks (i.e. crack vertical angle less than 30°). The difference in using the FMB and IB conditions for shallow angle cracks will be discussed in section 4.1.

As the ACFM sensor gives results in analogue to digital conversion (ADC) units while modelling results are in SI units, the normalised Bx (equation 24) and Bz (equation 25) are used to compare the experimentally and numerically determined signals. The normalised maximum ΔBx (equation 26) is used to determine the crack pocket length and the Bz trough-peak ratio (equation 27) is proposed in the present study to determine the crack vertical angle. Full details are given in section 4.3

$$Normalised Bx = \frac{Bx}{Bx_0} \times 100\,\% \tag{24}$$

$$Normalised\ Bz = \frac{Bz - Bz_0}{Bz_{\max} - Bz_0} \times 100\,\% \tag{25}$$

$$Normalised \Delta Bx_{\max} = \frac{Bx_0 - Bx_{\min}}{Bx_0} \times 100\,\% \tag{26}$$

$$Bz\ trough - peak\ ratio = \frac{Bz_{trough}}{Bz_{peak}} \tag{27}$$

where Bx_0 and Bz_0 are the background signals of the x and z-components of the magnetic fields, respectively; the Bx_{min} is the minimum value of the Bx signal; the Bz_0 takes a value of 0 % and the maximum value recorded by the measurement line, Bz_{max}, denotes the signal strength of 100 %; Bz_{trough} is the value at the trough of the Bz signal and Bz_{peak} is the value at the peak of the Bz signal.

3.1.3 Current and Magnetic field

Figure 3.2 shows a typical result from the model of how the current and magnetic field distribute around a semi-elliptical surface-breaking crack. For a single surface-breaking crack, as shown in Figure 1.1 and Figure 3.2, ACFM can give an estimation of the physical length of propagation of the crack into the material, known as the pocket length, by measuring the perturbations in the x-component of the magnetic field (the Bx signal, extracted along the measurement path that is parallel to the crack opening). As observed in Figure 3.2a, the Bx trough is generated because the current flowing down and along the crack surface leads to a decrease in the current flow through the crack, therefore reducing the strength of the magnetic field above the middle of the crack. The Bx signal can be used to effectively estimate the pocket length for surface-breaking cracks with a semi-elliptical shape whose surface length is less than 20 mm and pocket length is less than 10 mm [20, 156], as discussed in section 2.5.

It is shown in Figure 3.2b that the current flows clockwise or anticlockwise around the ends of the crack, generating a fluctuation in the z-component of the magnetic field, Bz. The Bz signal (extracted along the measurement path that is parallel to the crack opening) is used to determine the crack surface length by measuring the perturbations (trough to peak position along the x-axis) provided that the ACFM sensor is oriented along the crack such that current flows perpendicular to the crack. It has been shown that the distance between the Bz trough and peak gives a reasonable measurement of the crack surface length and that parameters such as sensor lift-off and crack elliptical ratio (surface length to twice pocket length) have only a small effect on this measurement [140, 157].

In the present study, the modelled Bz signals are also extracted from the magnetic field along a measurement line that is at 45° relative to the crack surface length and passes through the centre of the crack, at 0 mm lift off (as shown in Figure 3.2b). This mimics the ACFM sensor path across the centre of the crack used in the experiments, which is used because this path can best show the magnetic field variations caused by a change in the vertical propagation angle of the crack into the rail. The modelling results of using the Bz signal to indicate the crack vertical angle will be discussed in sections 4.2 and 4.3.

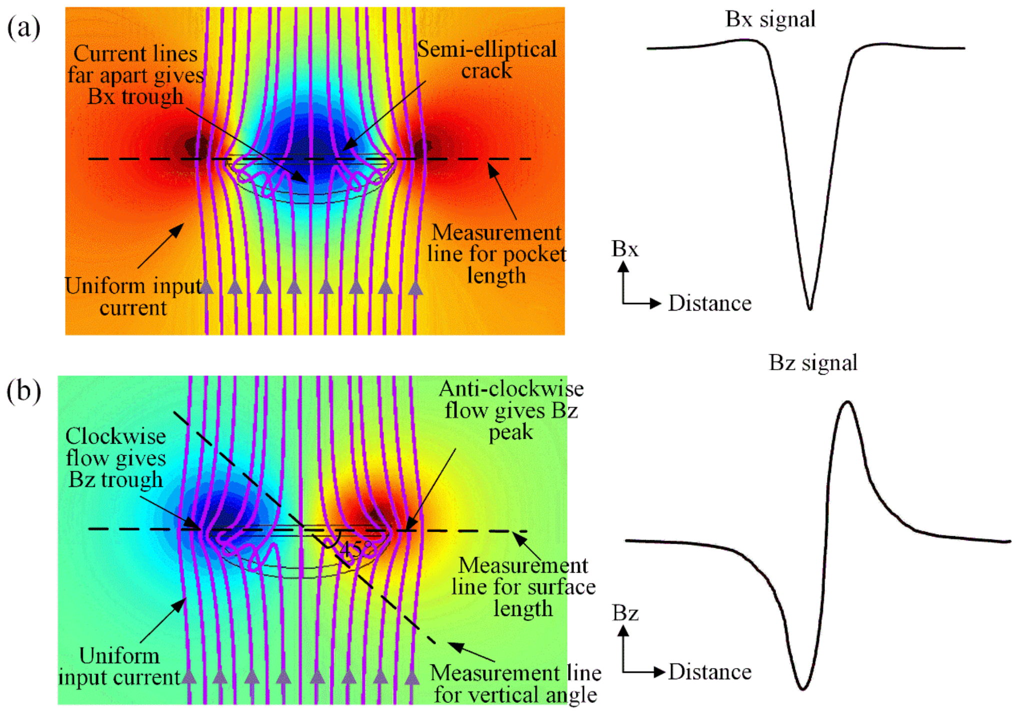

Figure 3.2 Current disturbed by a surface-breaking crack (of 8 mm surface length, 3.2 mm pocket length, 90° vertical angle) generating (a) Bx signal and (b) Bz signal; the contour plots show (a) the Bx magnetic field distribution and (b) the Bz magnetic field distribution around the crack; the dashed line parallel to the crack opening

indicates the path from which the Bx and Bz signals are extracted for crack pocket length and surface length determination respectively; the dashed line at 45° to the crack opening is the measurement line proposed in this study for crack vertical angle determination.

3.2 Samples and ACFM measurements

3.2.1 Calibration samples

Single and multiple angled cracks (schematically shown in Figure 3.3) with semi-elliptical shapes were electro discharge machined on a calibration plate and an unworn (new) rail, respectively to verify the modelling results for cracks with different vertical angles. A 5 kHz Amigo 255 pencil sensor, produced by TSC Inspection Systems, was manually used for the ACFM signal measurements. The orientation of the sensor was kept parallel to the surface-breaking component of the crack to ensure current flows perpendicular to the crack opening, in which case the field perturbation is a maximum. The sensor was held at 0 mm lift-off and moved by hand through the centre of the crack along a measurement line that is at 45° to the crack opening, as shown in Figure 3.3b.

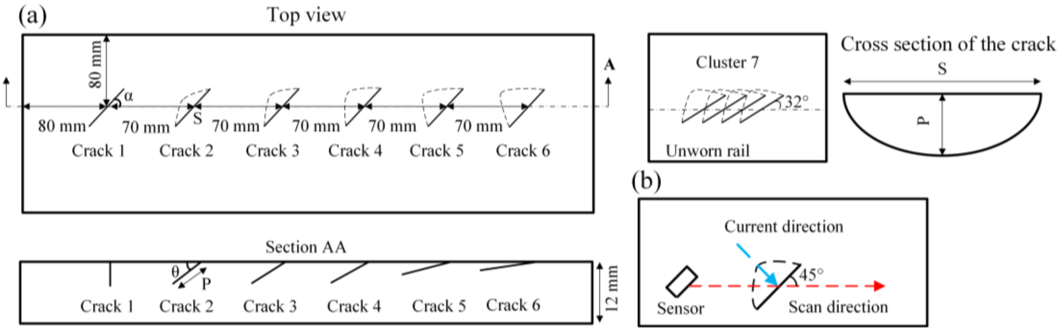

Figure 3.3 (a) Schematic diagram of the calibration plate with single angled artificial cracks and the unworn rail with an angled crack cluster, which have semi-ellipse shapes; (b) schematic diagram of the manually ACFM measurement procedure.

The desired and final machined angled crack dimensions are shown Table 3.1. A crack cluster (formed of 4 cracks) with vertical angle of 25° on an unworn rail (machined in a previous study [20, 21]), termed crack cluster 7 in Table 3.1, was also experimentally inspected to verify the modelling results for vertical angle of multiple cracks. There was significant variation between the designed and actual crack sizes and angles for cracks 2-4 due to the initial difficulties in machining the semi-ellipse shape and angled cracks. For cracks 5 and 6 the actual crack width is larger than the desired width (0.5 mm), at 1.5 mm (for 20° vertical angle) and 4 mm (for 10° vertical angle) due to machining difficulties for shallow cracks. For these cracks the measurement line passes through the centre of the crack opening of the crack face approached by the ACFM sensor. The widths of these calibration cracks (except for cracks 5 and 6) were 0.5 mm, measured parallel to the plate surface. This matches the crack width used in the modelling.

The asymmetry of crack profiles was also measured by inserting a fine copper wire into the crack slot from the middle point (0 mm) of the crack surface-breaking component and every 1 mm to the left (gives negative value) and right (gives positive value) covering the whole surface length. The measurement of the length that the copper wire inserted into the crack slot can indicate the pocket length. Table 3.2 shows pocket lengths measured at the middle point and at ±3 mm away from the middle point for cracks 1-6. It can be seen that the machined calibration cracks have asymmetric profiles into the steel plate and the influence on ACFM signals is discussed in sections 4.2.2 and 5.3.

The pocket length (P) refers to the maximum extent of the crack in its subsurface propagation direction and the vertical angle (θ) is the intersection angle between the material surface and the crack's subsurface propagation direction, as shown in Figure 1.1. Cracks are located far enough from each other as well as the plate edges to avoid any effect of interactions between neighbouring cracks and the edges on the ACFM signals. The results of model validation tests for the Bx and the Bz signals are shown in chapter 4.

Table 3.1 Designed and measured (in brackets when different from designed) crack dimensions for experimental validation of vertical angle (length measurement errors < 0.1 mm; angle measurement errors < 1°).

Crack (cluster)	1	2	3	4	5	6	7
Surface length (S), mm	8.0	8.0 (9.5)	8.0 (11.5)	8.0 (12.0)	8.0	8.0	10.0 (11.0)
Pocket length (P), mm	3.2	3.2 (5.0)	3.2 (5.0)	3.2 (4.0)	3.2	3.2	4.0 (3.0)
Horizontal angle (α), °	45	45 (36)	45 (25)	45 (19)	45	45	32
Vertical angle (θ), °	90	50 (61)	30 (51)	20 (41)	20 (21)	10 (12)	25 (30)
Crack number	1	1	1	1	1	1	4
Inner spacing (I), mm	-	-	-	-	-	-	4

Table 3.2 Pocket length measured at the middle point (of the surface breaking component) and ±3 mm away from the middle point showing the asymmetric shape of calibration cracks (length measurement errors < 0.1 mm).

Crack	1	2	3	4	5	6
Pocket length at +3 mm	1.9	3.6	3.3	2.9	2.3	2.4
Pocket length at middle point	3.2	4.7	4.6	3.8	3.2	3.1
Pocket length at -3 mm	2.0	3.3	2.8	2.0	1.5	1.4

To validate the pocket length predictions using the modelling results for multiple cracks, a calibration plate with different sized crack clusters (cracks machined vertically into the plate), as shown in Figure 3.4, was electro discharged machined. The shape of the cracks is semi ellipse and the designed dimensions for these clusters are listed in Table 3.3. As all these cracks are machined vertical into the plate (vertical angle of 90°), the dimensions were more accurately controlled. The pencil ACFM sensor with frequency of 5 kHz (produced by TSC Inspections) was also used in the manually ACFM measurement on multiple cracks. All measurements were carried out at 0 mm lift-off and the scanning procedure is similar to that in the single crack case, schematically shown in Figure 3.3b. The modelling results for multiple cracks and experimental validation are discussed in chapter 5.

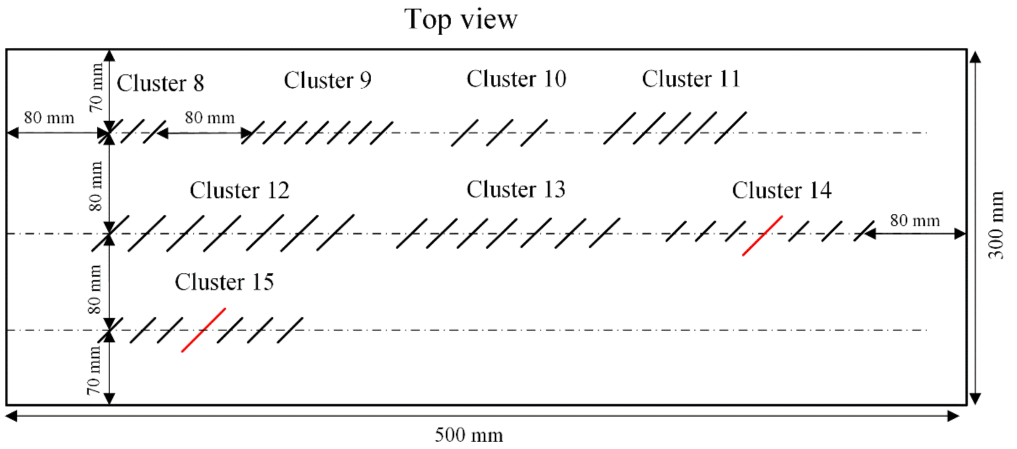

Figure 3.4 Schematic diagram of the calibration plate with vertical crack clusters.

Table 3.3 Designed crack dimensions used for the multiple cracks validation; all cracks in the clusters are the same size except for clusters 14 and 15 where the central crack is larger with surface length of 15 mm and pocket length of 6 mm (length measurement errors < 0.1 mm; angle measurement errors < 1°).

Crack cluster	8	9	10	11	12	13	14	15
Surface length (*S*), mm	5.0	7.0	11.0	15.0	21.0	14.0	5.0	10.0
Pocket length (*P*), mm	2.0	2.0	4.4	5.0	6.0	7.0	2.0	4.0
Elliptical ratio (*R*)	1.25	1.75	1.25	1.5	1.75	1	1.25	1.25
Inner spacing (*I*), mm	3.0	3.0	5.0	4.0	7.0	5.0	8.0	8.0
Crack number (*N*)	3	7	3	5	7	7	7	7
Horizontal angle (α), °	45	45	45	45	45	45	45	45
Vertical angle (θ), °	90	90	90	90	90	90	90	90

3.2.2 Samples taken from service

A single RCF crack (crack 16) and two RCF crack clusters (crack clusters 17 and 18) on rails taken from service (high rail from BNSF, Canada; manufacture year of 1972) were selected to be the subject of the case study in the present project. Figure 3.5 shows these cracks after MPI inspection (samples were first white painted and then the magnetic particle ink was sprayed to the sample surface; a magnetic yoke was used to magnetize the sample and magnetic particles can accumulate on the crack surface breaking component to enhance the crack appearance). Table 3.4 gives the crack dimensions. Crack clusters 17 and 18 can be considered as two separate clusters because the spacing between these two clusters is larger than 13 mm and the crack spacing needs to avoid the influence of adjacent cracks (for signal from the ACFM pencil probe) is normally 10 mm. There is a discontinuous crack (underlined by a blue line shown in Figure 3.5 and it can be seen from the sample cross section in Figure 3.9 that this crack disappears between clusters 17 and 18 due to the discontinuity) located between crack clusters 17 and 18. This crack will be influenced by the two clusters therefore is not investigated. Single crack 16 and crack cluster 17 and 18 were scanned by the ACFM probe sensor before destructive inspection (progressive milling) to investigate their inner dimensions into the rail (vertical angle and pocket length).

For the single crack 16, the sensor was held manually at 0 mm lift off and moved along the surface-breaking component for pocket length and across the centre of the crack at an angle of 45° to the crack opening (with an orientation parallel to the crack surface-breaking component) for vertical angle measurement. The crack clusters 17 and 18 were selected to be grid scanned using the ACFM probe sensor installed on a robotic arm (LR-Mate 200iD, FANUC UK Limited). The robotic arm allowed accurate control of lift off distance (0 mm in present study) between the single pencil probe and the railhead through the use of a laser range sensor (a commercial ACFM walking stick or array probe configuration would give constant lift off but was not available). Figure 3.6a shows the robotic arm used in the trial. The robotic arm was used to carry out 21 parallel scans (each scan 1 mm apart) forming the grid scanning area. The ACFM pencil sensor was held at 0 mm lift-off to the rail surface at 45° to the running direction (which is similar to the average horizontal angle of the inspected cracks). Figure 3.6b shows the ACFM pencil sensor installed on the robotic arm with the laser range sensor scanning over the RCF crack cluster.

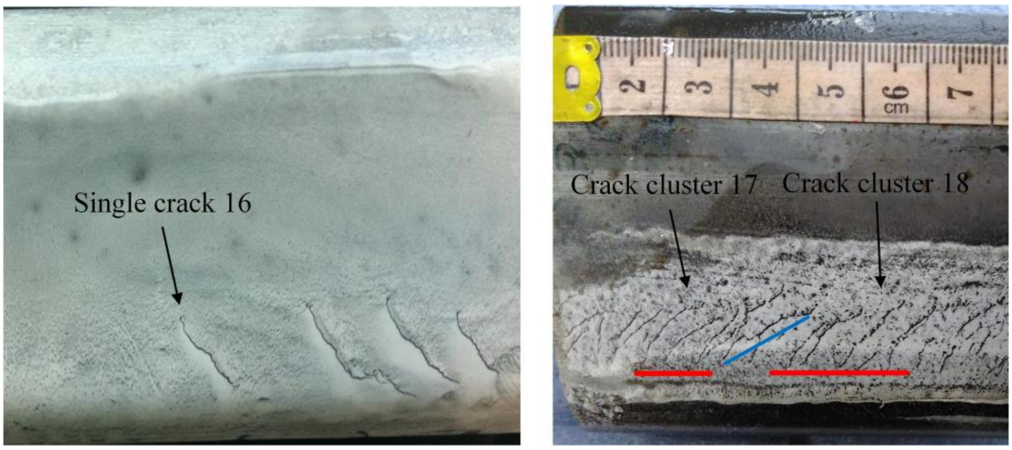

Figure 3.5 Images of sample taken on rails removed from service showing single and multiple cracks inspected by manual and robotic ACFM, respectively.

Table 3.4 Summary of the crack dimensions measured on real RCF cracks (average values are shown for crack clusters 17 and 18 with the range of values shown in bracket; length measurement errors < 0.1 mm; angle measurement errors < 1°).

Crack (cluster)	16	17	18
Surface length (*S*), mm	12.6	11.6 (10.5-14.3)	12.7 (10.8-15.6)
Horizontal angle (α), °	53.2	43.3 (29.7-52.8)	43 (41.6-46.7)
Inner spacing (*I*), mm	-	3.9 (2.7-4.8)	4.4 (1.9-6.1)
Crack number (*N*)	1	4	4

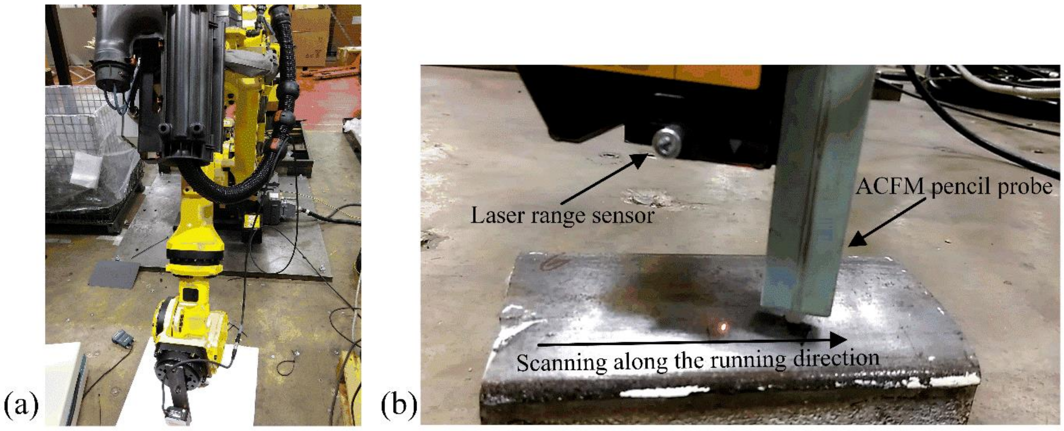

Figure 3.6 (a) The robotic arm used in the trial; (b) The ACFM probe sensor was moved along the running direction with an angle of 45° relative to the crack opening (such that the probe is parallel to most of the components of the RCF cracks) by robotic arm and the laser ranging sensor was used to maintain a constant ACFM sensor lift-off.

The Bx and Bz signals obtained from the grid scan were used to construct the magnetic field mappings of the x-component and z-component fields (i.e. contour plot using experimental signals, as numerically shown in Figure 3.2). The mappings provide a more complete image of the magnetic field distribution over the cracks compared to the signal obtained from a single scan, especially for crack clusters, and facilitate determination of crack surface lengths, pocket lengths and vertical angles. In addition, the mappings can indicate the positions of maximum or minimum values of magnetic field in relation to the crack surface-breaking component. This is useful for cracks with asymmetrical shapes as the maximum or minimum values are not necessarily beneath the centre position of the crack surface-breaking component.

3.3 X-ray tomography and progressive milling

After ACFM measurements the rail samples (the single crack 16 and the crack clusters 17 and 18) taken from service were destructive inspected (progressive milled) to investigate crack profiles and therefore provide the actual dimensions of crack pocket length, vertical angle and vertical depth for comparison with the predicted results. Figure 3.7 shows the progressive milling procedure for crack clusters. The milling direction is parallel to the running direction and milling started at 9 mm away from the gauge side, which corresponded to the start of the cracks and a total 29 mm was milled off (each milling removed 1 mm of the material) until all inspected cracks have been removed.

The single crack 16 was also inspected using X-ray tomography. Figure 3.8a shows the sectioning and imaging direction for the single crack 16. The direction is parallel with the main crack opening component such that the real maximum pocket length can be achieved from the tomography results. Figure 3.8b shows an X-ray tomography image for crack 16, indicating the maximum pocket length of 6.0 mm (errors < 0.12 mm) with a vertical angle of 25.7° (errors < 0.1°). Figure 3.9 shows an example of the cross section image of crack clusters 17 and 18 when the railhead sample was milled vertically to remove 16 mm from the gauge side.

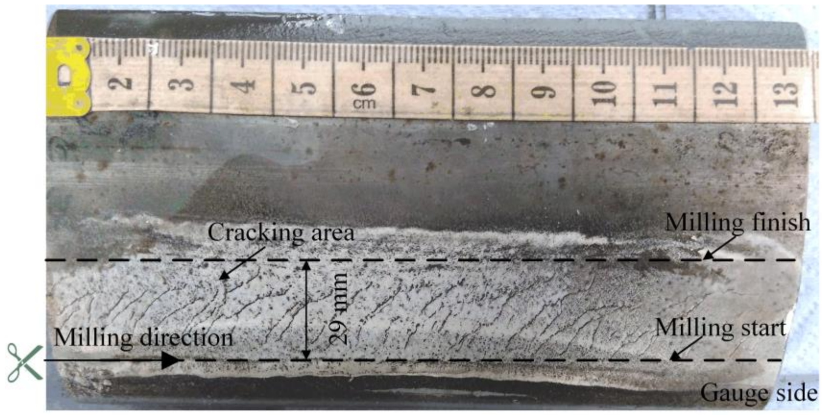

Figure 3.7 Progressive milling of crack clusters 17 and 18 on the sample taken from service.

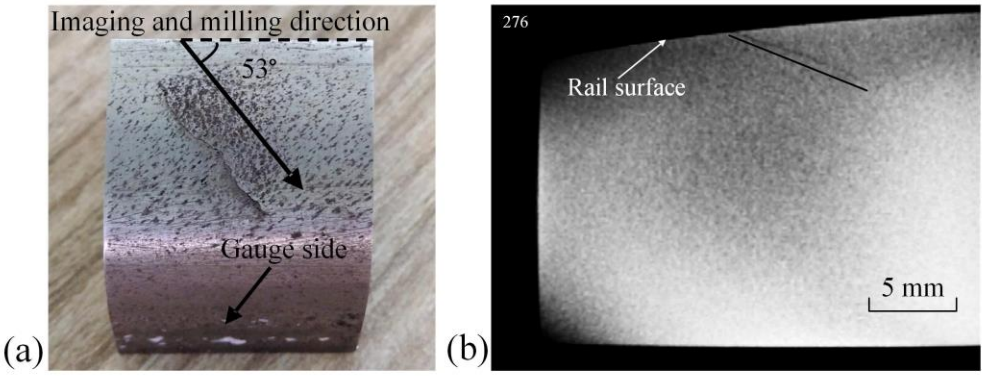

Figure 3.8 (a) Single crack 16 removed from the railhead sample and the imaging and the milling direction; (b) X-ray tomography image for crack 16 showing the position of the maximum pocket length of 6.0 mm (errors < 0.12 mm) and the vertical angle of 25.7° (errors < 0.1°).

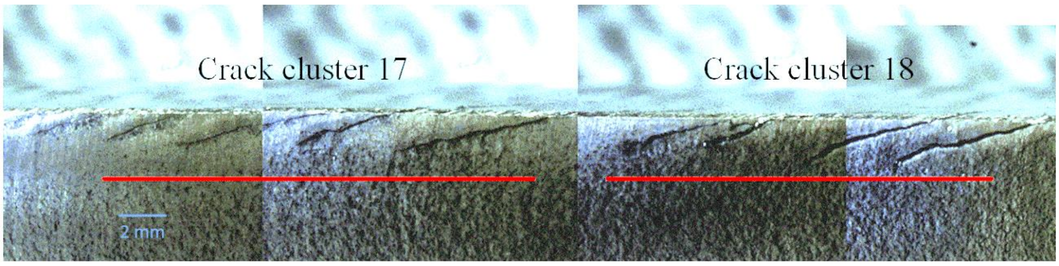

Figure 3.9 Cross section for crack clusters 17 and 18 showing the profile of the crack propagating into the rail when the rail sample was milled to remove 16 mm from the gauge side.

The results of measurements on these RCF cracks in the rails taken from service and the comparison with the predictions of crack dimensions, i.e. crack vertical angle, crack pocket length and crack vertical depth, together with the results of progressive milling are discussed in the case study in chapter 7.

3.4 Summary

This chapter introduces the FEM model used to study the ACFM responses to single and multiple RCF cracks and how it can be used to approximate the physical ACFM measurements. Modelling results in the study will be verified by experimental measurement on calibration cracks using an ACFM pencil probe and details of the calibration cracks are provided in this chapter. Cracks on rails taken from service were investigated as case studies to show the accuracy using the modelling results in the study. The inspection methods of MPI, ACFM measurement, X-ray tomography, progressive milling are introduced in this chapter.

4. Influence of the vertical angle on ACFM signals

4.1 Introduction

RCF cracks have been reported to initially grow at a vertical angle of 10°-30° until they reach a critical depth of 5 mm before they probably turn down causing rail break, or turn up to the rail surface resulting in a spall [3]. From a rail maintenance point of view for light to moderate cracks (categorized by Network Rail, as shown in Figure 2.7 [20]), it is important to know the vertical crack depth, which varies depending on the crack pocket length and vertical angle, as this determines the amount of rail to be ground off to eliminate the RCF cracks before they grow to a severe size. It has been found that the Bx signal from ACFM inspection can be used to determine the pocket length of cracks in the light to moderate category, whereas cracks with larger surface length (e.g. in the heavy to severe category) lead to saturation in the minimum Bx value [20]. In addition, the visual length-depth guidance diagram (Figure 2.7) cannot give the explicit length and depth relationships for RCF cracks due to the variability in vertical propagation angles and surface length to depth ratios [20].

Currently for EM-based techniques, the determination of crack vertical depth requires an assumed propagation angle into the rail since no method to detect the crack vertical angle using EM signals has been reported previously. Other NDT studies on surface-breaking cracks are limited to cracks that propagate vertically, i.e. where vertical depth is equal to pocket length, or use an assumption about the angle of propagation to determine the vertical depth to which the crack has penetrated [20, 158-160]. A common method used for angled crack characterization is ultrasonic detection, for example using tip reflections for long cracks [161, 162] or analysing the various components of Rayleigh waves in the vicinity of small cracks with pocket lengths less than 5 mm [95, 163, 164]. Improvements in ultrasonic array post-processing can give more accurate sizing than methods which rely on tip diffraction for small cracks, for example use of the half-skip total focussing method was reported to improve the depth estimation of small back wall surface-breaking cracks compared to standard time-of-flight measurements, including for angled cracks, although shallow angle cracks were not assessed [165]. Generally, however, ultrasonic detection used in the rail industry is inaccurate for the small surface-breaking cracks (< 4 mm in depth) occurring in clusters that correspond to rolling contact fatigue (RCF) cracks in the early stage of development. In addition some severe internal defects can be masked by small surface cracks (shadowing effect), thus giving an underestimated size [1, 14].

The present chapter reports the relationship between the ACFM Bz signal and the vertical angle of RCF cracks, which then allows the crack vertical depth to be determined via a simple calculation using the pocket length determined from the Bx signal. Section 4.2 presents an analysis of the sensitivity of the Bx signal to crack vertical angles in the range 10°-90°. Section 4.3 quantitatively discusses the relationship between the Bz signal and the vertical angle, in which the reasons for the Bz magnetic field being sensitive to crack vertical angle are explained. The Bz trough-peak ratio is proposed as a measure for the crack vertical angle in section 4.4. The modelling results are also experimentally verified using single and multiple machined cracks in calibration samples.

4.2 Influence of crack vertical angle on Bx signals

4.2.1 Comparison between model boundary conditions

In the present study, the full mesh boundary (FMB) condition is used for the consideration of crack vertical angle determination rather than the impedance boundary (IB) condition, which was used in previous work [20, 22]. The IB condition can greatly reduce the meshing requirements and solving time by introducing current flowing only along the boundary, that is, the crack surface and the interface between air and rail surface. The IB method model was verified against experimental data for pocket length measurement, using the Bx signal, for cracks with vertical angles larger than or around 30° [20]. The full mesh boundary method meshes the whole domain with refined meshes for the area around the crack and the surface/near surface region.

Figure 4.1 shows the differences in the modelled Bx signal using these two boundary conditions for cracks with surface length of 8 mm and pocket length of 3.2 mm at different vertical angles. The results show that the Bx signals for vertical angles of

30° to 90° are similar for both boundary conditions (less than 0.53 difference). However, at shallow vertical angles, 20° and 10°, the results diverge, with the IB model Bx values remaining the same as for higher angles whilst the Bx values for the FMB model increase. When using the IB condition the current flow is completely bound to the material and crack surfaces regardless of the variation in vertical angle, therefore the current path for the estimation of pocket length remains the same. However, for the FMB condition the current path can deviate from the surfaces and take a shorter path back to the surface when that distance is similar to the skin depth. Therefore the trough in the Bx magnetic field (i.e. the negative-valued area of the x-component of the magnetic field shown in the middle of the crack in Figure 3.2a) moves away from the crack surface-breaking component on the side where the crack is propagating into the rail.

As the ACFM measurement scan is taken at 45° to the crack surface component through its centre, the measurement line does not cross the lowest point of the negative-valued area of Bx and the minimum Bx value recorded (i.e. normalised minimum Bx) during the scan therefore is not the minimum value of the negative-valued area (it visualised in Figure 4.4 that the measurement line does not cross the minimum value of the negative-valued are of Bx). This effect is significant at shallow vertical angles, because the Bx magnetic field moves further as vertical angle decreases from 30° to 10° than from 90° to 30°. It is shown in Tables 4.2 and 4.3 that the distance, Y_l or Y_r, from the Bz magnetic field to the crack surface-breaking component is longer when vertical angle decreases from 30° to 10° than from 90° to 30°; it is although the Bz magnetic field, the Bx magnetic field will show the same result. In addition, the minimum value of Bx magnetic field largely decreases in magnitude at shallow vertical angles. Therefore, the normalised minimum Bx for vertical angle less than 30° is greatly increased. Comparison of the modelled results to experimental data for Bx signals against vertical angles is given in section 4.2.2.

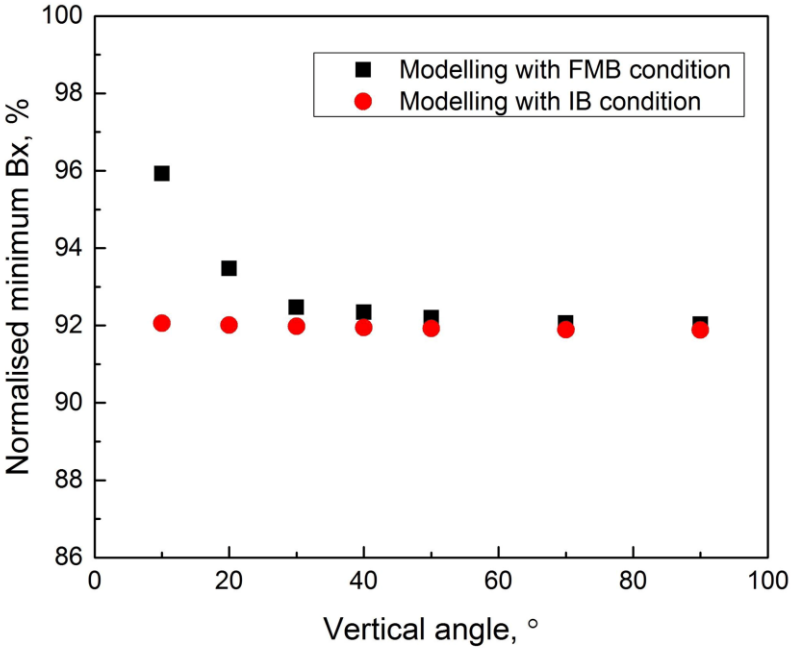

Figure 4.1 Bx responses to the crack vertical angle (cracks with surface length of 8 mm and pocket length of 3.2 mm) using the impedance boundary condition and full mesh boundary condition.

4.2.2 Sensitivity of Bx signals to crack vertical angle

In Figure 4.2 the normalised minimum Bx values for the measured dimensions of calibration cracks 1-6 obtained via modelling with IB and FMB conditions are shown. The experimental results for the calibration cracks with measured dimensions are also shown in Figure 4.2. It can be seen that the Bx does not show a regular relationship with the change of vertical angle, as discussed previously [20]. Modelling results with FMB are closer to the experimental results than those modelled with IB for all investigated vertical angles. The small offset between the model and experimental values are caused by the machined cracks having a slightly asymmetrical shape, as indicated in table 3.2.

As described in section 4.2.1 there is no significant change between Bx signals modelled with IB and FMB conditions when the vertical angle is between 30° and 90°. When the vertical angle changes to 20° the minimum normalised Bx values changes from 92.0 % (for IB) to 93.0 % (for FMB), which corresponds to a change in estimated pocket length of 0.91 mm, an underestimation of 28.6 %, based on the sizing algorithms previously developed for vertical cracks [20]. For the crack with a vertical angle of 10°, the predicted pocket length would be 1.6 mm, an underestimation of 50 %. Obviously Bx signals modelled using FMB condition can give a better fitting with experimental results with respect to the change of vertical angle. However, the Bx signal is insensitive to the vertical angle changing from 90° to 30° and therefore it cannot be used to determine the vertical angle as, in practice, both the crack pocket length and vertical angle are unknown.

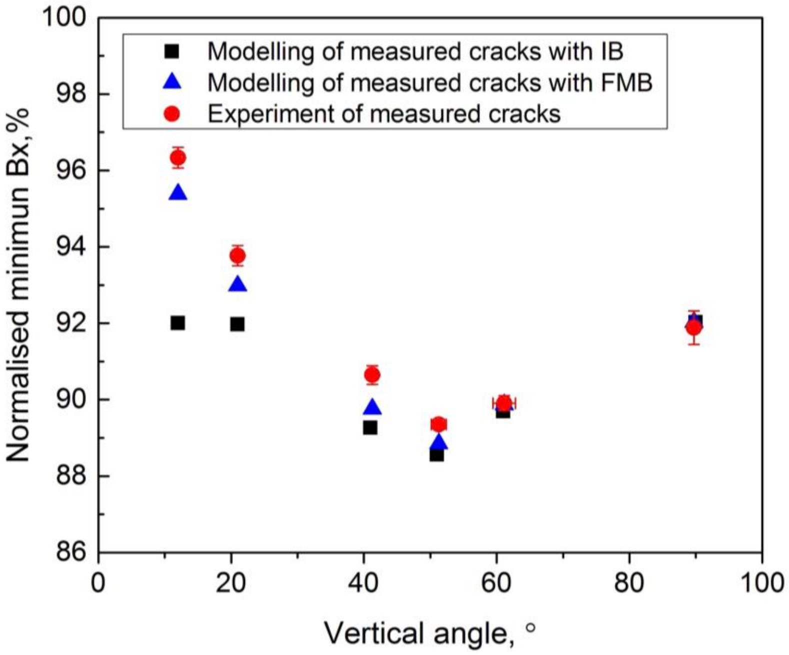

Figure 4.2 Modelling Bx signals for measured cracks 1-6 using IB and FMB and the experimental Bx signals for measured cracks with dimensions given in Table 3.1 (shown with the standard error).

4.3 Influence of crack vertical angle on Bz signals

4.3.1 Sensitivity of Bz signals to crack vertical angle

The Bz magnetic field is generated because of current rotation at the ends of the crack, as shown in figure 3.2a. This rotation is influenced by the vertical angle of the crack since the extent of current flow rotation decreases when the crack angle becomes shallow, i.e. lower values of vertical angle. The decrease in the rotation of current flow at the ends of the crack has two effects: a decrease in current intensity (peak and trough values of the Bz signal) and a shift in the maximum current intensity position, i.e. the current flow path gradually becomes more linear at the crack ends (see Figure 4.3a).

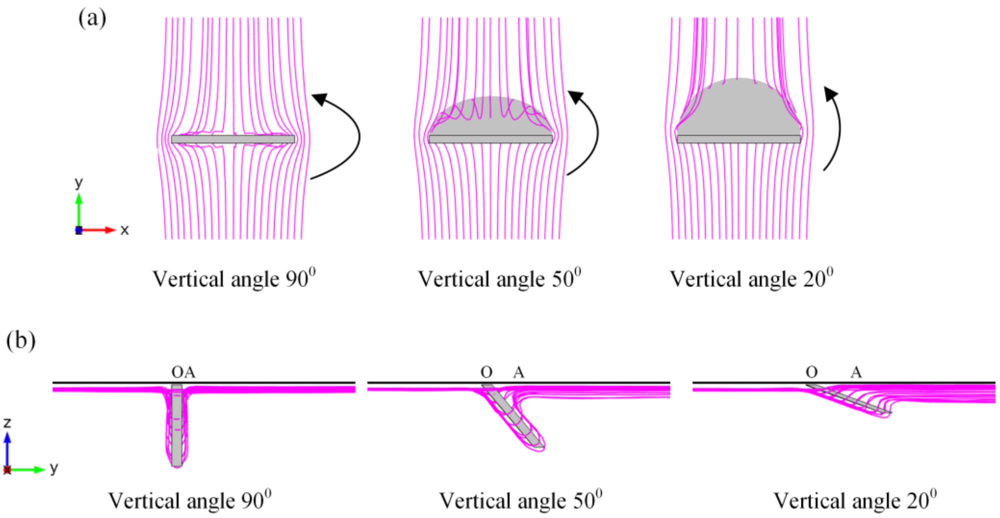

Figure 4.3 Current streamline flowing around a crack (8 mm surface length, 3.2 mm pocket length) with different vertical angles (a) the plan view showing the rotation of the streamlines at the crack ends being reduced for the smaller vertical angle cracks; (b) the lateral view showing the current intensity shifting at the surface with change in vertical crack angle (O represents the location of the crack opening and A indicates the location of the greatest current intensity at the surface).

Figure 4.3b shows a lateral view of the current flowing down and around the cracks with different vertical angles. For a single non-vertical crack with a semi-elliptical shape, the current flows along the crack surface and when it flows back to the sample surface, it takes a shorter pathway rather than being completely bound to the crack surface, as discussed earlier for the Bx signal. This causes the greatest current intensity behind the crack to move further from the crack opening, i.e. the shallower the crack vertical angle, the longer the distance between O and A, as shown in Figure 4.3b. Therefore, the negative-valued area and the positive-valued area of the Bz magnetic field will move away from the crack opening as the vertical angle decreases.

In order to investigate how the Bz magnetic field changes with the crack vertical angle, the concept of centre of gravity is introduced to consider the two influencing factors: the current intensity and the current intensity displacement. Figure 4.4

illustrates the Bz values and the coordinate system used in computing the Bz centre of gravity, which can be expressed in terms of X and Y components:

$$X_{CG} = \frac{|B_{zr}| X_r + |B_{zl}| X_l}{|B_{zr}| + |B_{zl}|} \tag{28}$$

$$Y_{CG} = \frac{|B_{zr}| Y_r + |B_{zl}| Y_l}{|B_{zr}| + |B_{zl}|} \tag{29}$$

where B_{zr}, B_{zl} are the maximum and the minimum values of the z-component of the magnetic field, respectively; X_r, Y_r are the coordinate values corresponding to the position of B_{zr}; X_l, Y_l are the coordinate values for B_{zl}.

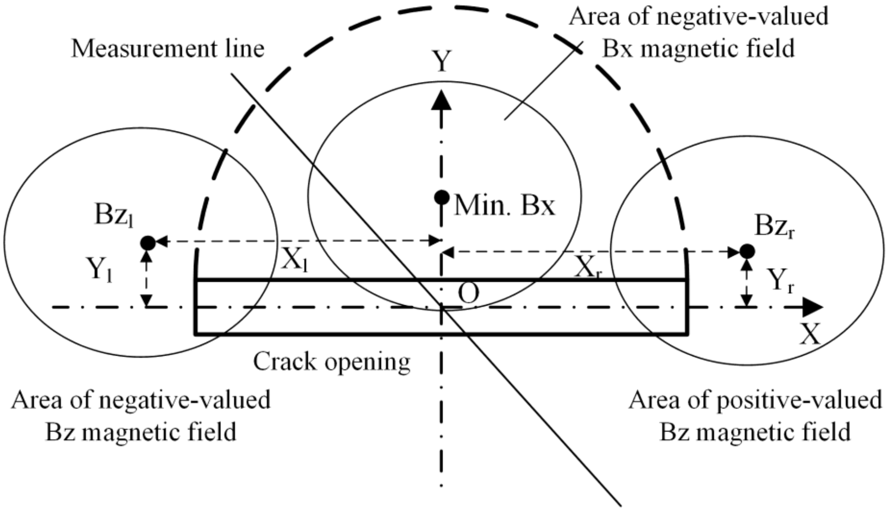

Figure 4.4 Schematic diagram of the parameters used for computing the centre of gravity of the Bz magnetic field (top view of the crack).

Table 4.1 and Table 4.2 give the computed results of the Bz centre of gravity using equations 28 and 29 for different vertical angles (θ) for cracks with surface lengths (S) of 8 mm and 21 mm. Each surface length contains two conditions of pocket length (P) corresponding to ellipse ratios of 1.75 and 1. The coordinate values are a few orders of magnitude higher than the magnetic field values so the centre of gravity is dominated by the coordinate values, particularly Y_{CG} is increased (i.e. Y_{CG} gradually moves in the Y direction) due to an increase in Y_r and Y_l (due to a decrease in vertical angle), although both the B_{zr} and the B_{zl} values decrease with the smaller vertical angle.

As the effect of changes in vertical angle are symmetric with respect to the Y axis, X_{CG} should have a value of 0 for each vertical angle but the computed results show some deviations from the Y axis; this is mainly caused by measuring error (due to meshing) when determining the X_r and the X_l values, but this has only a small effect on the final Bz trough-peak ratio, which is used to indicate the crack vertical angle, see section 4.4. Y_{CG} is the most important parameter; it increases with a decrease in vertical angle, and therefore can be used to show the asymmetrical distribution of the Bz magnetic field. However, some of the coordinate values are insensitive to the different vertical angles probably because the modelling mesh is insufficiently fine to differentiate these minute displacements, so the Y_{CG} values show no difference between 70° and 90° for cracks with surface length of 8 mm and 21 mm. The asymmetrical coordinate values at the same vertical angle (e.g. Y_r and Y_l for 50° vertical angle in Table 4.2) is probably also caused by measuring error; the maximum difference of 5.4 % between the Y_r and the Y_l coordinate values causes a change of 2.7 % in Y_{CG}, which, however, will not significantly influence the determination of the vertical angle through Y_{CG} values.

The computed results of Y_{CG} in Tables 4.1 and 4.2 suggest that the Bz magnetic field can be used to imply the variations in crack vertical angle for cracks with surface lengths of 8 mm and 21 mm. However, the Y_{CG} values show deviations for the larger crack (pocket length of 10.5 mm); for example, see the 10° case in Table 4.2 where Y_{CG} has a value of 16.20 for a pocket length of 6 mm compared to 19.60 for pocket length of 10.5 mm. This is because, the pocket length increases as the surface length and the influence of pocket length on the Y_{CG} value at a shallow angle becomes greater. Therefore, the Y_{CG} value is not only sensitive to vertical angle for small cracks (surface length of 8 mm based on the results presented) but also sensitive to longer crack pocket length (of larger cracks, e.g. 21 mm) at shallower vertical angles (30°-10°).

Table 4.1 The computed results of the Bz centre of gravity for cracks with 8 mm surface length (*S*) and two pocket lengths (*P*): 2.3 mm and 4.0 mm

Crack	θ	B_{zl}, 10^{-6} T	B_{zr}, 10^{-6} T	X_l, 10^{-3} m	X_r, 10^{-3} m	Y_l, 10^{-3} m	Y_r, 10^{-3} m	X_{CG}, 10^{-4}m	Y_{CG}, 10^{-4} m
S 8 *P* 2.3	10°	-3.56	3.55	-3.48	3.51	0.98	0.98	0.10	9.80
	30°	-8.03	8.02	-3.48	3.51	0.58	0.58	0.13	5.80
	50°	-9.09	9.08	-3.79	3.77	0.35	0.35	-0.12	3.50
	70°	-9.36	9.36	-3.79	3.77	0	0	-0.10	0
	90°	-9.46	9.45	-3.79	3.77	0	0	-0.12	0
S 8 *P* 4.0	10°	-7.05	7.05	-3.48	3.48	0.98	0.98	0	9.80
	30°	-11.17	11.18	-3.48	3.51	0.58	0.58	0.17	5.80
	50°	-11.68	11.68	-3.79	3.82	0.35	0.35	0.15	3.65
	70°	-11.85	11.85	-3.79	3.81	0	0	0.10	0
	90°	-11.91	11.91	-3.79	3.81	0	0	0.10	0

Table 4.2 The computed results of the Bz centre of gravity for cracks with 21 mm surface length (*S*) and two pocket lengths (*P*): 6.0 mm and 10.5 mm.

Crack	θ	B_{zl}, 10^{-6} T	B_{zr}, 10^{-6} T	X_l, 10^{-3} m	X_r, 10^{-3} m	Y_l, 10^{-3} m	Y_r, 10^{-3} m	X_{CG}, 10^{-4}m	Y_{CG}, 10^{-4}m
S 21 *P* 6.0	10°	-21.70	21.70	-8.32	8.30	1.62	1.62	-0.10	16.20
	30°	-29.03	29.03	-8.46	8.46	0.69	0.69	0	6.90
	50°	-29.77	29.79	-8.52	8.50	0.35	0.37	-0.07	3.60
	70°	-29.9	29.9	-8.64	8.67	0.18	0.18	0.15	0.18
	90°	-30.01	29.99	-8.89	8.86	0	0	-0.18	0

S 21 *P* 10.5	10°	-31.88	31.88	-8.42	8.40	1.96	1.96	-0.10	19.60
	30°	-36.43	36.47	-8.61	8.59	0.8	0.81	-0.05	8.05
	50°	-36.86	36.88	-8.75	8.76	0.35	0.37	0.07	3.60
	70°	-37.03	37.01	-8.91	8.92	0.18	0.18	0.03	0.18
	90°	-37.04	37.05	-9.03	9.00	0	0	-0.14	0

4.3.2 Use of Bz signals for vertical angle determination

Figure 4.5 shows the distribution of the Bz magnetic field above the semi-ellipse cracks with vertical angles of 90° and 10°. As the Bz centre of gravity shifts away from the centre of the crack surface breaking component onto the side where the crack propagates in the material with the change in vertical angle, the Bz signal extracted from a measurement line (as shown in Figure 4.5b) across the centre of the crack at a certain angle, taken as 45° in the present study, can detect the asymmetry in the Bz magnetic field; Figure 4.6 shows the Bz signal taken along this measurement line changing with crack vertical angle.

The Bz signal is symmetrical when the crack is vertical, as the maximum and minimum possible values of the z-component of the magnetic field and the distances from them to the measurement line are the same, as shown in Figure 4.5a. Therefore the Bz centre of gravity is at the origin (centre of the surface crack length) when the vertical angle is 90°. With a decrease in the vertical angle the Bz signal becomes more asymmetrical. The peak value of the Bz signal decreases as the Bz centre of gravity moves away from the measurement line. This results from the decrease in the maximum value of the z-component of the magnetic field (i.e. the decrease in current intensity) and the greater distance from this point to the measurement line (i.e. the shift in the current intensity), as shown in Figure 4.5b.

The trough of the Bz signal deepens at a smaller vertical angle as the distance from the negative area of the magnetic field dominates the Bz minimum values except for the case where the vertical angle is 10°. The negative area of the magnetic field approaches the measurement line leading to the lower minimum Bz value, although its absolute values decrease, which should deepen the Bz trough. However, as the vertical angle decreases to a shallower angle (e.g. 10°), the crack surface is closer to the rail surface and the current rotation at the ends of the crack is weak, which causes a larger decrease in the absolute values of the field. The negative area of the magnetic field is still approaching the measurement line but the magnetic field decays rapidly, therefore, the Bz trough value which is detected by the measurement line for the vertical angle of 10° is higher (see the trough in Figure. 4.6 for the 10° crack vertical angle).

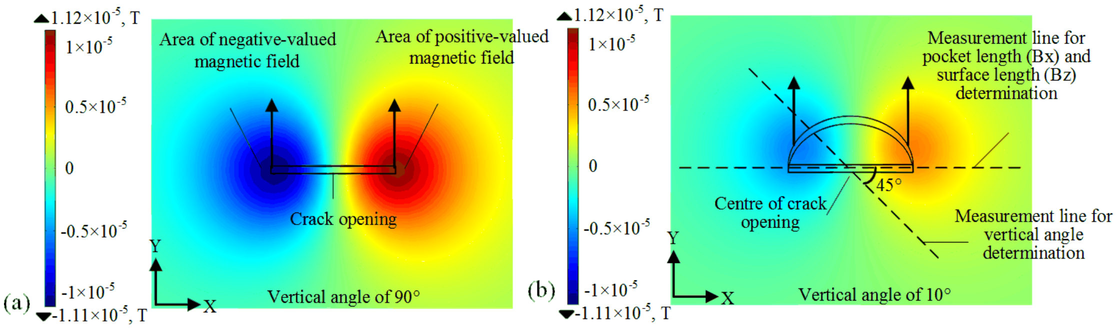

Figure 4.5 Contour plot of the z-component of the magnetic field above a semi-elliptical crack with vertical angle of (a) 90° and (b) 10°; arrows indicate both the negative and positive-valued area moving away from the crack opening component as vertical angle decreases; the measurement line parallel with the crack opening is used to obtain the Bx and Bz signals that can be used to estimate the crack pocket length and surface length respectively; the measurement line at an angle of 45° to the crack opening is for recording the Bz signals to determine the vertical angle.

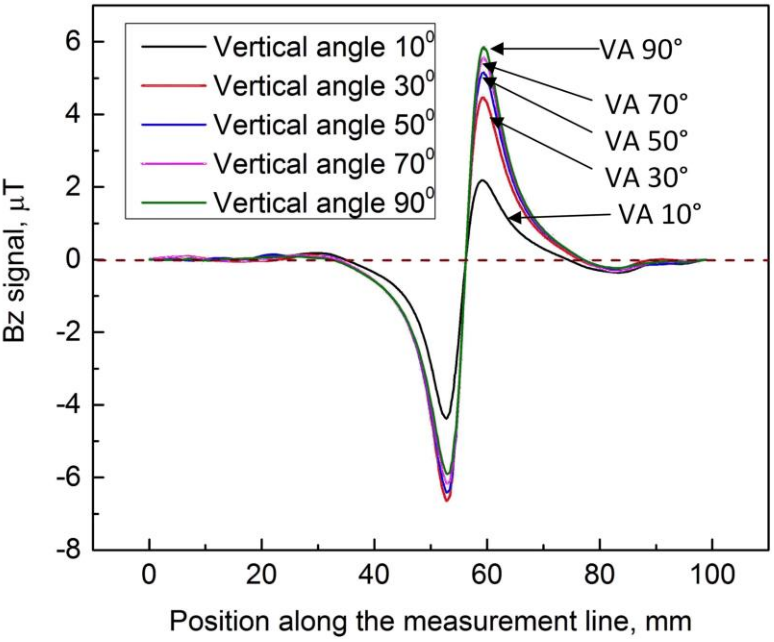

Figure 4.6 The Bz signal, for a crack with surface length of 8 mm, pocket length of 3.2 mm and different vertical angles, showing the asymmetry caused by the smaller vertical angles.

4.4 Crack vertical angle determination

4.4.1 Bz trough-peak ratio

In order to quantify the change in the Bz signal with the crack vertical angle, the Bz trough-peak ratio (see equation 27) of the Bz signal taken along the measurement line, which is 45° relative to the crack surface-breaking component, is proposed. In addition, although it is easy to observe from contour plots (e.g. Figure 4.5) that the Bz magnetic field changes with vertical angle, contour plots are established based on theoretical modelling and it is not possible to obtain them experimentally with a single pass of a single ACFM probe, and is time consuming if using a grid scan to generate a contour plot. The Bz trough-peak ratio can represent the magnitude of the trough value to the peak value in the Bz signal along a single measurement line, thus showing the asymmetric Bz magnetic distribution caused by the crack vertical angle.

Figure 4.7 shows the modelling and experimental Bz trough-peak ratio obtained from the 45° measurement line (45° with respect to the crack surface length) for single (cracks 1-6) and multiple (crack cluster 7) calibration cracks with a range of vertical angles between 12° and 90°. Modelling has been carried out for the calibration cracks. Five measurements have been carried out for each of the experimental point (therefor the error bars shown in Figure 4.7). The experimental measurements agree with the modelling results for the calibration cracks in that they show the same tendency that the ratio decreases as the crack becomes shallower. The Bz trough-peak ratio changes correspondingly with the vertical angle and it changes rapidly when the vertical angle is smaller than 30° due to the strong asymmetry in the Bz magnetic field.

For the single cracks, the experimental Bz trough-peak ratios are lower than the modelling results with a mean difference of 6.2 %, indicating that the magnitude of trough and peak values for measured signals are more asymmetrical than the modelling results except for the 90° case. This is because the machined calibration cracks are slightly asymmetrical themselves. Consequently, the actual Bz magnetic field deviates from the centre of the crack, increasing the difference between the trough and the peak values meaning the actual Bz trough-peak ratios are slightly lower than the model results (this will be discussed in more detail in section 5.3). For the crack cluster 7, the experimental Bz peak-trough value is lower than the modelling result by 9.5 %. As the crack cluster 7 is machined on an unworn rail, with the cracks in the curved gauge side, the ACFM probe sensor does not conform fully to the rail surface (the flat base of the sensor is quite long, i.e. 12 mm and prevents true conformal contact), leading the trough and peak values to be more asymmetrical than the result with the flat steel plate.

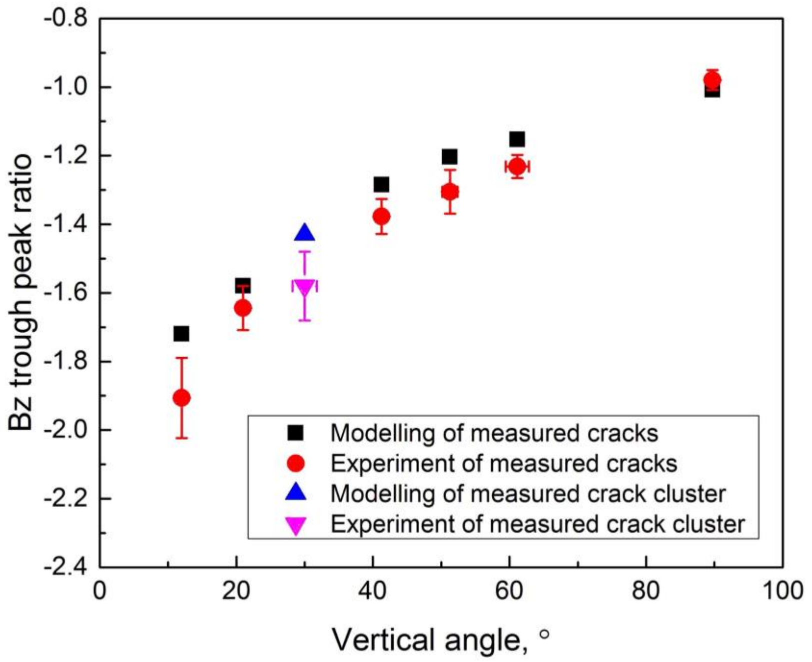

Figure 4.7 Model and experimental results of the Bz trough-peak ratios against different vertical angles for single and multiple cracks. The experimental results show standard errors for both measured vertical angles and the Bz trough-peak ratios.

4.4.2 Bz trough-peak ratios for vertical angle measurement of semi-elliptical cracks

Cracks with surface lengths of 8 mm, 15 mm and 21 mm, which are categorized as “light”, “moderate” and “heavy”, respectively, by Network Rail (see Figure 2.7) have been modelled to investigate the influences of crack dimensions on the relationship between Bz trough-peak ratios and the crack vertical angles. Each crack has been studied with the maximum and minimum elliptical ratios reported for RCF cracks of 1 and 1.75.

The Bz trough-peak ratio is a reflection of the asymmetrical distribution of the Bz magnetic field caused by the vertical angle, as discussed above. Cracks with the same surface length but different ellipse values show the same Bz trough-peak ratio when the vertical angle is between 30° to 90°, as shown in Figure 4.8. As the cracks become shallower, at vertical angles less than 30°, the Bz trough-peak ratios are no longer the same for the same surface length. The Bz trough-peak ratio values for the small elliptical ratio, i.e. the longer pocket length, are lower than for the higher elliptical ratio. The variations are caused by the different pocket lengths of the cracks, as cracks with a longer pocket length give a shorter distance from the negative area of the magnetic field to the measurement line, leading to the difference between the highest and lowest values along the measurement line becoming much greater. However, this effect becomes less obvious with an increase of surface length, as for the results for the 21 mm surface length cracks. The longer surface length causes a large shift in the Bz magnetic field along the surface length when compared to the displacement perpendicular to the surface length with changing vertical angle. Therefore, the distance from the measurement line to the Bz maximum and minimum value is greater, which decreases the difference caused by the variations of the pocket length between the highest and lowest values along the measurement line.

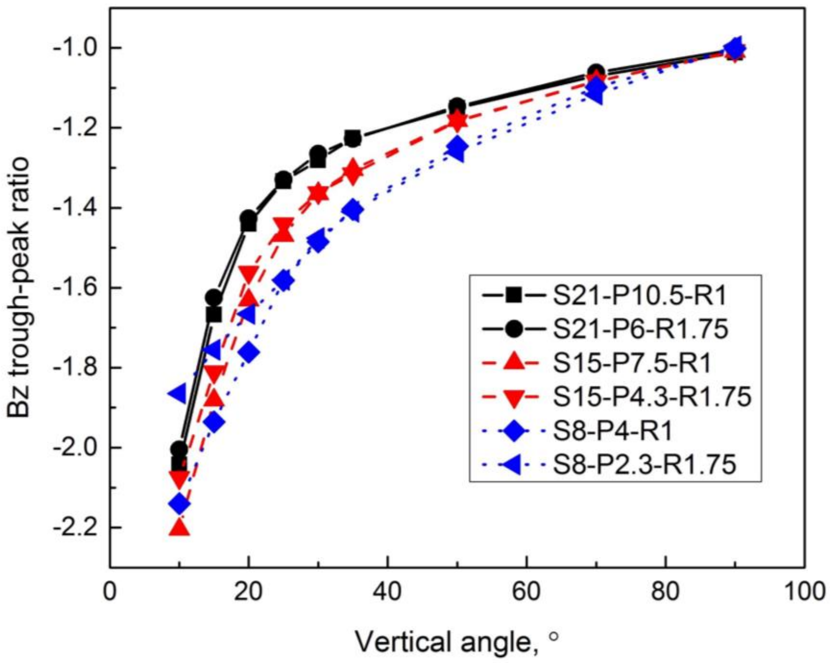

Figure 4.8 Bz trough-peak ratios against crack vertical angle along the 45° measurement line for semi-elliptical cracks from light to heavy category with elliptical ratios 1:1 and 1:1.75 (*S* denotes the surface length, *P* denotes the pocket length and *R* denotes the elliptical ratio).

4.4.3 Angle of measurement line to the crack surface-breaking component

The Bz trough-peak ratio along the 45° measurement line has been shown to record differences caused by variations in vertical angle, through modelling and experimental validation in section 4.4.1. However from the contour plot of the Bz magnetic field (Figure 4.5), it would be expected that the Bz trough-peak ratio is rather sensitive to the angle of the measurement line, i.e. the angle at which the sensor is scanned across the crack opening component. To investigate the sensitivity, the ACFM sensor was moved by hand at 0 mm lift-off through the centre of the crack surface-breaking component at different measurement angles with the sensor orientated such that current flows perpendicular to the crack surface-breaking component. The measurement angle in the model was varied between 0° to 85° with respect to the crack surface length and experimental measurements were carried out at angles of 15°, 25°, 45°, 75° to compare with the modelling results.

Figure 4.9 shows the Bz trough-peak ratios against measurement angle for cracks with surface lengths of 8 and 15 mm (elliptical ratio of 1.25). For the crack at an angle of 90°, the distances from the measurement line to the negative and positive valued areas of Bz at any measurement angle are similar, therefore the Bz trough-peak ratio values remain at -1. As the measurement angle increases, the negative and positive valued areas of the Bz magnetic field move away from the measurement line. The distance to the positive valued area is greater than to the negative valued area, leading to the difference between the minimum and maximum values along the measurement line becoming larger. This explains why the Bz trough-peak ratios decrease with an increase in the measurement angle, as shown in Figure 4.9.

Experimental results, with error bars, for the calibration cracks with vertical angles of 21° and 12° (cracks 5 and 6, respectively) are also shown in Figure 4.9a. The figure indicates that it is difficult to distinguish the crack vertical angle using the Bz trough-peak ratio for measurement lines at low angles with respect to the crack surface-breaking component. The Bz trough-peak ratio starts to saturate at larger measurement angle, e.g. 75° and 65° for the crack with surface lengths of 8 and 15 mm, respectively. Results at greater measurement angles will make it easier to distinguish the crack vertical angle in the model results, however in experimental inspection with the ACFM sensor, the Bz trough-peak ratio measured via a measurement line at greater angles is more influenced by noise, as the magnitude of the maximum and minimum values along the measurement line are rather small. An optimization study to determine the best measurement line angle for the Bz trough-peak ratio could be carried out with regard to different crack surface lengths, however, in this study 45° was selected as giving a sufficiently large signal-to-noise ratio and Bz trough-peak ratio to allow the crack vertical angle to be determined.

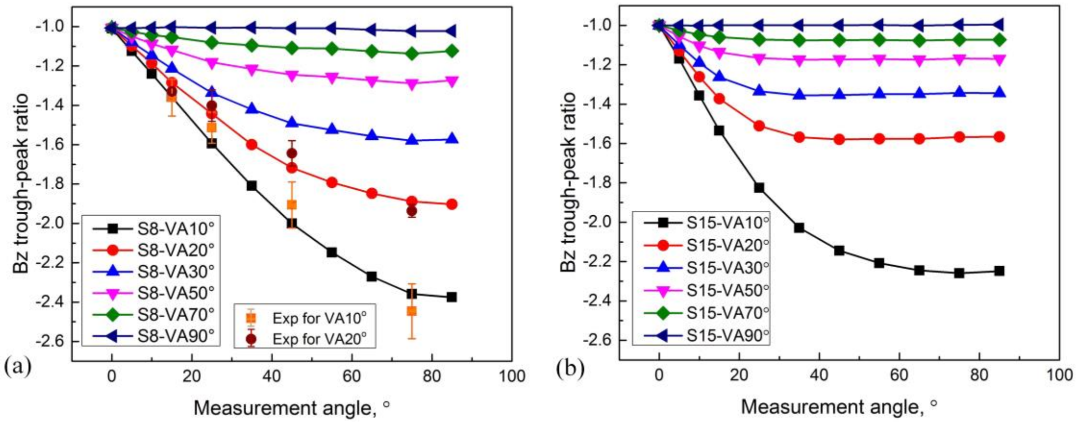

Figure 4.9 Bz trough-peak ratio against the measurement angle ranging from 0° to 85° for cracks with surface length of (a) 8 and (b) 15 mm (with elliptical ratio of 1.25); experimental results for calibration cracks with surface length of 8 mm and vertical angle of 10° and 20° are also shown (*S* denotes the surface length and *VA* denotes the vertical angle).

4.4.4 Sensor lift-off

The ACFM technique is less sensitive to changes in lift-off than eddy current testing, as the signal strength diminishes proportional to the square of the lift-off, rather than the cube, which is the case for the eddy current technique. This facilitates the use of ACFM even through coatings, paint or contamination. However, the accurate quantification of the crack vertical angle using ACFM Bz signals may be adversely affected by variations in lift-off due to the signal magnitude changing. Therefore the influence of lift-off needs to be determined so that correct estimation of the crack vertical angle can be achieved.

For a lift-off sensitivity experiment, the ACFM pencil sensor was held at a certain lift-off and moved by hand through the centre of the crack opening component at a measurement angle of 45°. A constant lift-off was achieved using cardboard spacers with different thicknesses, i.e. 1, 2, 3, 4, and 5 mm, as cardboard has no effect on the ACFM signal.

Figure 4.10 shows the results of the Bz trough-peak ratio against sensor lift-off for a crack with surface length of 8 mm and pocket length of 3.2 mm. The experimental results, shown with error bars, are for cracks with vertical angles of 10° and 20°. The experimental results match well with the model results. It is shown in Figure 4.10 that the sensor lift-off has only a small influence on the Bz trough-peak ratio for cracks with vertical angles from 90° to 50°; for example, the Bz trough-peak ratio for the case of vertical angle of 50° changes from -1.24 at 0 mm lift-off to -1.14 at 5 mm lift-off, a difference of 8.06 %. This difference will cause an over estimation of less than 10° for the vertical angle according to the model results at 0 mm lift-off shown in Figure 4.7. However, the impact of sensor lift-off on the Bz trough-peak ratio becomes larger when the crack vertical angle changes from 30° to 10°. A maximum difference of 30.5% is observed for the 10° vertical angle crack when the lift-off changes from 0 mm to 5 mm, which will cause an over estimation of 30° for the vertical angle.

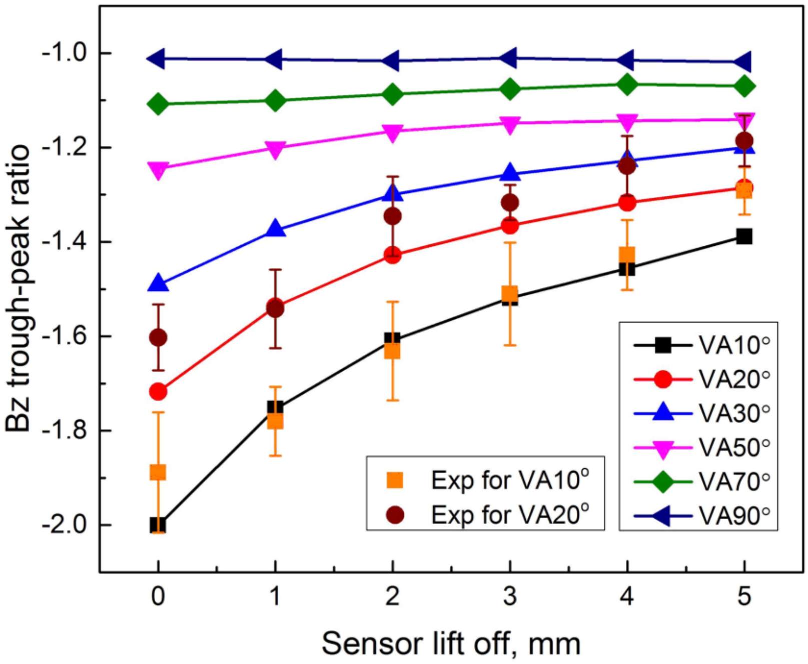

Figure 4.10 Bz trough-peak ratio against the sensor lift-off for a crack with surface length of 8 mm and pocket length of 3.2 mm; experimental results with error bars for the same calibration crack with vertical angle of 10° and 20° are also shown (*VA* denotes the vertical angle).

4.4.5 Bz trough-peak ratio for clusters of uniformly sized cracks

Real RCF cracks are usually variable in size and are present in the form of clusters, for example, it has been observed within a cluster of RCF cracks in a rail taken from service that the maximum difference in the surface length can be 9 mm and that for the pocket depth it can be as large as 5.2 mm [21]. Modelling work has been carried out for uniformly sized crack clusters to investigate how Bz trough-peak ratios respond to the variations in surface length and spacing between adjacent cracks. This is a starting point after which further investigation into the relationship between Bz trough-peak ratios and crack clusters with non-uniform sized cracks will be discussed in chapter 6.

Figure 4.11a shows the distribution of the Bz magnetic field above the uniformly sized crack cluster with surface length of 15 mm and pocket length of 4.3 mm. Cracks are at a vertical angle of 30° and are uniformly spaced 8 mm apart. Figure 4.11b gives the Bz signals recorded along the measurement line at 45° (marked on Figure 4.11a) for the crack cluster with uniformly changed vertical angles. The 45° measurement line passes across the centre of each of the surface-breaking component of cracks. As vertical angle becomes shallower, the magnitude of the Bz trough-peak ratio is greater, as shown in Figure 4.8, which indicates the difference between the trough and peak values is greater at shallower vertical angles. This explains that multiple peaks and troughs are observed in signals for shallow vertical angles while signals become flat at large vertical angles.

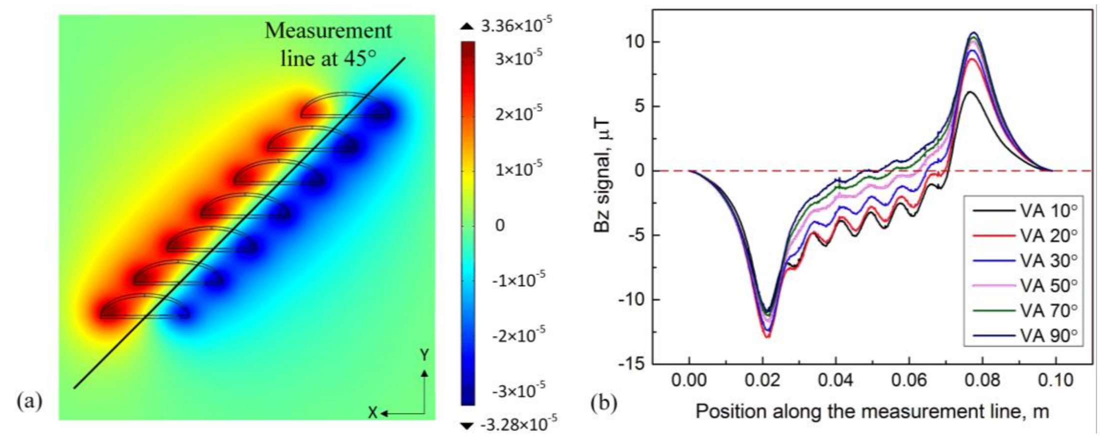

Figure 4.11 (a) Plan view of contour plots of the Bz magnetic field above the uniformly sized crack cluster with vertical angle of 30°; (b) Bz signals along the

measurement line at 45° marked on (a) for the uniformly size crack cluster with different vertical angles. Cracks are with surface length of 15 mm and pocket length of 4.3 mm; inner spacing between adjacent cracks is 8 mm.

The first trough and the last peak along the 45° measurement line can be used to determine the Bz trough-peak ratio for crack clusters to indicate variations in vertical angles. It is inevitable that the peak and trough values will be influenced by that of adjacent cracks. The influence depends on the size of the cracks and the spacing between them. Figure 4.12a shows the Bz trough-peak ratio for uniformly sized clusters with surface lengths of 8 mm, 15 mm and 21 mm. The inner spacing is 8 mm and the elliptical ratios are 1 and 1.75. It can be seen in Figure 4.12a that the Bz trough-peak ratio shows a similar trend for crack clusters to that for the single crack with different surface length (as shown in Figure 4.8), but the magnitude of the Bz trough-peak ratio is smaller than that for the single crack, as the minimum and maximum values of the Bz signal are influenced by the adjacent troughs and peaks. Figure 4.12b shows the influence of inner spacing, i.e. 4, 6, 8, 10 mm, on the Bz trough-peak ratio for a uniformly sized cluster with surface length of 15 mm (elliptical ratio 1.75). When the inner spacing between cracks is greater, the influence of adjacent cracks on the Bz trough-peak ratio for the crack cluster decreases and the Bz trough-peak ratio for the case with inner spacing of 10 mm is the closest of those investigated for the same sized single crack (shown by the inverted triangle in Figure 4.8).

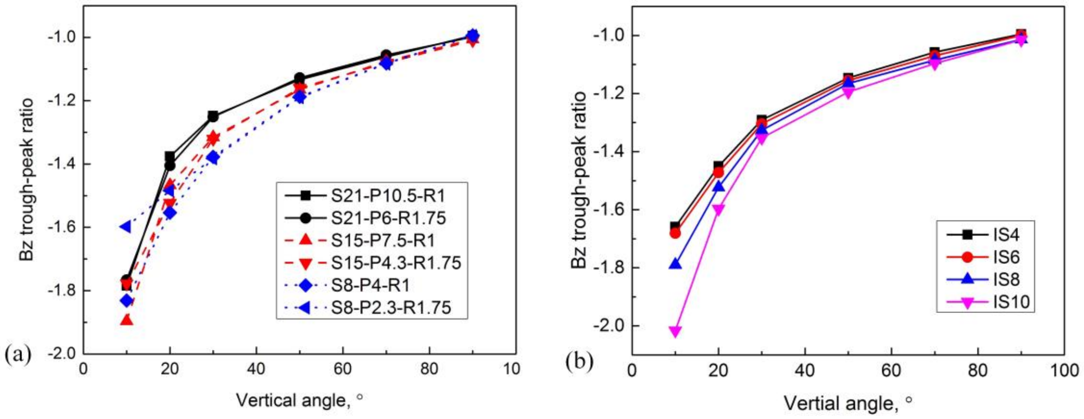

Figure 4.12 Bz trough-peak ratio for uniformly sized clusters when (a) the surface length for the crack cluster changes (b) the inner spacing between each crack

changes (*S* denotes the surface length, *P* denotes the pocket length, *R* denotes the elliptical ratios and *IS* denotes the inner spacing).

Therefor the use of the relationship between the Bz trough-peak ratio and the single crack vertical angle will lead to an overestimation of the vertical angle for cracks of the same uniform size within clusters and therefore, a different relation between the Bz trough-peak ratio with the surface length and the inner spacing should be considered with regard to the determination of vertical angle for uniformly sized crack clusters (see discussion in section 5.2)

4.5 Summary

This chapter presented the relationship between the ACFM Bx and Bz signals and the vertical angle for RCF cracks using model predictions and experimental measurements. The Bz trough-peak ratio is proposed to determine the vertical angle of single and multiple RCF cracks. The main conclusions are as follows

- The Bx signal is insensitive to crack vertical angle in the range 30°-90°. However, when the vertical angle is less than 30°, the Bx signal increases because the Bx trough moves further away from the centre of the crack opening, therefore the minimum Bx value recorded for a single line scan is not the actual minimum value of the Bx magnetic field.

- The effect of crack vertical angle on the Bx signal, and hence pocket length measurement, for cracks with vertical angles less than 30° has been determined; errors of 50 % in crack pocket length value (under estimate) result for a crack of 3.2 mm pocket length and a 10° vertical angle of propagation if basing the pocket length estimate on sizing methods applicable to vertical cracks.

- A Bz trough-peak ratio, for measurement through the crack centre along a line at 45° to the crack surface length, has been defined to indicate the asymmetrical distribution of the Bz magnetic field. It has been shown that the Bz trough-peak ratio varies with the crack vertical angle, with this variation also being influenced by crack surface length. The results show that the crack vertical angle can be determined from the measured Bz trough-peak ratio, provided the crack surface length is known.

- The angle of the measurement line has a significant influence on the Bz trough-peak ratio. It is difficult to distinguish the crack vertical angle using the Bz trough-peak value when the measurement angle is less than 20°; the Bz trough-peak ratio starts to saturate at larger measurement angles, e.g. 75° and 65° for a crack with surface length of 8 and 15 mm, respectively.

- The Bz trough-peak ratio is insensitive to the sensor lift-off for cracks with vertical angles between 90° to 50°. However, the influence of lift-off becomes larger when the crack vertical angle is between 30° to 10°. A maximum difference in signal of 30.5% in value is observed for the 10° vertical angle crack when lift-off changes from 0 mm to 5 mm, which will cause an over estimation of 30° in the vertical angle.

- The Bz trough-peak ratio along the measurement line at an angle of 45° to the crack surface-breaking component can be used to detect the vertical angle for uniformly sized crack clusters, but it is different to that for the same sized single cracks, as the signal is influenced by adjacent cracks. Change of surface length and the inner spacing of cracks in the cluster will also influence the relationship between the Bz trough-peak ratio and the crack vertical angle.

5. Sizing RCF cracks using ACFM signals

5.1 Bx responses to single RCF cracks

The trough value of the Bx signal obtained from the measurement line for a single RCF crack is affected by the variation in the crack vertical angle, as discussed in section 4.2 (see Figures 4.1 and 4.2). This may cause the pocket length determination from the Bx signal for a single RCF crack to be inaccurate if the crack vertical angle is not known. Figure 5.1 shows the $\Delta Bx_{max}/Bx_0$ value recorded along measurement lines that are parallel (0°) with and at 45° to the crack surface-breaking component for three single RCF cracks (surface length of 8, 15 and 21 mm, respectively with the same elliptical ratio) with different vertical angles. These values can be compared with the minimum values of the x-component of the magnetic field (i.e. the minimum value in the blue valued area of the contour plot shown in Figure 3.2a) which are also shown in this figure.

Figure 5.1 shows that the $\Delta Bx_{max}/Bx_0$ value obtained from the 0° measurement line (used for pocket length determination) significantly decreases, by 62.4 %, as the vertical angle changes from 30° to 10° for the crack with 8 mm surface length, whereas there is only a 15.8 % decrease in $\Delta Bx_{max}/Bx_0$ as the vertical angle changes between 90° to 30°. For larger cracks with surface length of 15 and 21 mm, the $\Delta Bx_{max}/Bx_0$ value also drops more significantly when the vertical angle changes from 30° to 10° compared to that for 90° to 30°. The decrease in the vertical angle means the difference between the minimum value of the x-component of the magnetic field and the minimum value recorded along the measurement line is greater due to the negative valued area of the x-component of the magnetic field moving further from the crack surface position, as discussed in section 4.2. Figure 5.1 also shows that this deviation is more significant when it comes to larger cracks, e.g. the deviation between the minimum value of the Bx magnetic field and the value recorded along the 0° measurement line is 9.0 % for the crack with 21 mm surface length at a vertical angle of 10°, but is only 2.4 % for the crack with 8 mm surface length. The minimum Bx value from the Bx magnetic field is lower than that obtained from the measurement line (therefore the $\Delta Bx_{max}/Bx_0$ value is higher, as shown in Figure 5.1) because it eliminates the effect of the shift in the minimum current intensity position (negative valued area) of Bx and only the decrease in the current density is considered (see discussion in section 4.3.1).

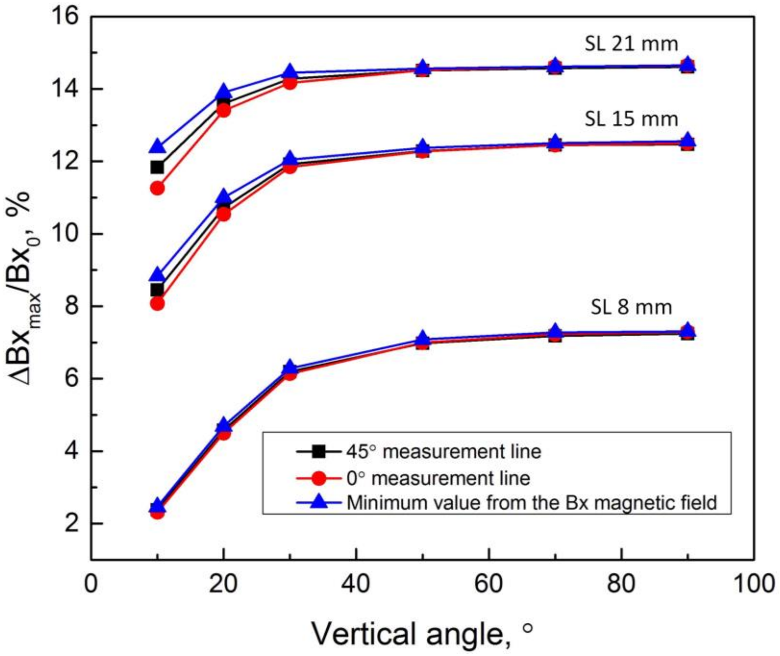

Figure 5.1 Normalised maximum ΔBx obtained from the 45°, 0° measurement lines and the contour plot of the Bx magnetic field for single RCF cracks with surface length of 8, 15 and 21 mm (elliptical ratio of 1.75) and varying vertical angle.

To predict the pocket length of single cracks using the Bx signal obtained from 0° and 45° measurement lines, the crack vertical angle should be determined first as cracks with vertical angles of 30°-10° will cause significant errors based on the results shown in Figure. 5.1. The deviation of the $\Delta Bx_{max}/Bx_0$ value caused by shallow vertical angles depends on the surface length and pocket length and should be compensated when sizing the pocket length using the signal obtained from a single ACFM measurement line (i.e. the 0° or 45° measurement line).

In the case of multiple cracks, the change in the $\Delta Bx_{max}/Bx_0$ value caused by the variation of crack vertical angle depends not only on crack surface length but the crack arrangement in the cluster, e.g. crack inner spacing and crack number. Therefore, for accurately sizing of the pocket length of angled multiple cracks, the influences of the crack angle, the crack surface length, the crack inner spacing and the crack number on the Bx signals need to be investigated and compensations should be considered when using the sizing algorithm developed for cracks with different vertical angles. This is discussed in section 5.2.

5.2 Bx responses to uniformly sized crack clusters

RCF cracks often appear in the form of clusters with cracks that are closely spaced, leading to an interaction between ACFM signals from each crack. Sizing for crack clusters using an algorithm based on predictions for single cracks inevitably leads errors, as shown in [21]. The crack vertical angle also influences the pocket length prediction using Bx signals obtained from either the single ACFM measurement or the minimum values of the x-component of the magnetic field. In this section, modelling work on the ACFM responses to uniformly sized RCF crack clusters, considering variations in crack surface length, crack spacing, crack number and crack vertical angle is presented, which provides a starting point for the study of sizing non-uniform crack clusters using ACFM (discussed in chapter 6). This is an extension study for sizing multiple RCF cracks following initial ACFM modelling on multiple cracks carried out for a limited number of crack arrangement conditions in [21]. In the previous study variations in crack vertical angle were not considered.

The initial uniformly sized crack cluster considered in this work consists of 4 cracks with surface length of 12 mm and inner spacing of 4 mm. These values are close to the averages for the crack clusters taken from service (crack clusters 17 and 18 shown in Table 3.4); crack clusters with inner spacing of 4 mm and crack number of 4 were also considered in previous studies [20, 21]. Two vertical angles (10° and 90°) were selected for the modelling work, as RCF cracks with vertical angle at 10°-30° have been reported [3, 18, 19] and a model of cracks with 90° vertical angle can give representative values for cracks with vertical angles between 30° and 90° (as discussed in section 4.2.1); 10° was selected to determine the maximum expected error if vertical angle is not considered in the prediction of the crack pocket length using the Bx signal. The signals are extracted from a measurement line across the centre of every crack in the cluster at an angle of 45° to the surface-breaking component.

5.2.1 Variation of crack surface length

The cracks modelled are semi elliptical in shape with ratios (half surface length/pocket length) from 1 to 1.75 and surface lengths from 3 to 40 mm in order to cover the whole range of RCF cracks included in the UK classification system [70]. Figure 5.2 shows the modelling results for normalised ΔBx_{max} with the variation in surface length when the vertical angle for the cracks in the cluster is 90° and 10° and results for single RCF cracks (with vertical angle of 90°) from [20] are also compared in Figure 5.2a.

The normalised maximum ΔBx value for the cluster increases steeply as the surface length increases from 3 mm but begins to saturate when the surface length is 27 mm, whilst for single cracks the maximum ΔBx value begins to saturate at a smaller crack size, less than approximately 20 mm surface length. This means for uniformly sized cracks in the clusters presented in this study, the ACFM Bx signal can be effectively differentiated for cracks from the light to the heavy category based on the modelling results in Figure 5.2a (assuming an elliptical shape). As shown in Figure 5.2b, cracks with a vertical angle of 10° decrease the maximum ΔBx with an average difference of 30.1 % for all elliptical ratios and surface lengths when compared with that for 90° cracks due to the reduced current density and the shift in the minimum value of the Bx magnetic field for shallower angles.

The difference in the normalised maximum ΔBx caused by the vertical angle of 90° and 10° are listed and compared in Table 5.1 for each crack surface length of the crack cluster (elliptical ratio of 1). The maximum ΔBx are obtained from the 45° measurement line across the centre of the surface-breaking component of the crack cluster and the minimum value of the Bx magnetic field, respectively. The deviation in the normalised maximum ΔBx decreases with the larger crack surface length and begins to saturate at a surface length of 33 mm. For accurate sizing of pocket lengths of crack clusters, the maximum ΔBx should be compensated, for example as shown in Table 5.1, a maximum compensation of 7.8 should be considered when predicting the pocket length from the 45° measurement line for the crack cluster with a surface length of 15 mm (elliptical ratio of 1). It is shown that for all crack lengths (for 45º measurement line) the compensation is about 7.8 except the smallest cracks (surface length of 3 mm). This makes the prediction of the compensation easier because it is not necessary to calculate all surface lengths cases.

For cracks with a vertical angle of 90°, the minimum value of the Bx magnetic field (the negative valued area in the contour plot) is above the centre of the crack surface-breaking component so the maximum ΔBx obtained from these two methods (i.e. from the 45° measurement line and from the minimum value of the Bx magnetic field) are similar, however when cracks become shallower (vertical angle of 10°), the minimum Bx value recorded along the 45° measurement line (across the centre of the surface-breaking component) is not the minimum value of the negative valued area, as the negative valued area shifts away from the centre of the crack surface component. Therefore, the maximum ΔBx diverges at a vertical angle of 10° for these two measurements, with the maximum ΔBx from the minimum value of the magnetic field being larger than that from the 45° measurement

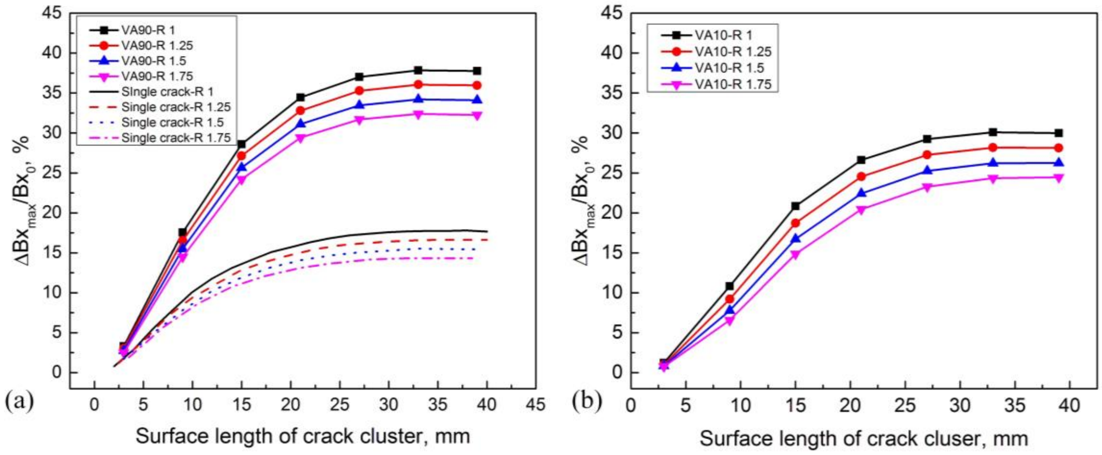

Figure 5.2 Modelling results for Bx signal response to variations of surface length when the crack vertical angle is (a) 90° and (b) 10°; the calibration curves for single cracks with semi ellipse shape from the literature [20] are also shown in (a); *VA* denotes the vertical angle and *R* denotes the elliptical ratio (uniformly sized crack clusters with inner spacing of 4 mm).

Table 5.1 Normalised maximum ΔBx obtained from the 45° measurement line and the minimum value of the magnetic field for crack clusters with vertical angle of 90° and 10° when the crack surface length varies (*SL* denotes surface length; *VA* denotes vertical angle; elliptical ratio 1).

SL, mm	3		9		15		21		27		33		39	
VA, °	90	10	90	10	90	10	90	10	90	10	90	10	90	10
ΔBx_{max} (45° measurement line), %	3.3	1.2	17.5	10.8	28.6	20.8	34.5	26.6	37.0	29.2	37.8	30.0	37.8	30.1
Deviation, %	63.6		38.3		27.3		22.9		21.1		20.6		20.4	
ΔBx_{max} (minimum value in the magnetic field), %	3.3	1.3	17.6	11.5	28.7	21.9	34.5	28.0	37.1	30.7	37.8	31.8	37.9	31.9
Deviation, %	60.1		34.7		23.7		18.8		17.3		15.9		15.8	

5.2.2 Variation of crack inner spacing

The inner spacing (distance between adjacent cracks in a cluster) of RCF crack clusters has been reported to vary from 0.8 mm to 20 mm [1, 21], for different rail grades, rail radius of curvature and traffic types. Closely spaced cracks result in interactions between the ACFM signals for each crack. It has been reported that individual troughs for each crack in a cluster are not seen if the inner spacing is less than 5 mm and the $\Delta Bx_{max}/Bx_0$ value for closely spaced (1 mm) cracks is significantly greater (52.4 %) than for an single crack of the same size; these results were from modelling the ACFM signal response for a cluster of uniform sized (surface length 10 mm) cracks with a lift off of 0 mm [20, 21]. The study [151] developed a neural network to predict the pocket length of crack clusters based on ACFM signals; a large number of simulations were carried out to investigate the effect of crack inner spacing on the Bx signal responses. However, only cracks with vertical angles of 25° and 30° have been considered using the IB condition in these studies (see section 4.2.1 for a discussion on the significance of the boundary conditions used for modelling shallow angle cracks). The results for crack vertical angles of 30-90° will be the same and the 25° result is expected to be similar to that for the 30° result as the difference in angle is small. Therefore the influence of changing vertical angle to include shallow angles (< 30°) on the Bx responses to multiple cracks has not yet been ascertained, and should be considered to determine the compensation required when sizing the pocket length for shallow angled multiple RCF cracks.

A uniformly sized crack cluster (4 cracks with surface length 12 mm) with crack inner spacing from 2 to 20 mm and crack vertical angles of 90º and 10 º has been investigated. In Figure 5.3 it can be seen that the $\Delta Bx_{max}/Bx_0$ value decreases as the crack inner spacing increases but it begins to saturate at a spacing of 12 mm for both vertical angle cases; in addition the shallower vertical crack angle (10°) decreases the $\Delta Bx_{max}/Bx_0$ value when compared with the results for vertical angle of 90°. As shown in Figure 5.3 for the crack cluster with surface length of 12 mm when the ratio of surface length to inner spacing is smaller than a value of 1, the Bx signals remain at the same levels for increasing crack spacing for all elliptical ratios (with the value being determined by the elliptical ratio). Clustered cracks spaced at this distance can be considered as behaving like single cracks as far as ACFM inspection is concerned because the cracks are spaced far enough apart that the adjacent crack has no influence on the Bx signal. When the surface length to inner spacing ratio is larger than 1, the $\Delta Bx_{max}/Bx_0$ value is significantly increased due to the smaller inner spacing. Modelling results show that the $\Delta Bx_{max}/Bx_0$ values remain constant when the ratio of surface length to inner spacing ≤ 1 for other surface lengths (e.g. 6 mm, 15 mm and 20 mm) investigated in this study. It is believed that the ratio of surface length to inner spacing dominates the influence of inner spacing on the $\Delta Bx_{max}/Bx_0$ value for a crack cluster and it can be used to indicate whether the inner spacing is great enough to eliminate the influence of the adjacent crack on the Bx signal.

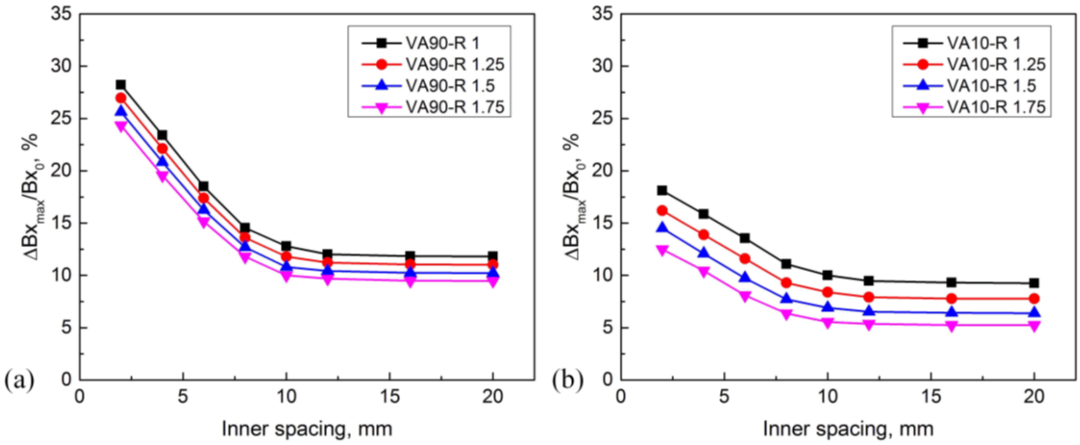

Figure 5.3 Modelling of Bx signals response to the variations of inner spacing for uniformly sized crack clusters with surface length of 12 mm when the vertical angle is (a) 90° and (b) 10°; *VA* denotes the vertical angle and *R* denotes the elliptical ratio.

Table 5.2 lists the normalised maximum ΔBx obtained from the 45° measurement line and the minimum value of the magnetic field for crack clusters (elliptical ratio of 1) with vertical angle of 90° and 10° when the crack inner spacing varies from 2 to 20 mm. The difference between 10º and 90º cracks should be considered when using the ACFM signal to characterise the pocket length of the crack cluster. It should be noted that there is little difference in the effect for the different measurements (i.e. along the 45° measurement line compared to the minimum value in the Bx magnetic field) as the crack size (surface length and pocket length) remains the same, which gives a relatively fixed distance from the 45° measurement line to the minimum value of the Bx magnetic field. However, the difference is expected to change if the crack size changes, then the difference should be calculated to obtain the compensation with regard to the new surface length.

Table 5.2 Normalised maximum ΔBx obtained from the 45° measurement line and the minimum value of the magnetic field for crack cluster with vertical angle of 90° and 10° when the crack inner spacing varies (*IS* denotes inner spacing; *VA* denotes vertical angle; elliptical ratio 1).

IS, mm	2		4		6		8		12		16		20	
VA, °	90	10	90	10	90	10	90	10	90	10	90	10	90	10
ΔBx_{max} (45° measurement line), %	28.2	18.1	23.4	15.9	18.5	13.5	14.5	11.1	12.1	9.5	11.8	9.3	11.8	9.3
Deviation, %	35.8		32.0		27.0		23.4		21.5		21.2		21.2	
ΔBx_{max} (minimum value in the magnetic field), %	28.3	18.9	23.5	16.7	18.6	14.2	14.7	11.5	12.2	9.7	11.9	9.6	11.9	9.6
Deviation, %	33.2		28.9		23.7		21.8		20.5		19.3		19.3	

5.2.3 Variation of crack number

The number of cracks presenting in the cluster can also vary and hence influence the Bx signal for crack pocket length prediction [21]. The previous study [21] showed the effect of crack number for crack clusters with an inner spacing of 1 mm; the ACFM neural network [151] developed for crack cluster pocket length prediction was based on a large number of simulations focusing on crack numbers up to 17 with the crack inner spacing from 1 to 12 mm. However the crack vertical angle also has an influence on the change caused by the crack number and should be considered. The effect of changing the number of cracks within a uniformly sized cluster with 4 mm spacing for vertical angles of 90° and 10° have been modelled and the results are shown in Figure 5.4. The cracks in the cluster have a surface length of 12 mm and inner spacing between each crack is 4 mm (surface length to spacing ratio of 3).

The $\Delta Bx_{max}/Bx$ value increases when the crack number increases up to 6 then the value begins to saturate for all elliptical ratios studied. The $\Delta Bx_{max}/Bx$ value for the cluster with the shallow vertical angle (10°) is significantly lower than that for the 90° vertical angle, as the negative area of the magnetic field is smaller and it shifts from the crack surface-breaking component; the Bx signal recorded along the measurement line across the centre of the crack is not the minimum value of the magnetic field. Further increases in the number of cracks in the cluster have no obvious effect on the magnitude of the Bx signal along the measurement line.

Figure 5.5 shows the effect of crack number variation within a uniformly sized cluster with surface length of 15 mm and 3 mm spacing (surface length to spacing ratio of 5) for vertical angles of 90° and 10°. Cracks with different elliptical ratios have the similar tendency in the $\Delta Bx_{max}/Bx$ value changing with crack number that the $\Delta Bx_{max}/Bx$ value increases rapidly as the crack number increases and begins to saturate at a certain crack number, e.g. the $\Delta Bx_{max}/Bx$ value in Figure 5.5 saturates at a crack number of 9 for crack clusters with vertical angles of 90° and 10°.

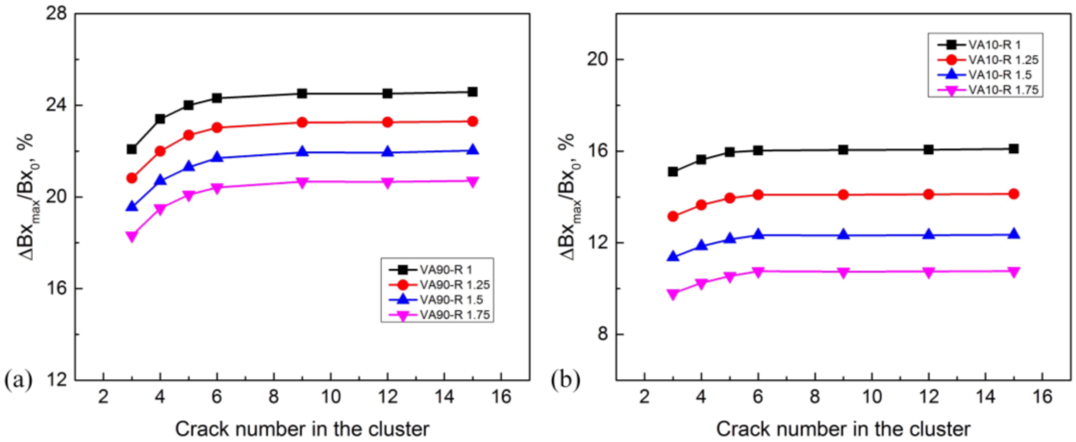

Figure 5.4 Modelling of Bx signals response to the variations of crack number for a uniformly sized crack cluster with surface length of 12 mm and inner spacing of 4

mm when vertical angle is (a) 90° and (b) 10°; *VA* denotes the vertical angle and *R* denotes the elliptical ratio.

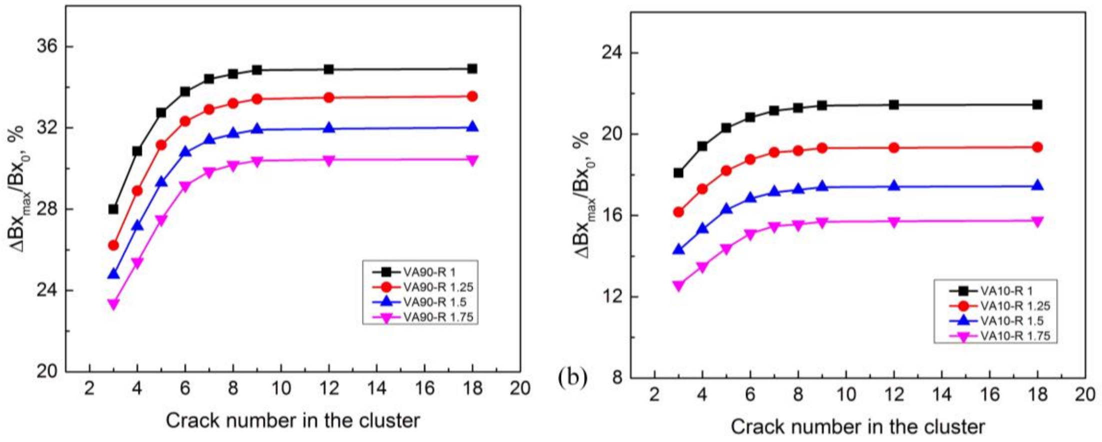

Figure 5.5 Modelling of Bx signals response to the variations of crack number for a uniformly sized crack cluster with surface length of 15 mm and inner spacing of 3 mm when vertical angle is (a) 90° and (b) 10°; *VA* denotes the vertical angle and *R* denotes the elliptical ratio.

Figure 5.6 shows the $\Delta Bx_{max}/Bx$ value for crack clusters with 15 mm surface length but with different inner spacing (3-6 mm), which gives surface length to spacing ratios from 5 to 2.5. It can be seen that the influence of the crack number on the Bx signal depends on the ratio between crack surface length and crack inner spacing within a cluster; the $\Delta Bx_{max}/Bx$ value saturates at a larger value of crack number when the ratio of the crack surface length to the crack inner spacing increases, e.g. in Figure 5.6, the $\Delta Bx_{max}/Bx$ value saturates at crack number of 9 for the cluster with surface length of 15 mm and inner spacing of 3 mm (surface length to spacing ratio of 5) while the $\Delta Bx_{max}/Bx$ value saturates at crack number 4 or 5 for the cluster with surface length of 15 mm and inner spacing of 6 mm (surface length to spacing ratio of 2.5).

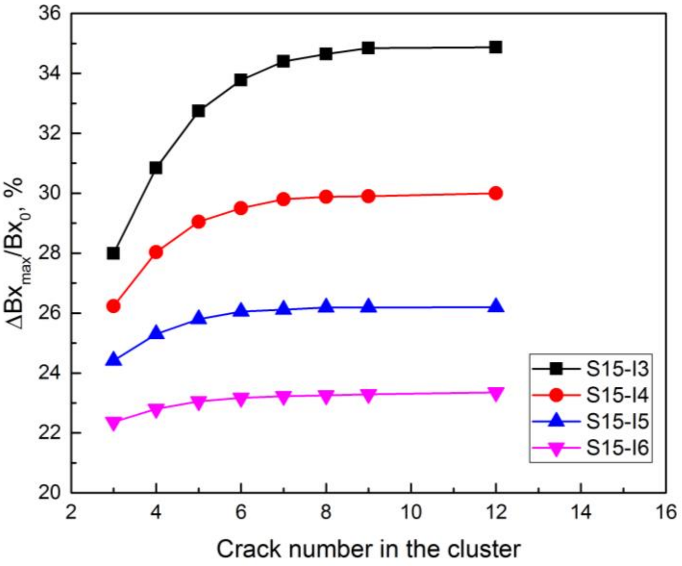

Figure 5.6 Modelling of Bx signals response to the variations of crack number for uniformly sized crack cluster with surface length of 15 mm and inner spacings of 3-6 mm (i.e. surface length to spacing ratio of 5 to 2.5) when vertical angle is 90° and elliptical ratio is 1; *S* denotes the surface length and *I* denotes the inner spacing.

5.2.4 Pocket length prediction for calibration crack clusters

Calibration crack clusters (crack clusters 8-13 in Figure 3.4) were used to verify the modelling results for the Bx responses to uniformly sized crack clusters with variations in crack surface length, crack inner spacing and crack number (as discussed in section 5.2.1-5.2.3). Crack clusters 8 to 13 have surface lengths from 5-21 mm, pocket lengths 2-7 mm (elliptical ratio 1-1.75), inner spacings of 2-7 mm and crack numbers 3-7, which represent the typical arrangements of RCF crack clusters found in the railway network.

Table 5.3 lists the $\Delta Bx_{max}/Bx$ values measured using the ACFM pencil sensor for each of the crack clusters, together with the predicted pocket length for crack clusters 8 to 13. The prediction was made using a lookup table based on the modelling results (similar with the results from the model used in this research) for uniformly sized crack clusters [151] where the measured $\Delta Bx_{max}/Bx$ value and the known surface length, inner spacing and crack number are the required inputs. The relative errors compared with the actual pocket lengths are also shown in the table. The results show that the predicted pocket lengths generally agree with the actual values with an average deviation of less than 10 %. The predicted pocket length is underestimated for all the crack clusters due to the machined cracks having a slightly asymmetrical shape (discussed in section 4.2.2). This causes the Bx trough along the measurement line, which is at 45 ° across the centre of the crack, to not be the minimum value in the x-component of the magnetic field.

These results are based on the ACFM measurements for calibration crack clusters with a vertical angle of 90° and the modelling results are for uniformly sized crack clusters with a vertical angle of 30° [151], however it has been shown that the Bx signal shows relatively small deviation (e.g. less than 6.2 % for the crack cluster with surface length of 15 mm) when the vertical angle changes from 90° to 30°. For crack clusters with vertical angle between 30° to 10°, the pocket length prediction should be modified because of the change in signal caused by the vertical angle, which depends on the crack surface length, the inner spacing and the crack number as shown in the previous sections. For example, for a multiple crack cluster, the crack vertical angle should be determined using the Bz trough-peak ratio proposed in the present study, then the amount of compensation for pocket length prediction can be determined according to the vertical angle range (90° to 30° or 30° to 10°) for different surface length, inner spacing and crack number arrangements. The details of how this can be carried out will be discussed in chapter 7 (Case study chapter).

Table 5.3 The results of pocket length prediction for calibration crack clusters based on the relationships between Bx signals and crack surface length, inner spacing and crack number for crack clusters with vertical angle of 90°.

Crack clusters	8	9	10	11	12	13
Measured $\Delta Bx_{max}/Bx$ values, %	6.1	9.4	17.6	24.1	20.8	22.4
Stand error of the measurement, %	0.4	0.7	0.4	0.4	0.5	0.7
Predicted pocket length, mm	1.8	1.8	4.1	4.7	5.5	6.5
Actual pocket length, mm	2.0	2.0	4.4	5.0	6.0	7.0
Relative error, %	10.0	10.0	6.8	6.0	8.3	7.1

5.3 Influence of crack shapes on ACFM signals

The shape of RCF cracks can generally be approximated by a semi ellipse with specific elliptical ratios (from 1 to 1.75) when they are in the light to moderate category (see Figure 2.7). However, RCF cracks can deviate from this regular shape and become non-planar with complex shapes, for example it has been observed that the subsurface portion of a RCF crack, whose surface length belongs to the moderate category, extends significantly beyond the surface-breaking component [3]. This may cause the vertical angle and pocket length prediction from a single ACFM scan to be inaccurate since the non-surface breaking component is not detected or the effect of asymmetrical shapes taken into account [20]. Therefore, it is important to investigate the influence of an asymmetrical shape on the crack vertical angle and pocket length predictions from a single ACFM scan.

Cracks in a rail sample taken from the service (shown in Figure 3.7) were progressive milled to investigate their crack profiles. Figure 5.7 shows the 3D profiles of RCF cracks using the data from progressive milling. The x and the y axes are orthogonal axes and the x axis represents the crack surface length. The z axis is the actual vertical depth of these cracks. The crack profiles were reconstructed based on the assumption that the crack surface length is linear. It can be seen that crack surfaces are non-planer (i.e. the vertical angle varies along the crack length); some portion of the crack sub-surface extension is not surface-breaking (as shown in Figure 5.7a, b and c, etc.) and can propagate into the rail significantly further than the surface breaking component, as shown in Figure 5.7f.

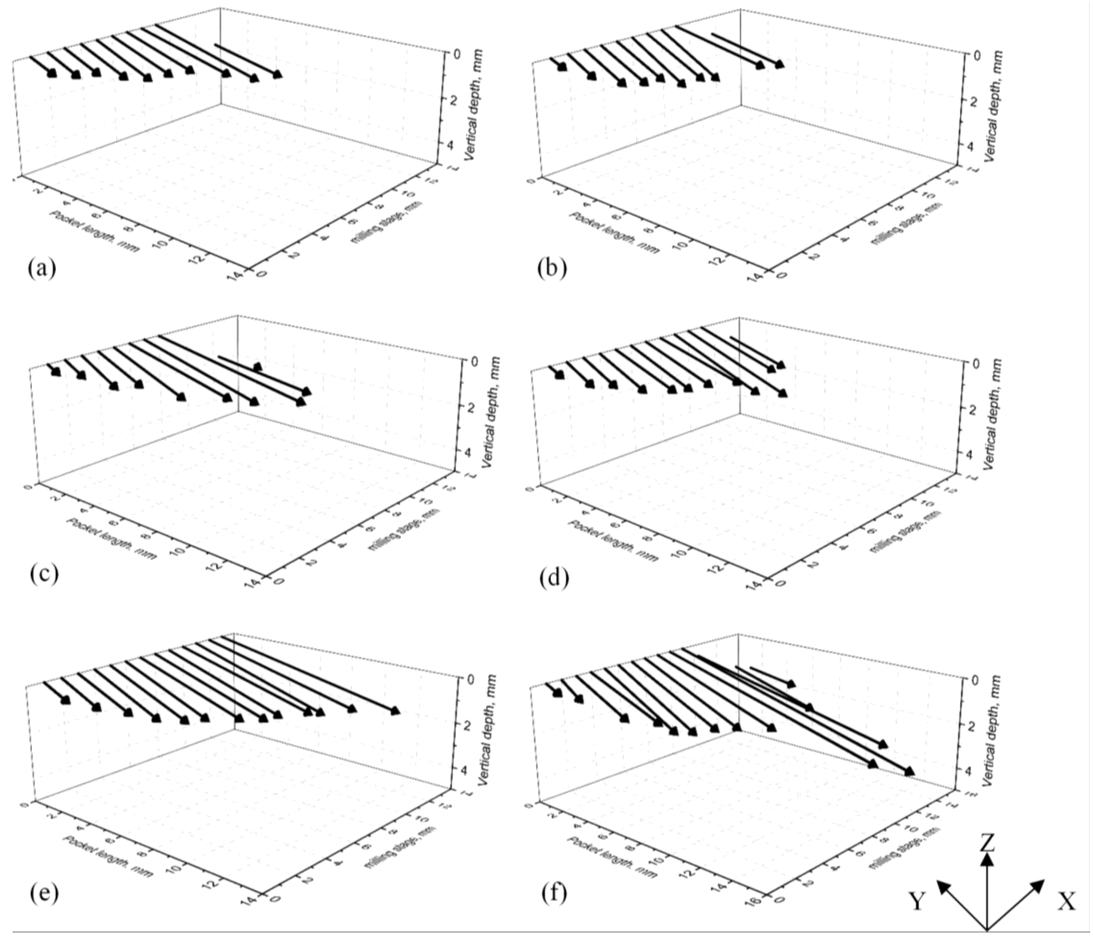

Figure 5.7 3D profiles of RCF cracks in the rail sample taken from service where x and y axes are orthogonal axes and the x axis represents the crack surface length; the z axis is the actual vertical depth of these cracks; the arrows represent the length and position of the RCF crack determined from the progressive milling stage.

Four crack profiles were imported into Comsol Multiphysics using interpolation and a modelling study on the influence of asymmetrical crack shapes on pocket length and vertical angle predictions for ACFM inspection was carried out. In the modelling work, all the crack profiles were modified to have the same surface length of 15 mm and maximum pocket length of 6 mm to allow the effect of crack shape only to be compared. The crack profiles were considered to be planar so that the influence of crack profile alone could be determined; actual RCF cracks are non-planar and the 2D profile is an idealised representation for modelling simplicity. Figure 5.8 shows the reconstructed crack profiles used in the model, denoted as A-D. Shape A is slightly asymmetrical but could be approximated as a semi ellipse. Shape D is also slightly asymmetrical and has a relatively flat bottom profile. Shape B indicates that there is a subsurface portion of the crack extending beyond the surface breaking component, as reported in the literature [3].

A perfect semi-elliptical crack with the same surface and pocket length dimensions was also modelled. The Bx signal was determined using a measurement line parallel with the crack surface-breaking component, as shown in Figure 3.2a. The Bz signal was determined from the measurement line across the centre of the surface-breaking component at an angle of 45° representative of the experimental inspection procedure using the ACFM probe sensor.

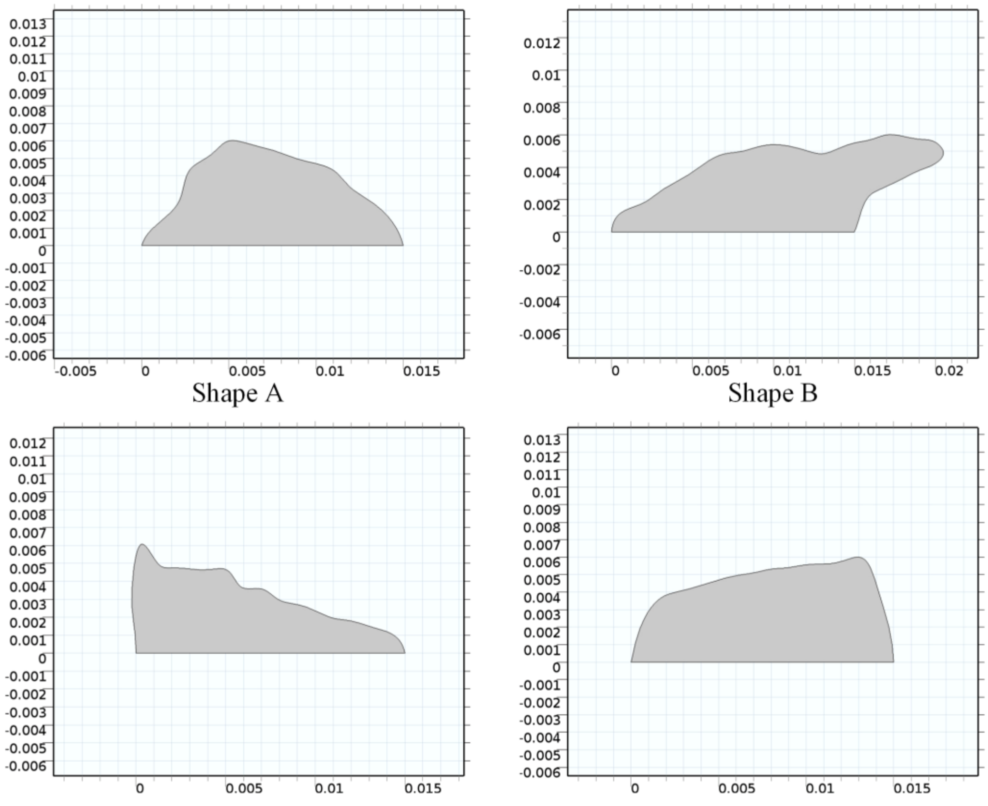

Shape A

Shape B

Shape C

Shape D

Figure 5.8 2D crack profiles developed from the measured dimensions from progressive milling.

Figure 5.9 shows the modelling results on how the $\Delta Bx_{max}/Bx$ value and the Bz trough-peak ratio responds to different crack profiles for vertical angles changing from 90° to 10°. The results for shape A are close to the $\Delta Bx_{max}/Bx$ value and Bz trough-peak ratio obtained from the perfect semi ellipse, indicating that this slight asymmetrical profile does not influence the determination of pocket length and vertical angle significantly. Shape D, with a slightly asymmetric shape and flat bottom also shows similar results except for the Bz trough-peak ratio when the vertical angle is 10°, where a difference of 10.1 % in value is seen compared to the semi ellipse shape. This gives an approximately 5º underestimate of vertical angle prediction (i.e. predicted vertical angle is less than 5º). Shape B and shape C are significantly asymmetrical, which causes an asymmetrical distribution of the x-and the z-component of the magnetic field with regard to the y axis. For the Bz trough-peak ratio, the maximum (peak) and minimum (trough) values along the single measurement line are asymmetrical. This can be seen by the small difference in Bz trough-peak ratio for the 90° (vertical) crack compared to the semi ellipse case, with this difference becoming magnified as the vertical angle decreases. The $\Delta Bx_{max}/Bx$ value of shape C for a vertical angle of 30º gives a value 23.4 % lower than that for the semi elliptical shape and therefore indicates an underestimation of pocket length of 3.3 mm; the Bz trough peak value of shape C for a vertical angle of 30 º gives a value 66.7 % lower than that for the semi elliptical shape, indicating a underestimate of vertical angle of more than 20º.

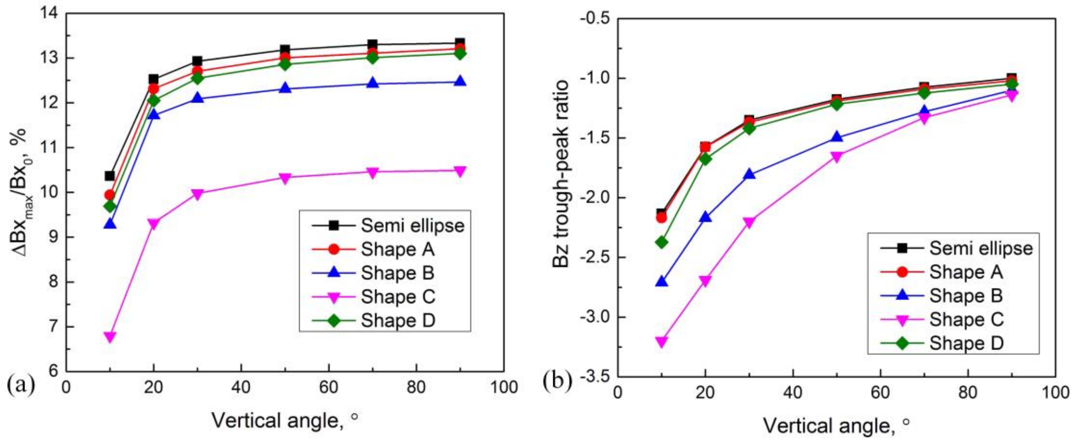

Figure 5.9 Influences of asymmetrical crack profiles on the (a) $\Delta Bx_{max}/Bx$ value and the Bz trough-peak ratio for cracks with shapes A-D.

The asymmetrical crack profile therefore results in an error in crack sizing when using the ACFM signals obtained through a single ACFM scan, e.g. the predicted vertical angle will be smaller than reality if using an assumed semi ellipse shape for the predictions; therefore the vertical depth of the crack will be also underestimated assuming the pocket length is known (from the Bx signal). The measured $\Delta Bx_{max}/Bx$

value and Bz trough-peak ratio can be compared with those for a crack with the semi-elliptical shape; this is a way to show that the crack profile is asymmetric and hence a different measurement (e.g. full grid scan) is needed (discussed in section 3.2.2).

The $\Delta Bx_{max}/Bx$ values and Bz trough-peak ratios in Figure 5.9 indicate that for accurate sizing of RCF cracks using a single ACFM scan the cracks should be regular, where the assumption of semi ellipse shapes is appropriate. Literature [3, 22] suggests that RCF cracks in the light category can be approximate as semi ellipses and most of RCF cracks in the moderate category also can be approximated as semi ellipses but it is in this category that the crack shapes start to become asymmetric. Figure 5.10 shows the normalised Bx signal recorded using the measurement line that is parallel to the crack surface-breaking component (as shown in Figure 3.2a). The results shows that the signals for shapes B and C are different with that for the semi ellipse due to the significantly asymmetrical crack shapes. It should be noticed that the Bx signal can be used to indicate the asymmetrical cracks shapes, i.e. the Bx trough shifts towards right and left for the shapes B and C because the crack shape extends to the right and left mostly for cracks B and C respectively, leading to the minimum valued area shifting from the centre of the crack surface when compared to the semi ellipse shape.

It is possible that the shape asymmetry can be quantified by using the magnitude of the normalised Bx (y axis in Figure 5.10) and the position of the signal trough (x axis in Figure 5.10), then the amount of error caused by the asymmetry when compared to an assumed semi ellipse can be derived from modelling results for the influences of different crack shapes, such as shown in Figure 5.9. Therefore corrections can be determined when characterising RCF cracks using individual ACFM scans (i.e. scan for the Bx signal parallel to the surface breaking component and at 45° for the Bz signal). It is reported that a wavelet network has been developed using the ACFM probe output signals to reconstruct the fatigue crack profiles [166], which is similar with the concept that using the magnitude of Bx and the position of the single trough to indicate the crack profile.

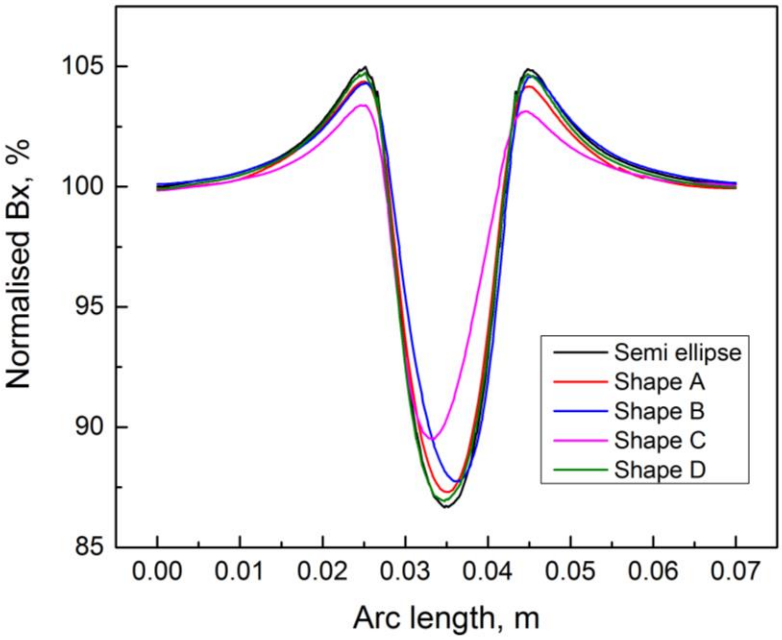

Figure 5.10 Normalised Bx signals recorded along the measurement line that is parallel to the crack surface-breaking component for different cracks shapes.

5.4 Summary

In this chapter, the influences of crack vertical angle on characterising single and multiple RCF cracks based on a single ACFM scan have been discussed. The variations of crack surface length, crack inner spacing and crack number for multiple cracks were modelled to investigate the influences of vertical angle (10° and 90°) on the $\Delta Bx_{max}/Bx$ values determined for multiple cracks. To determine the pocket length for multiple cracks, the influence of the vertical angle should be considered and the $\Delta Bx_{max}/Bx$ value needs to be compensated when the vertical angle is between 30° to 10°, which can be determined using the Bz trough-peak ratio along a 45° measurement line, as discussed in chapter 4. The asymmetrical crack shape also has an effect on the determination of pocket length and vertical angle. For accurate sizing of RCF cracks using a single ACFM scan the cracks should be regular (RCF cracks in light category and most cracks in moderate category, but it is in the moderate category that the crack shapes start to become asymmetric), where the assumption of semi ellipse shapes is appropriate.

The influence of crack vertical angle on pocket length sizing for multiple cracks could be included (via a compensation level) in the proposed neural network prediction approach where the database was established for multiple cracks with a vertical angle of 30° [151]. The neural network approach has been reviewed in section 2.5.

6. Sizing for non-uniformly sized crack clusters

6.1 Introduction

Real RCF cracks are generally present in the form of clusters, and some can have varying surface lengths, as shown in Figure 6.1. Figure 6.1a shows a cluster of four RCF cracks where the two on the left are about 20 mm in surface length but the two on the right are only about 10 mm in surface length; the spacing between the cracks is similar at about 10 mm. Figure 6.1b shows more closely spaced cracks with cracks at the left of the rail section being much shorter than the cracks at the right; some shorter cracks can be seen between adjacent large cracks; the surface length ranges from 2.3 to 21.7 mm and the crack spacing ranges from 0.8 to 3.8 mm. Regular sized RCF crack clusters are more common for rails subjected to mainly one type of traffic and variations in crack cluster patterns can reflect situations where the rail experienced a different mix of traffic [3].

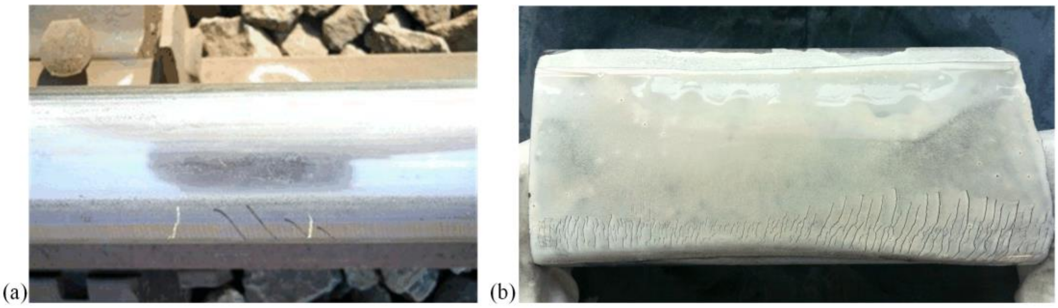

Figure 6.1 MPI images showing non-uniformly distributed RCF cracks at gauge side along the rail running direction.

Consideration of ACFM signal responses to crack pocket length and vertical angle for uniformly sized crack clusters has been discussed in chapter 5, which is a good starting point from where an investigation on non-uniformly sized crack clusters can be developed. As shown in Figure 6.1, RCF cracks within a cluster can vary in surface length and it is important to detect and size the deepest crack for the cluster. A scenario where the crack cluster is formed of 7 cracks (8 mm inner spacing), with the middle one being larger than the others is considered in this chapter (crack clusters 14 and 15 shown in Figure 3.4). This crack arrangement has been considered because the crack number (7) at this spacing (8 mm) gives a saturated signal (i.e. an increase in crack number does not change the signal) based on the results discussed in section 5.2.3, which allows the influence of the larger crack within the cluster to be discussed. Modelling and experimental work are discussed in this chapter for the non-uniformly sized crack clusters to investigate how Bx and Bz signals respond to the variations in surface length and spacing of cracks within the crack clusters; the difference to signals from uniformly sized crack clusters is discussed and it is shown that the signal can be compensated when sizing the non-uniform crack clusters based on the modelling results for uniformly sized crack clusters.

6.2 Model verification

Crack clusters 14 and 15 (as shown in Figure 3.4 and Table 3.3) were used to validate the modelling results on the non-uniformly sized crack clusters. Crack clusters 14 and 15 are comprised of cracks with a surface length of 5 mm and 10 mm, respectively and the middle cracks of both clusters are larger than the others, in both cases with a surface length of 15 mm. All cracks have an elliptical ratio of 1.25 and the inner spacing between the cracks is 8 mm.

Figure 6.2 and 6.3 shows a comparison between the modelling ACFM signals and the experimental measurements for crack clusters 14 and 15, respectively. The modelled normalised Bx for crack cluster 14 agrees with the experimental signal with a deviation of less than 1.1 % (with a standard error of 0.26). The Bx troughs show similar patterns between the model and the experiment; only five peaks and troughs can be seen in the signal, which is due to the indications from the small cracks (surface length of 5 mm) adjacent to the larger crack (surface length of 15 mm) being absent as the Bx trough of the large crack masks the signals for these smaller cracks. This will lead to an underestimation of the crack number from the signal. Although deviations between the modelled and measured signals for the smaller cracks in cluster 15 (as shown in Figure 6.3a), the Bx deviation for the middle larger crack is 0.9 % (with a standard error of 0.38), which means there is good agreement between the model and the experiment.

For the modelled Bz signals for cluster 14, as shown in Figure 6.2b, multiple peaks and troughs are observed with the middle larger trough and peak corresponding to the larger crack in the cluster. The experimental trough and peak values for the larger crack agree with the model and it can be distinguished from the troughs and peaks for the smaller cracks. However, for cluster 15 (shown in Figure 6.3b), the experimental trough and peak for the larger crack is influenced by those of the adjacent cracks, which is due to the “smaller” cracks being more similar in size (surface length of 10 mm). The measured signal for cluster 15 is more asymmetric than that for cluster 14 due to the non-uniformity of the steel plate microstructure (see section 2.2.1 for details of influences of different microstructures). The signals for both the model and the experiment are obtained from the 45° measurement line, as shown in Figure 6.4a, which crosses the centre of each surface-breaking component of the cracks, therefore signals for the larger crack can be influenced by the adjacent cracks. In experimental inspection using a single ACFM scan, particularly for real RCF cracks that are not as uniform as in the calibration clusters, the results will show far more complex signals than the modelling results. Therefore, it is expected that it will be difficult to distinguish the trough and the peak values from the 45° measurement line for any larger crack in a crack cluster, which will be a problem if determining the vertical angle of the larger crack is the priority.

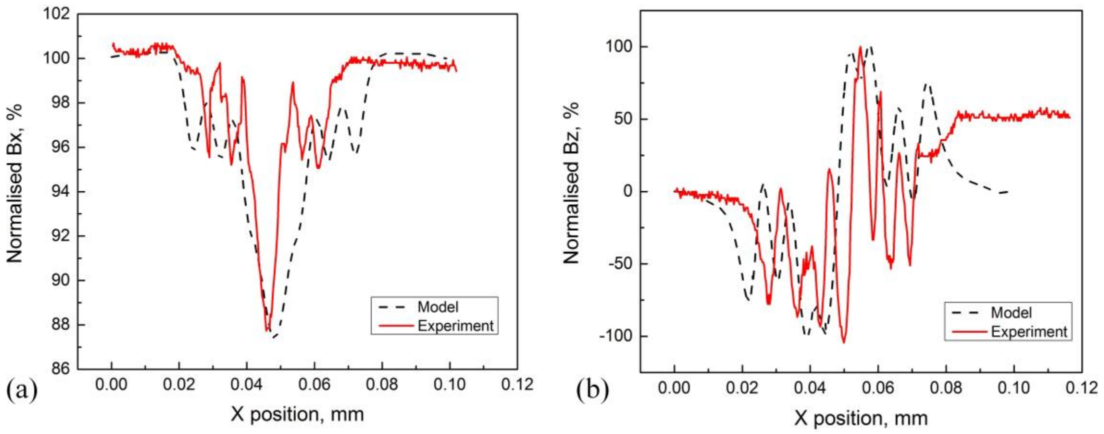

Figure 6.2 Comparison of modelling and experimental (a) Bx signals and (b) Bz signals for crack cluster 14.

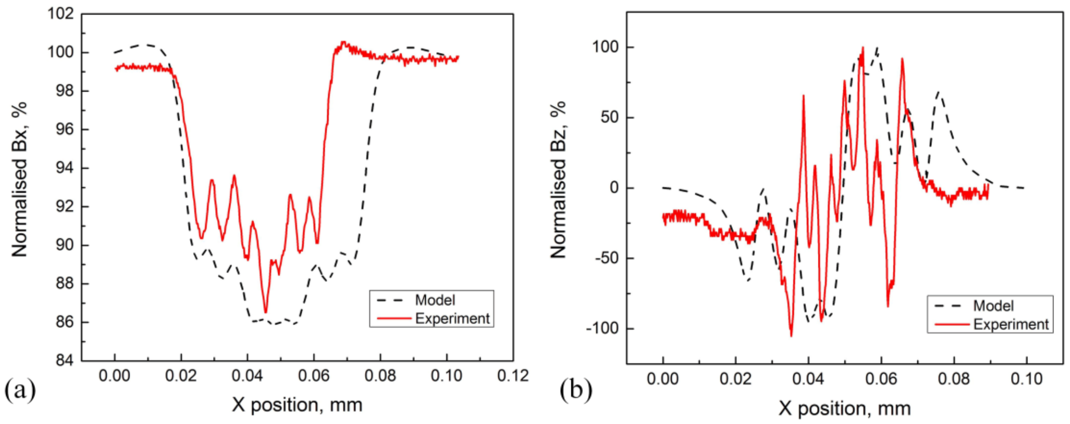

Figure 6.3 Comparison of Modelling and experimental (a) Bx signals and (b) Bz signals for crack cluster 15.

A 135° measurement line, as shown in Figure 6.4a, has also been used to determine the Bz trough-peak ratio for the larger crack within crack clusters. Figure 6.4b shows the Bz signals along the 135° measurement line for the non-uniformly sized crack cluster changing with the vertical angle. This measurement line crosses the centre of the larger crack therefore only one pair of trough and peak signals is observed, facilitating the recognition of the trough and peak values for the larger crack in the cluster. It also shows the variations of peak and trough values for different crack vertical angles and therefore can be used to determine the vertical angle in the present scenario.

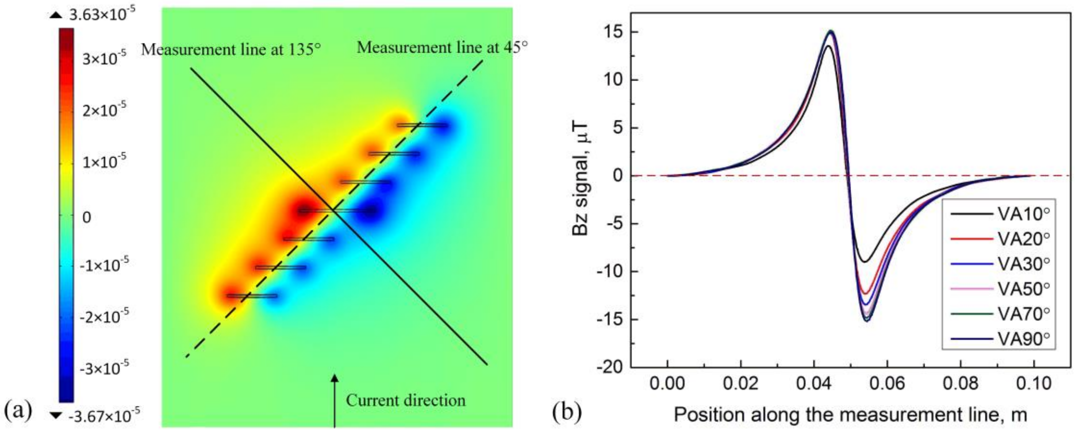

Figure 6.4 (a) Plan view of contour plots of the Bz magnetic field above crack clusters (surface length of 10 mm and pocket length of 4 mm) with the larger crack (surface length of 15 mm and pocket length of 6 mm) in the middle for vertical angle

of 90°; (b) Bz signals along a 135° measurement line from (a) for the crack cluster against vertical angle.

Figure 6.5 shows the modelling comparison for the $\Delta Bx_{max}/Bx$ value and the Bz trough-peak ratio for the crack with surface length of 15 mm (pocket length of 6 mm) when it presents in the form of a single crack, in a uniformly sized cluster (inner spacing of 8 mm) and in a non-uniformly sized cluster (inner spacing of 8 mm) where the other cracks are smaller (as shown for cluster 15 in Figure 6.4a), against crack vertical angle. Note that the Bz trough-peak ratio for the non-uniformly sized cluster is determined by using the 135° measurement line, as discussed in Figure 6.4 and the Bz trough-peak ratio is computed by Bz_{peak}/Bz_{trough}; other values are all determined using the 45° measurement line.

The $\Delta Bx_{max}/Bx$ values measured for the uniformly sized cluster with vertical angle of 90º using 45º and 135º measurement lines are 17.9 % and 17.6 %, respectively; the $\Delta Bx_{max}/Bx$ values for vertical angle of 10º are 13.5 % and 13.3 %, respectively. There is no big difference in the Bx signals recorded between the 45º and 135º measurement lines for the uniformly sized crack cluster. The Bz trough-peak ratio also shows similar values measured using 45º and 135º measurement lines for uniformly sized crack clusters (a difference less than 10 % for a cluster with vertical angle of 10º). These results are based on uniformly sized crack clusters with surface length of 15 mm and inner spacing of 8 mm. Differences caused by using the 45º and 135º measurement lines in the $\Delta Bx_{max}/Bx$ value and the Bz trough-peak ratio depend on the surface length and inner spacing; the difference becomes greater when the crack cluster has a longer surface length or smaller inner spacing.

In Figure 6.5, for the $\Delta Bx_{max}/Bx$ value, the non-uniformly sized crack cluster (cluster 15) leads to an overestimate of the pocket length for the larger crack at all vertical angles, e.g. for a vertical angle of 30°, the $\Delta Bx_{max}/Bx$ value for the larger crack in the non-uniformly sized cluster is 13.5 % while that for the single larger crack is 12.8 %, leading to an overestimate of the crack pocket length of about 1.1 mm. As shown in Figure 6.5a, the pocket length overestimation depends on the size of the other cracks in the cluster, indicated in the $\Delta Bx_{max}/Bx$ value for the uniformly sized cluster, in which the size of the other cracks increase to be equal to that of the larger crack. For the Bz trough-peak ratio, the non-uniformly sized crack cluster leads to a large overestimation of the crack vertical angle for the larger crack, e.g. when the larger crack has a vertical angle of 20° in the cluster it will be overestimated to about 55° based on the Bz trough-peak curve for the single crack. This is mainly caused by the different measurement angles (135° for the non-uniformly sized crack cluster and 45° for the uniformly sized crack cluster).

A larger crack in a non-uniformly sized crack cluster will be overestimated for both the pocket length and vertical angle if the sizing is based on the algorithm for a single crack; it will be underestimated for the pocket length and will be overestimated for the vertical angle if sized based on the algorithm for a uniformly sized crack cluster. Therefore it is important to investigate the Bx and Bz responses to non-uniformly sized crack clusters and the difference caused by the crack size, crack inner spacing and crack vertical angle should be analysed so that the larger crack can be accurately sized. Details will be discussed in following sections.

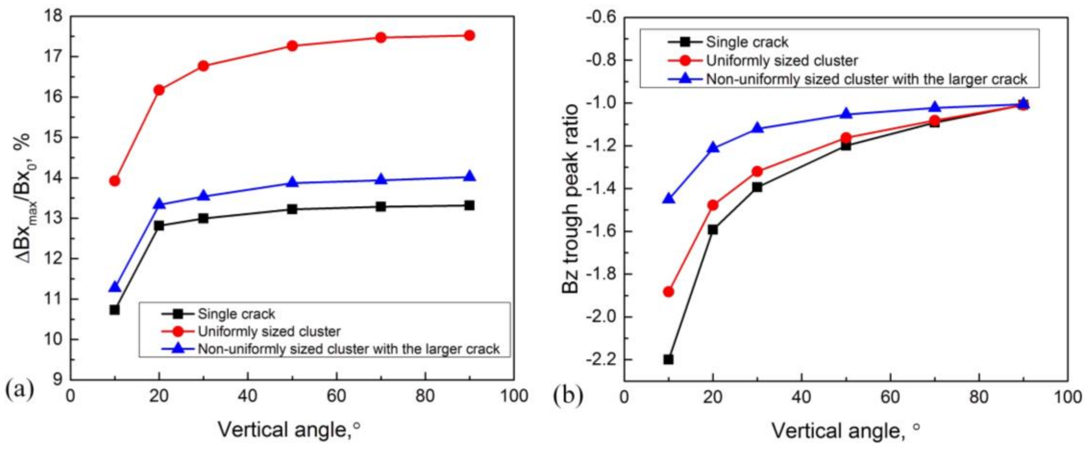

Figure 6.5 (a) The $\Delta Bx_{max}/Bx$ value; (b) the Bz trough-peak ratio for a crack with surface length of 15 mm (pocket length of 6 mm) present in the form of a single crack, a uniformly sized crack cluster and a non-uniformly sized crack cluster where the other surrounding cracks are smaller (surface length of 10 mm, as shown for the cluster 15), against crack vertical angle.

6.3 Variation of surface length in the non-uniformly sized cluster

Figure 6.6 shows the variations in the Bx and Bz signals for the larger crack (surface length of 15 mm and pocket length of 6 mm) within a non-uniformly sized crack cluster (inner spacing of 8 mm) when the surface length of the other cracks change from 3 mm to 15 mm. The results are compared with that for the larger crack in the form of a single crack. The crack cluster has 7 cracks and each of the cracks are 8 mm spaced. The Bz trough-peak ratio is determined by the peak and trough values along the 135° measurement line except for the single crack case (there is no difference in magnitude measured using 45° and 135° measurement lines for a single crack).

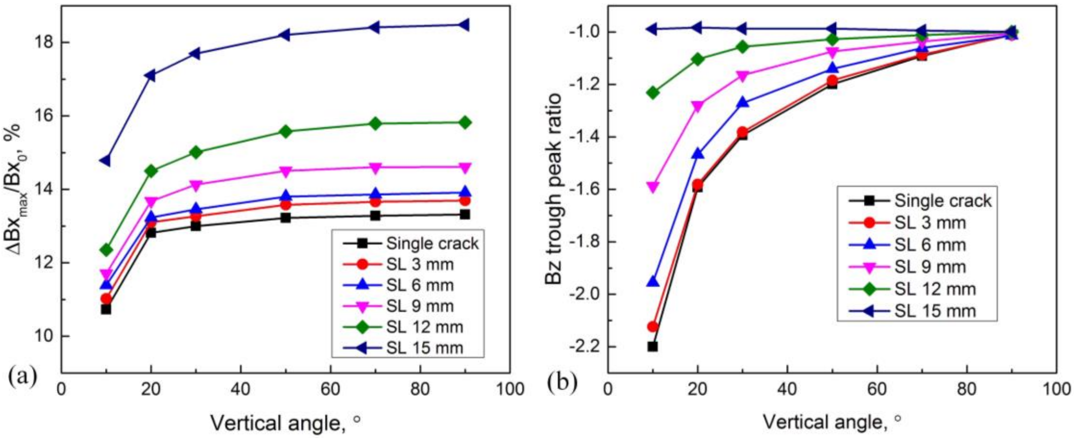

Figure 6.6 (a) The $\Delta Bx_{max}/Bx$ value; (b) the Bz trough-peak ratio for the crack with surface length of 15 mm (pocket length of 6 mm) present in the form of a single crack and a non-uniformly sized crack cluster when surface length of other cracks changes from 3 to 15 mm, against crack vertical angle (*SL* denotes the surface length).

As the surface length becomes greater, the influence of the adjacent cracks on the Bx and the Bz signals for the larger crack increases due to the increase in the surface length to inner spacing ratio. The results show that the pocket length and vertical angle prediction using the curves for single cracks will lead to over estimation in values. This, consequently, will give an over estimation of the vertical depth if the crack vertical angle or pocket length is known, respectively. An over estimation of the crack depth although not causing a serious safety issue, is undesirable as, from railway maintenance point of view, it increases the grinding depth therefore accelerating the replacement of the rails and reducing the service life.

6.4 Variation of inner spacing in the non-uniformly sized cluster

The non-uniformly sized crack cluster with the larger crack (as shown for cluster 15) in the middle has also been modelled to study the responses of the Bx and the Bz signals on the variation in inner spacing. The inner spacings considered ranged from 2 mm to 18 mm as this covers the range observed on samples taken from service, as discussed in section 1.2.

Figure 6.7 shows the Bx and Bz signals for the larger crack (surface length of 15 mm and pocket length of 6 mm) within the non-uniformly sized crack cluster when the inner spacing varies, against different vertical angle. The Bz trough-peak ratio is determined by the peak and trough values along the 135° measurement line except for the single crack case (there is no difference in magnitude measured using 45º and 135º measurement lines for a single crack). The results are also compared with that for the larger crack when it presents in the form of a single crack, so that any overestimation in pocket length and vertical angle for the larger crack in the non-uniformly sized crack cluster can be quantitatively analysed. The overestimated $\Delta Bx_{max}/Bx_0$ value decreases with an increase in the inner spacing and it begins to saturate when the inner spacing is about 14 mm (close to 15 mm, which is the surface length of the larger crack in the cluster). This agrees that the Bx signal beginning to plateau when the surface length to inner spacing ratio is smaller than 1, as discussed in section 5.2.2. With the increase in inner spacing, the influence of adjacent cracks on the larger crack signal decreases therefore the Bz trough-peak ratio is closer to that for the single crack. The Bz trough-peak ratio gives a small difference for different inner spacings at vertical angles of 50°-90°, shown in Figure 6.7b. As the vertical angle becomes shallower, i.e. less than 50° (which includes the typical vertical angles of RCF cracks in rails, 10°-30°), the Bz trough-peak ratio can be distinguished by different crack inner spacing.

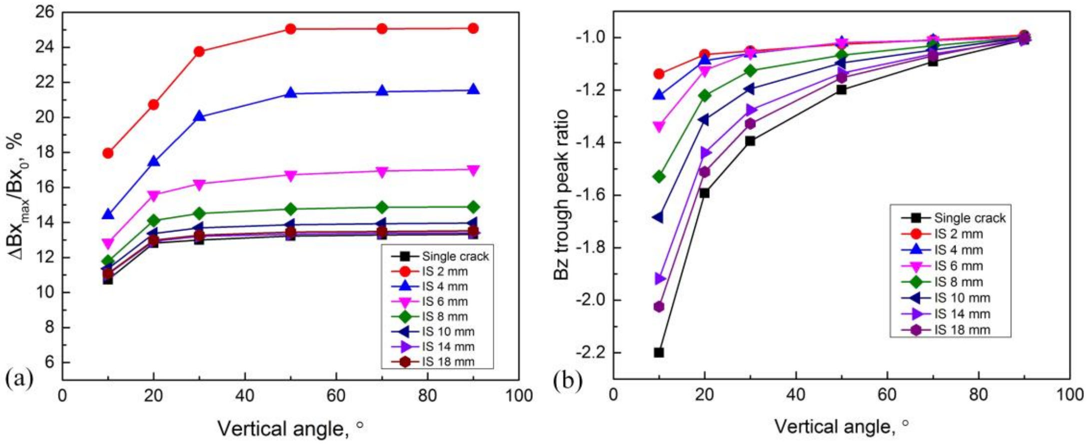

Figure 6.7 (a) The $\Delta Bx_{max}/Bx$ value; (b) the Bz trough-peak ratio for a crack with surface length of 15 mm (pocket length of 6 mm) present in the form of a single crack and a non-uniformly sized crack cluster when crack inner spacing varies from 2 to 18 mm, against crack vertical angle (*IS* denotes the inner spacing).

6.5 Variation of crack number in the non-uniformly sized cluster

The influence of crack number variation on the $\Delta Bx_{max}/Bx_0$ value and Bz trough-peak ratio for the larger crack (surface length of 15 mm and pocket length of 6 mm) in the non-uniformly sized crack cluster, against different vertical angles was also investigated. The crack number was increased equally on either side of the larger crack from 3 to 9; it has been observed in real RCF crack clusters that a larger crack typically exists between two or more relatively smaller cracks, or vice versa, as shown in Figure 6.1b. The Bz trough-peak ratio is determined by the peak and trough values along the 135° measurement line except for the single crack case.

Figure 6.8 shows that increasing the crack number from 3 to 9 does not change the $\Delta Bx_{max}/Bx_0$ value or the Bz trough-peak ratio significantly although all values for the cluster are different from that for the single crack thus leading to the overestimation of the pocket length and vertical angle if sizing based on the algorithm for single cracks.

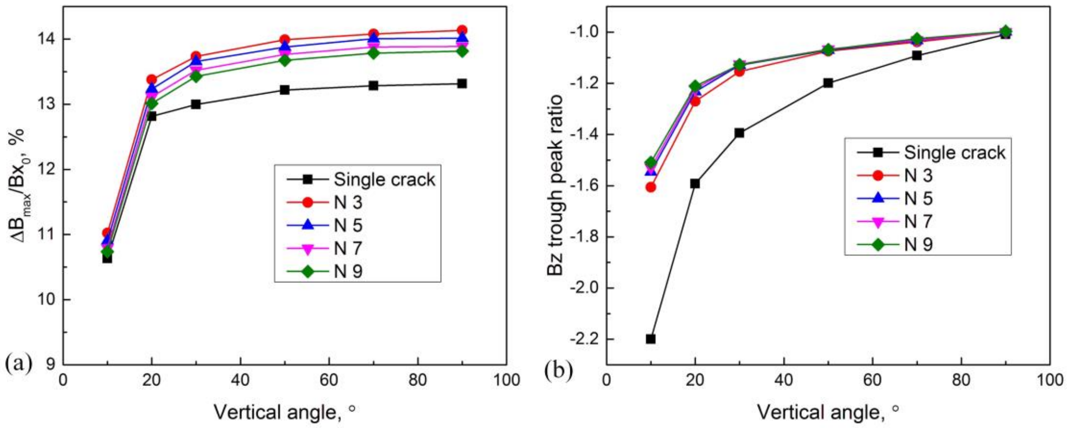

Figure 6.8 (a) The ΔBx_{max}/Bx value; (b) the Bz trough-peak ratio for a crack with surface length of 15 mm (pocket length of 6 mm) present in the form of a single crack and a non-uniformly sized crack cluster when the crack number varies from 3 to 9, against crack vertical angle (*N* denotes the crack number).

6.6 Summary

This chapter has discussed the responses of the Bx signal (the ΔBx_{max}/Bx value) and the Bz signal (the Bz trough-peak ratio) for non-uniformly sized crack clusters. A larger crack (greater in surface length and pocket length) present in the centre of the crack cluster with smaller cracks (e.g. crack clusters 14 and 15 shown in Figure 3.4) was considered to represent RCF crack clusters occurring in rails caused by mixed traffic. Calibration crack clusters were inspected and the results compared with the modelling outputs. The Bz trough-peak ratio along a 135° measurement line was proposed to determine the vertical angle of the larger crack in the non-uniformly sized crack cluster as this minimised interference in the signal from the neighbouring cracks. The influences of crack surface length, crack inner spacing, crack number and crack vertical angle on the Bx and Bz signals for the non-uniformly sized crack cluster were quantitatively analysed and the results compared to that for a single crack of the same dimensions as the central larger crack in the cluster.

7. Case study: Sizing for RCF cracks taken from service

7.1 Single cracks

As shown in Figure 3.5, RCF crack 16 on the sample taken from service was selected to be ACFM inspected and progressive milled, as the case study for single RCF cracks inspection, and the predicted and the measured crack vertical angle and crack pocket length were compared. Figure 7.1 shows the normalised Bx and Bz signals measured by the ACFM pencil probe sensor for the single RCF crack 16. The Bx and Bz signals were determined using six measurements and the average value was taken to estimate the pocket length and vertical angle. The background signal (the value of 100 % for the Bx signal and the value of 0 % for the Bz signal) was constant (± 0.7 % for Bx signals and ± 6.2 % for Bz signals) for all 6 measurements at the beginning of each scan but varied after the scan since the scan line was carried out over the gauge corner (curved profile) of the rail and the measurements were made by hand, therefore the conformity of the sensor to the rail curvature was not reproducible. As the background value for ΔBx_{max}/Bx and Bz trough-peak ratio computations was determined using the data from the beginning of each scan (i.e. from the background on the left of the trough), the divergence of background signals after the scan does not influence the values need for pocket length and vertical angle predictions.

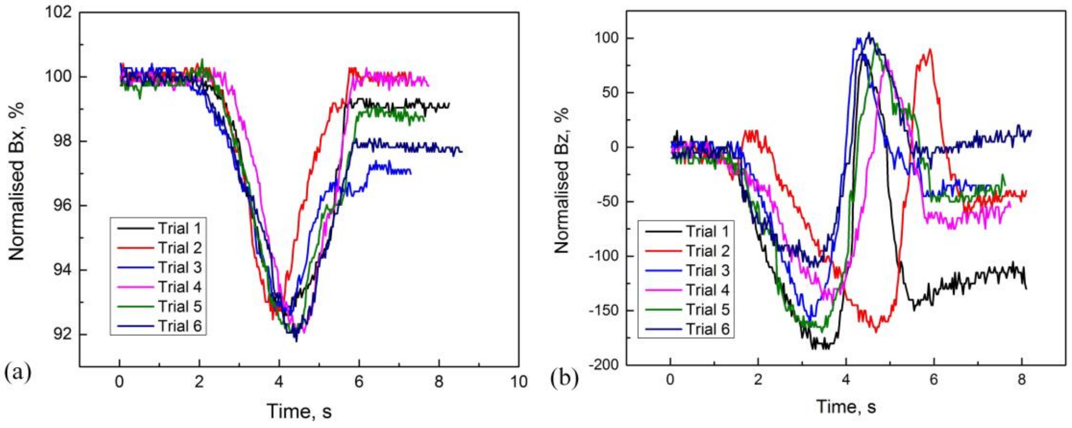

Figure 7.1 The experimental normalised (a) Bx and (b) Bz signals for the single RCF crack 16 shown in Figure 3.5.

The single RCF crack was progressive milled to investigate the actual dimensions (pocket length and vertical angle). The milling direction is shown in Figure 3.8a. Figure 7.2 shows the MPI images of each progressive milling stage (1 mm spacing) and the corresponding pocket length and the vertical angle measured from each image for the crack. The figure indicates that the maximum pocket length is 6.1 mm (errors < 0.1 mm) with a vertical angle of 28.1° (errors < 1°) occurring at the milling stage of +3 mm. This is similar to the result obtained by X-ray tomography (see Figure 3.8) which indicates a maximum pocket length of 6.0 mm (errors < 0.12) mm with a vertical angle of 25.7° (errors < 0.1°).

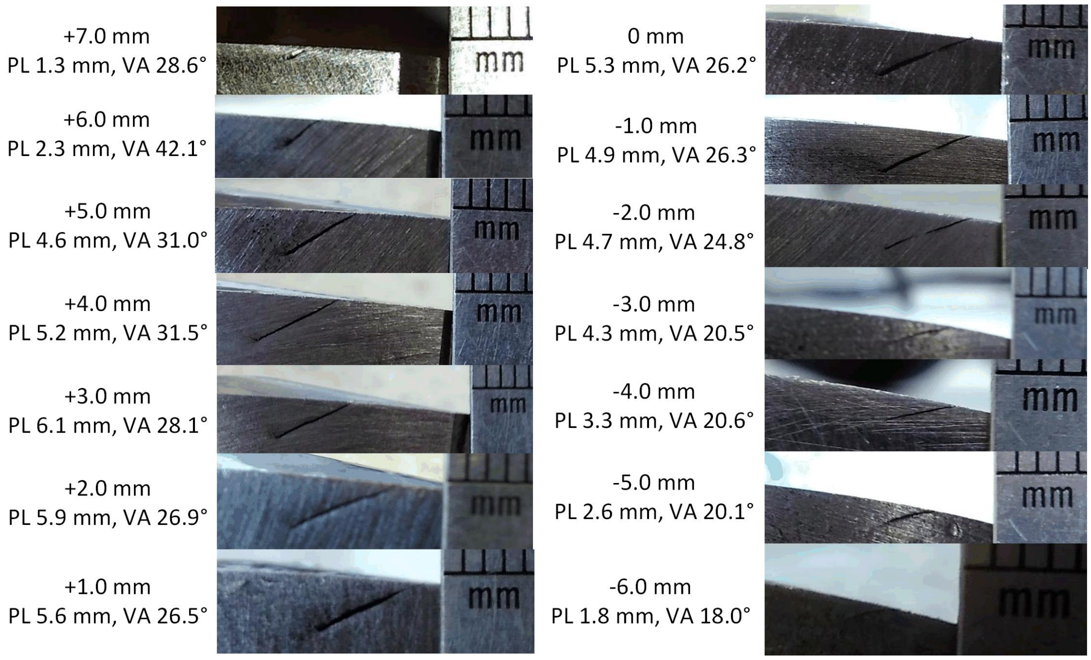

Figure 7.2 Images of each progressive milling stage for RCF crack 16; the milling stages from the crack centre (visual) milling stage are given in ± mm (*PL* denotes the pocket length and *VA* denotes the vertical angle; length measurement errors < 0.1 mm and angle measurement errors < 1°).

The actual crack dimensions are compared with the predicted results based on the Bx signal compensated for vertical angle (discussed in section 5.1). The results are listed in Table 7.1 and the $\Delta Bx_{max}/Bx_0$ and the Bz trough-peak ratio with standard errors were obtained from the ACFM measurements on crack 16 (shown in Figure 7.1). The predicted pocket length and vertical angle were obtained by comparison to the modelling results for a single RCF crack in Figure 2.21 (from a previous study) and

Figure 4.8 (from the present study), respectively, assuming an elliptical ratio of 1. Actual crack dimensions (crack pocket length, crack vertical angle and crack vertical depth) are all based on measurements of images obtained from the progressive milling. It was found that the maximum vertical angle is 42.1° but at this location the pocket length is only 2.3 mm, which gives a vertical depth of 1.5 mm, less than the measured maximum vertical depth of 2.9 mm at the milling stage of +3 mm where the pocket length is 6.1 mm and the vertical angle is 28.1º. Therefore the maximum vertical depth does not necessarily coincide with the maximum pocket length.

The average vertical angle is 24.5°, which compares well with the predicted vertical angle of 21.0°. The predicted vertical angle is smaller than measured, with a deviation of 14.3 %, which may be due to the crack being located at the curved gauge side of the rail (shown in Figure 3.8b) leading to the trough and peak values of the Bz signals to be more asymmetrical than that if the crack were in a sample with a flat surface. The predicted pocket length (using an uncorrected prediction for a single crack with a 90º vertical angle) is significantly smaller than the actual value (relative difference of 54.1 %) because the crack vertical angle is shallower and this causes the $\Delta Bx_{max}/Bx_0$ value to be smaller than that for a larger vertical angle for a crack with the same pocket length (see discussion in section 5.1). If the corrected prediction is made to account for the vertical angle (21.0°) of the crack then the predicted pocket length is 5.0 mm, greatly decreasing the relative difference from 54.1 % to 17.4 %. As the pocket length and the vertical angle are both underestimated, the crack vertical depth is underestimated by about 35.4 %. The asymmetrical shape of crack 16 also gives a deviation between the predicted and the actual pocket length as discussed in section 5.3 and may account for the errors between the actual and predicted crack dimensions.

Table 7.1 Results of predicted dimensions for the single RCF crack 16 and the comparison to the actual crack dimensions.

RCF crack	16	Measured and predicted error
$\Delta Bx_{max}/Bx_0$ with standard difference	7.90	0.34 %
Bz trough-peak ratio with standard difference	-1.75	0.12 %
Predicted pocket length (uncorrected)	2.8 mm	0.1 mm
Predicted vertical angle	21.0°	1°
Predicted vertical depth	1.0 mm	0.1 mm
Actual maximum pocket length	6.1 mm	0.1 mm
Actual average vertical angle	24.5°	1°
Actual maximum vertical depth	2.9 mm	0.1 mm
Relative difference for pocket length	54.1 %	-
Relative difference for vertical angle	14.3 %	-
Relative difference for vertical depth	64.3 %	-
Compensation for pocket length	2.6 %	0.1 %
Predicted pocket length (compensated)	5.0 mm	0.1 mm
Relative difference for pocket length (compensated)	17.4 %	-
Predicted vertical depth (compensated)	1.8 mm	0.1 mm
Relative difference for vertical depth (compensated)	35.4 %	-

Although the vertical angle is underestimated, the relative difference is small (a difference in angle of 3.5º) and the main reason for the deviation is because the modelling results are based on a rail model with a flat surface and the trough and peak values of the Bz signal are more asymmetrical for a curved rail surface. The compensation method used for the pocket length sizing algorithm greatly decreases the difference in the predicted pocket length (54.1 % to 17.4 %) but the asymmetrical crack shape still causes some error for pocket length. Hence it has been shown that to accurately size a semi-elliptical single RCF crack, the vertical angle of the crack should be determined from the Bz trough-peak ratio then appropriate compensation for the pocket sizing algorithm can be made to eliminate the effect of the crack vertical angle on the Bx signals.

7.2 Multiple cracks

RCF crack clusters 17 and 18 (shown in Figure 3.5) on the sample taken from service were selected as the case study for sizing multiple cracks using ACFM signals. Crack clusters 17 and 18 were grid scanned using the ACFM pencil sensor controlled by a robotic arm. They were then progressive milled to investigate the actual crack pocket length, crack vertical angle and crack vertical depth into the rail. MPI images after each milling stage were taken (e.g. as shown in Figure 3.9) and the crack dimensions were recorded and are listed in Tables 7.2 and 7.3. The milling stages are represented in mm indicating the distance from the rail gauge side of each stage (milling starts at 9 mm away from the gauge side, where the crack begins to be observed from the cross section of the rail). Cracks 1 and 4 in cluster 17 are discontinuous as they cannot be observed at the milling stage 14 and 17 mm, respectively.

Table 7.2 Summary of crack dimensions for each of the cracks in crack cluster 17 (milling stage refers to the distance from the rail gauge side; *PL* denotes pocket length, *VA* denotes vertical angle and *VD* denotes vertical depth; the values shown with a '*' refer to when the crack was not surface-breaking; length measurement errors < 0.1 mm; angle measurement errors < 1°).

Milling stage, mm	Crack cluster 17											
	1			2			3			4		
	PL, mm	VA, °	VD, mm	PL, mm	VA, °	VD, mm	PL, mm	VA, °	VD, mm	PL, mm	VA, °	VD, mm
9	0.7	18.9	0.2	1.9	17.2	0.6						
10	1.3	25.3	0.5	2.3	19.1	0.8	1.4	26.5	0.6			
11	1.5	26.3	0.7	2.6	18.6	0.8	1.8	21.6	0.7	0.4	25.3	0.2
12	1.6	30.7	0.8	3.3	19.8	1.1	2.7	24.7	1.1	1.2	28.3	0.6
13	1.6	27.0	0.7	3.9	25.8	1.7	3.4	25.2	1.5	2.3	17.2	0.7
14	-	-	-	4.2	22.2	1.6	4.2	29.7	2.1	2.6	21.8	1.0
15	2.3	20.6	0.8	4.7	18.1	1.5	4.5	24.2	1.8	3.0	21.0	1.1
16	3.4	19.9	1.1	6.1	16.6	1.8	4.8	20.0	1.7	3.1	17.6	1.0

17	3.5	18.1	1.1	7.0	12.3	1.5	4.5	16.6	1.3	-	-	-
18	4.8	15.3	1.3	4.4*	12.1	0.9*	4.4	16.8	1.3	1.3	24.2	0.5
19	6.2	12.0	1.3				3.0*	17.4	0.9*	2.4	15.6	0.7
20							2.63*	15.5	0.70*	3.61	16.2	1.0
21							2.53*	14.7	0.64*	3.01	11.3	0.6
22							2.00*	12	0.42*	3.00	12	0.6

Table 7.3 Summary of crack dimensions for each of the cracks in the crack cluster 18 (milling stage refers to the distance from the rail gauge side; *PL* denotes pocket length, *VA* denotes vertical angle and *VD* denotes vertical depth; the values shown with a '*' refer to when the crack was not surface-breaking; length measurement errors < 0.1 mm; angle measurement errors < 1°).

Milling stage, mm	Crack cluster 18											
	5			6			7			8		
	PL, mm	VA, °	VD, mm	PL, mm	VA, °	VD, mm	PL, mm	VA, °	VD, mm	PL, mm	VA, °	VD, mm
9	0.50	22.4	0.2							1.86	20.1	0.6
10	1.56	19.4	0.5	1.2	17.0	0.4	1.1	19.9	0.4	2.8	20.9	1.0
11	2.30	24.2	1.0	2.0	24.1	0.8	2.0	24.8	0.8	3.8	19.2	1.2
12	2.42	24.1	1.0	2.9	23.5	1.2	2.4	24.2	1.0	4.6	20.1	1.6
13	3.58	21.1	1.3	3.3	22.4	1.3	3.3	22.1	1.2	5.4	18.4	1.7
14	3.98	18.7	1.3	3.4	22.6	1.3	4.2	17.4	1.3	5.7	17.9	1.8
15	4.32	19.5	1.4	3.7	26.7	1.7	4.3	19.2	1.4	7.0	14.6	1.8
16	4.37	15.0	1.1	4.0	22.9	1.6	4.6	16.9	1.4	7.6	14.1	1.9
17	4.69*	14.8	1.4*	4.1	25.7	1.8	5.6	13.1	1.3	7.6	14.4	1.9
18	3.81*	15.3	1.7*	6.1	9.3	10.	5.9	18.8	1.9	8.7	11.9	1.8
19				4.9*	10.0	1.1*	6.8	17.3	2.0	8.7	13.6	2.0
20							5.2	15.3	1.4	9.8	10.9	1.9
21							3.8*	13.8	1.4*	11.6	9.0	1.8

Figure 7.3 shows a map of the x and the z components of the magnetic field reconstructed from the ACFM grid scanning signals. Cracks are assumed to be straight and are represented as black lines in the figure indicating the crack arrangement for clusters 17 and 18. From the magnetic field mapping, the minimum value of the Bx magnetic field (for pocket length) and the minimum and maximum values of the Bz magnetic field (for vertical angle) can be accurately determined,

This scenario represents scanning with an array probe [119] or robotic system [137, 138] with appropriate signal analysis.

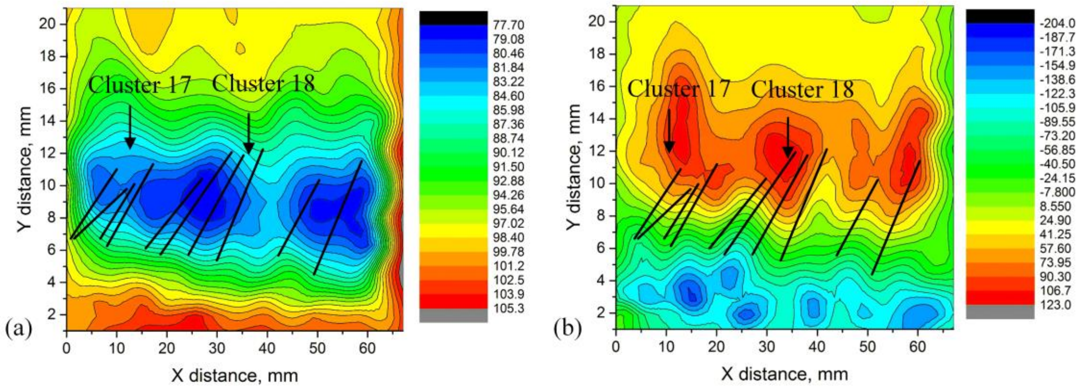

Figure 7.3 (a) Bx and (b) Bz signal maps using grid scanning with an ACFM pencil sensor (crack positions are superimposed on the map by black lines).

Table 7.4 shows the predicted crack dimensions compared with the actual dimensions for crack clusters 17 and 18. The $\Delta Bx_{max}/Bx_0$ values and the Bz trough-peak ratios were obtained from the magnetic field maps constructed from the ACFM signals. The pocket lengths and vertical angles are predicted using the measured $\Delta Bx_{max}/Bx$ values and the Bz trough-peak ratios by comparison to the modelling results for multiple cracks with a uniform size (taken as the average surface length and average inner spacing from the MPI data) as discussed in sections 4.4.5 and 5.2, and an assumed semi-ellipse ratio of 1 (which, from the rail maintenance point of view, can give a prediction of the maximum pocket length and vertical depth to ensure the cracks are removed completely). The actual pocket length and vertical angle are taken as the average of the maximum values for each crack in the cluster. The vertical angle prediction gives a maximum relative difference to the average dimension of less than 13.6 % for the inspected crack clusters. The relative differences are even smaller (7.0 % and 4.6% for clusters 17 and 18, respectively) if compared with the actual maximum vertical angle (30.7° and 26.7° for clusters 17 and 18, respectively). The pocket length prediction gives relatively large difference (24.1 % for cluster 17 and 37.0 % for cluster 18) taking the influence of crack vertical angle, crack shape and the non-uniformity of cracks into account.

Compensation values of 3.8 % and 4.3 % are required for crack clusters 17 and 18 respectively for the $\Delta Bx_{max}/Bx_0$ value to account for the predicted vertical angle of 33° for RCF crack cluster 17 and 28° for RCF crack cluster 18. For crack cluster 17 the compensation was used with model results for cracks with surface length of 11.6 mm and inner spacing of 3.9 mm, and for crack cluster 18 cracks with surface length of 12.7 mm and inner spacing of 4.4 mm were used. The compensation greatly decreases the pocket length prediction difference for both of the inspected crack clusters however for cluster 18, a relatively large difference is still observed (24.7 %), and this is probably due to the cluster being comprised of large cracks with an elliptical ratio of 0.87. The crack sizing algorithm and the compensation are based on modelling results for semi-ellipse cracks with an elliptical ratio from 1 to 1.75 and will be less accurate if used for single cracks or crack clusters with an elliptical ratio out of this range.

The actual vertical depths are computed from the actual pocket length and vertical angle. The results in Table 7.2 and Table 7.3 show that the position of the maximum vertical depth does not coincide with the positions where the maximum pocket length or the maximum vertical angle are seen. The predicted vertical depth is derived from the predicted pocket length and vertical angle (i.e. the maximum values), therefore errors will exist for the predicted vertical depth. For cracks studied in this work, these errors are even greater when compensation for pocket length prediction based on the predicted vertical angle is used. The vertical depth is overestimated but from a railway maintenance point of view, overestimations are safer as then the crack will be completely removed from the railway rails, but will reduce the overall life of the rail. The results may be specific to these cracks only and it is probably due to the different elliptical shape (vertical depth is not overestimated for the single crack discussed in section 7.1). Further work investigating whether the vertical angle compensation results in increased conservatism in vertical depth prediction should be carried out.

Table 7.4 Results of predicted dimensions for RCF crack clusters 17 and 18 and the comparison to the actual crack dimensions.

RCF crack cluster	17	18	Measured and predicted error
$\Delta Bx_{max}/Bx_0$	19.54 %	22.22 %	0.26 %
Bz trough-peak ratio	-1.30	-1.38	0.14 %
Predicted pocket length	4.1 mm	4.6 mm	0.1 mm
Predicted vertical angle	33.0°	28.0°	1°
Predicted vertical depth	2.2 mm	2.2 mm	0.1 mm
Actual pocket length	5.4 mm	7.3 mm	0.1 mm
Actual vertical angle	28.6°	24.2°	1°
Actual maximum vertical depth	1.8 mm	2.0 mm	0.1 mm
Relative difference for pocket length	24.1 %	37.0 %	-
Relative difference for vertical angle	13.3 %	13.6 %	-
Relative difference for vertical depth	18.1 %	9.1 %	-
Compensation for pocket length	3.8 %	4.3 %	0.1 %
Predicted pocket length (compensated)	4.8 mm	5.5 mm	0.1 mm
Relative difference for pocket length (compensated)	11.1 %	24.7 %	-
Predicted vertical depth (compensated)	2.6 mm	2.6 mm	0.1 mm
Relative difference for vertical depth (compensated)	31.3 %	23.1 %	-

7.3 Summary

This chapter has presented case studies for single and multiple RCF cracks using the sizing method based on the modelling results for crack vertical angle and crack pocket length. The vertical angle is determined prior to the pocket length and the amount of compensation for pocket length prediction can be calculated based on the obtained vertical angle.

For the single RCF crack with surface length of 12.6 mm, pocket length of 6.1 mm and vertical angle of 24.5°, ACFM measurement gives a predicted vertical angle of

21° (relative difference 14.3 %) and a compensation of 2.6 % is added to the $\Delta Bx_{max}/Bx_0$ value, decreasing the relative difference of pocket length from 54.1 % to 17.4 %. The prediction of vertical depth using the compensation is 1.8 mm, decreasing the difference from 64.3 % to 35.4 %.

For crack clusters 17 (average surface length 11.6 mm, average inner spacing of 3.9 mm and pocket length of 5.4 mm) and 18 (average surface length 12.7 mm, average inner spacing of 4.4 mm and pocket length of 7.3 mm), the difference for vertical angle prediction is less than 13.6 % and the pocket lengths using the compensation are 4.8 mm and 5.5 mm decreasing the difference from 24.1 % to 11.1% and from 37.0 % to 24.7 % for clusters 17 and 18, respectively. However, the vertical depth prediction using the compensation increases the error for these cracks but it is safer as the crack will be completely removed from a railway maintenance point of view. Further work investigating whether the vertical angle compensation results in increased conservatism in vertical depth prediction should be carried out.

There are some deviations between the actual and predicted dimensions for single and multiple RCF cracks as the sizing algorithm is based on the modelling results for regular semi-elliptical cracks with elliptical ratio from 1 to 1.75. Cracks with asymmetrical crack shapes or with elliptical ratios out of this range (1 to 1.75) will lead to the dimension sizing being inaccurate. In addition, the slight differences in crack surface lengths in clusters 17 and 18 also give errors when using the results of the model for uniformly sized crack clusters.

8. Conclusions

Alternating current field measurement can be used to non-destructively detect and characterise rolling contact fatigue cracks in railway rails, as ACFM signals (Bx and the Bz signals) are sensitive to changes in crack surface length and pocket length for light to moderate cracks (classified by Network Rail, Figure 2.7). This work focused on ACFM responses to variations in crack vertical angle for single RCF cracks and to variations in surface length (elliptical ratio), inner spacing and crack number for uniformly and non-uniformly sized multiple RCF cracks.

A novel method using the Bz trough-peak ratio (from the Bz signal) has been proposed to predict the crack vertical angle. The predicted vertical angle can then be used with the predicted pocket length (obtained from the Bx signal) to give the vertical depth the cracks have propagated to. This is important for railway maintenance for elimination of the RCF cracks from railway rails. It has been found that crack vertical angle also influences the Bx signals used for pocket length determination and this has been quantitatively investigated for single and multiple RCF cracks. Appropriate compensation of the Bx signals can be implemented, based on the determined vertical angle, when sizing the pocket length of RCF cracks. Case studies on single and multiple RCF cracks on rail samples taken from service have shown that the Bz trough-peak ratio can be used for crack vertical angle determination and the compensation determined from the vertical angle can decrease the error in pocket length prediction. The main conclusions of the research are as follows:

For the crack vertical angle determination using ACFM signals:

- The Bx signal is sensitive to crack vertical angle when the vertical angle is less than 30°. The Bx signal from a single scan measurement increases as the vertical angle becomes shallower because the Bx trough moves further away from the centre of the crack opening, therefore the minimum Bx value recorded is not the actual minimum value of the Bx magnetic field. The effect of crack vertical angle on the Bx signal, and hence pocket length measurement, for cracks with vertical angles less than 30° has been determined; errors of 50 % in crack pocket length value (under estimate) result for a crack of 3.2 mm pocket length and a 10° vertical angle of propagation if basing the pocket length estimate on sizing methods applicable to vertical cracks.

- The Bz trough-peak ratio, from ACFM single scan measurement through the crack centre along a line at 45° to the crack surface length, has been shown to vary with the crack vertical angle, with this variation also being influenced by crack surface length. The modelling results and measurement on calibration cracks (crack 1-7) show that the crack vertical angle can be determined from the measured Bz trough-peak ratio, provided the crack surface length is known.

- The angle of the ACFM measurement line has a significant influence on the Bz trough-peak ratio. It is difficult to distinguish the crack vertical angle using the Bz trough-peak value when the measurement angle is less than 20°; the Bz trough-peak ratio starts to saturate at larger measurement angles, e.g. 75° and 65° for a crack with surface length of 8 and 15 mm, respectively. The Bz trough-peak ratio is insensitive to the sensor lift-off for cracks with vertical angles between 90° to 50°. However, the influence of lift-off becomes significant when the crack vertical angle is between 30° to 10°. A maximum difference of 30.5% in value is observed for a 10° vertical angle crack when the lift-off changes from 0 mm to 5 mm, which will cause an over estimation of 30° in the vertical angle.

- The Bz trough-peak ratio along the measurement line at an angle of 45° to the crack surface-breaking component can be used to determine the vertical angle for uniformly sized crack clusters, but it is different to that for the same sized single cracks, as the signal is influenced by the adjacent cracks in the cluster. Changes in surface length and inner spacing also influence the relationship between the Bz trough-peak ratio and the crack vertical angle.

For characterisation of single and uniformly sized RCF cracks using ACFM signals:

- The influence of crack vertical angle on $\Delta Bx_{max}/Bx$ values for single RCF cracks with surface lengths of 8, 15 and 21 mm has been quantitatively analysed and compared for three data extraction methods, i.e. $\Delta Bx_{max}/Bx$ extracted from the 0° measurement line, the 45° measurement line and the minimum value directly from the x-component of the magnetic field (i.e. from full model results that would represent grid scans). The $\Delta Bx_{max}/Bx$ values from these three methods decrease significantly when the crack vertical angle is less than 30°; the differences in $\Delta Bx_{max}/Bx$ values from the three methods are greater at shallower vertical angle and it becomes greater for cracks with larger surface lengths, e.g. the deviation between the minimum value of the Bx magnetic field and the value recorded along the 0° measurement line is 9.0 % for a crack with 21 mm surface length at a vertical angle of 10°, but for the crack with 8 mm surface length it is only 2.4 %.

- Responses of ACFM signals to uniformly sized crack clusters when the crack surface length (3 to 40 mm), crack inner spacing (2 to 20 mm), crack number (3 to 9) and crack vertical angle (90° and 10°) varied have been investigated. Deviations in the $\Delta Bx_{max}/Bx$ value caused by the vertical angle change from 90° to 10° are observed and the deviation decreases for larger crack surface lengths but begins to saturate when the surface length is about 33 mm; the $\Delta Bx_{max}/Bx_0$ value decreases as the crack inner spacing increases but begins to saturate at a spacing of 12 mm for both crack vertical angles of 90° and 10°. The ratio of surface length to inner spacing is more important than the influence of inner spacing on the $\Delta Bx_{max}/Bx_0$ value for a crack cluster and it can be used to indicate whether the inner spacing is great enough to eliminate the influence of the adjacent crack on the Bx signal; the $\Delta Bx_{max}/Bx$ value increases when the crack number increases up to 6 then the value begins to saturate. The $\Delta Bx_{max}/Bx$ value for the cluster with the shallow vertical angle (10°) is significantly lower than that for the 90° vertical angle and it saturates at a larger value of crack number when the ratio of the crack surface length to the crack inner spacing increases

- Calibration crack clusters (clusters 8-13) were used to verify the modelling results for the Bx responses to uniformly sized crack clusters (vertical angle of 90°) with variations in crack surface length, crack inner spacing and crack number. The results show that the predicted pocket lengths generally agree with the actual values with an average deviation of less than 10 %. The predicted pocket length is underestimated for all crack clusters due to the machined cracks having a slightly asymmetrical shape to the centre of the crack.

- For crack clusters with a shallow vertical angle, the pocket length prediction should be compensated for the difference in signal caused by the shallow vertical angle, the amount of which depends on the crack surface length, the inner spacing and the crack number. For example, for sizing a multiple crack cluster, the crack vertical angle should be determined using the Bz trough-peak ratio proposed in the present study, then the amount of compensation for pocket length prediction can be considered according to the vertical angle range (90° to 30° or 30° to 10°) for the different surface length, inner spacing and crack number arrangements.

- Any asymmetry in the crack profile results in an error in crack sizing when using the ACFM signals obtained through a single ACFM scan, e.g. the predicted vertical angle will be smaller than reality if using an assumed semi ellipse shape for the predictions. The study indicated that for accurate sizing of RCF cracks using a single ACFM scan the cracks should be regular, where the assumption of semi ellipse shapes is appropriate. For cracks with irregular shapes, the Bx signal from the measurement line parallel to the crack surface length can be used to indicate the asymmetry; corrections can be determined according to the modelling results on influences of different crack shapes when characterising RCF cracks using a single ACFM scan.

For characterisation of non-uniformly sized crack clusters using ACFM signals:

- Calibration crack clusters 14 and 15 were used to validate the modelling results on non-uniformly sized crack clusters (same sized and spaced cracks with a larger crack in the middle). The Bx troughs show similar patterns between the model and the experimental measurements for the cluster with the larger crack in the middle of the cluster (deviations less than 1.1 % and 0.9 % for cluster 14 and 15 respectively). For the Bz trough-peak ratio, although the maximum and minimum modelling values from the 45° measurement line agree with the experiments, the troughs and peaks for the larger cracks are adversely influenced by those of the adjacent cracks. In the experimental inspection using a single ACFM scan, particularly for real RCF cracks that are not as uniform as the calibration clusters, the signal has a far more complex pattern than the modelling results show for calibration clusters. Therefore, it is expected that it will be difficult to distinguish the trough and the peak values from the 45° measurement line for any larger crack in the crack cluster if determining the vertical angle of the larger crack is the priority.

- A 135° measurement line was used to determine the Bz trough-peak ratio for the larger crack within the crack clusters. This measurement line crosses the centre of the larger crack and only one set of trough and peak values is observed, facilitating recognition of the trough and peak values for the larger crack in the cluster. It also showed the variations of peak and trough values for different crack vertical angles and therefore can be used to determine the vertical angle in the present scenario.

- Modelling results show that the $\Delta Bx_{max}/Bx$ value and the Bz trough-peak ratio from the 135° measurement line for the larger crack in the non-uniformly sized crack cluster is different from that for the single crack or the uniformly sized crack cluster. The Bx and Bz responses to the non-uniformly sized crack cluster and the difference caused by the crack size, crack inner spacing and crack vertical angle should be analysed so that the larger crack can be accurately sized for the studied scenario.

For the case study on sizing RCF cracks in rails taken from service:

- The single RCF crack (crack 16) in the rail taken from service was inspected manually by moving the ACFM pencil probe sensor at 0 mm lift-off along the surface-breaking component for pocket length and across the centre of the crack at an angle of 45° to the crack opening (sensor with an orientation parallel to the crack surface-breaking component) for vertical angle. The ACFM predictions were compared with the actual crack dimensions measured from progressive milling. The vertical angle prediction shows a relative difference of 14.3 % (predicted value of 24.5° to measured value of 21°); this gives a compensation of pocket length prediction of 2.6 %, decreasing the pocket length relative difference from 54.1 % to 17.4 % and vertical depth relative difference from 64.3 % to 35.4 %.

- The remaining errors between the predicted and actual crack dimensions for single RCF cracks are due to the model being based on cracks in a sample with a flat surface, whilst the trough and peak values of the Bz signal are more asymmetrical for the curved rail surface; in addition the asymmetrical crack shape also causes some error for predicted pocket length.

- To accurately size a semi-elliptical single RCF crack, the vertical angle of the crack should be determined from the Bz trough-peak ratio then the appropriate compensation for pocket sizing determined to eliminate the effect of the crack vertical angle on the Bx signals.

- Crack clusters 17 and 18 in the rail taken from service were grid scanned using the ACFM pencil probe sensor installed on a robotic arm. The $\Delta Bx_{max}/Bx_0$ values and the Bz trough-peak ratio were obtained from the magnetic field map constructed from the ACFM signals from grid scanning. The vertical angle predictions are reasonable as the maximum relative difference to the actual dimension is less than 13.6 % for the inspected crack clusters. Compensation values of 3.8 % and 4.3 % were required to be added to the original values of $\Delta Bx_{max}/Bx_0$ for crack clusters 17 and 18 respectively, greatly decreasing the pocket length prediction difference for both of the inspected crack clusters (from 24.1 % to 11.1 % and from 37.0 % to 24.7 %, respectively).

- For cluster 18, a significant difference was still observed (24.7 %) as the cluster is comprised on ‘heavy’ cracking and the determined elliptical ratio is 0.87, outside the range considered in developing the crack sizing algorithm (elliptical ratios from 1 to 1.75).

- For the crack shape examined in these clusters, the crack vertical depth was overestimated because the prediction was based on the predicted vertical angle and pocket length whilst the actual cracks showed a variation in vertical angles and pocket lengths, with the maximum crack depth not being located at the same position as the maximum crack vertical angle or pocket length.

9. Future work

Following the work carried out in the present study, further research can be continued both in modelling and experimental ways to improve the accuracy of using the ACFM probe sensor for RCF cracks characterisation in railway rails. The following are suggested for further study:

In the area of modelling of ACFM responses to RCF cracks:

- Modelling on the influences of sensor frequency in order to decide the optimized frequency that works best for sizing small surface-breaking cracks. Increase in sensor frequency will attenuate the induced magnetic field but the sensitivity and crack quantification error can be improved. The resolution of the ACFM depends on the sensor frequency, sensor geometry and how cracks distribution in the crack cluster.

- The signal sensitivity to the measurement angle (measurement line related to the crack surface opening) has discussed in section 4.4.3. The measurement line along 45° relative to the crack opening is used to determine the crack vertical angle based on the laboratory measurement, but this angle is expected to vary in the practical railway inspection due to the variation of crack horizontal angle. Initial modelling study on measurement angle shows that it is difficult to distinguish the vertical angle at small measurement angles and large measurement angles give small signal to noise ratio. An optimization study should be carried out to determine the best measurement angle or the measurement angle range for the vertical angle determination.

- The relative position between the measurement line and crack surface opening also influences the signal responses to crack dimensions. In this study the measurement line across the crack opening centre was studied but in reality this could be vary due to the non-uniformly arrangement of multiple RCF cracks. The sensitivity of the position of the measurement line in relation to the crack surface opening should be carried out numerically and should be verified by experiments.

- Establish a complete 3D railhead model (including a curved surface at the rail gauge side), to extend the current modelling, which considers a block with a flat surface (taken as the rail surface). Since RCF cracks are located near the gauge side of the rail and the curved surface can influence the ACFM signals (as the sensor cannot match completely with the curved surface), it is necessary to establish a complete railhead model to investigate how much the curved surface influences the ACFM signals.

- Include real crack shapes and more complex crack arrangements in the modelling. The present work focuses on modelling of regular cracks with semi-elliptical shapes and (mostly) uniformly sized crack clusters. Study of cracks with real shapes (obtained from progressive milling) and with real crack arrangements (as shown on the railhead sample with MPI) could be carried out to improve the ACFM prediction on RCF cracks taken from service.

- Bending and branching RCF cracks can be considered in the modelling. RCF cracks will bend and branch as they propagate into the rail (particularly after 5 mm depth). The change in propagation direction of RCF cracks will influence the detected ACFM signals and it would be beneficial to determine how well the ACFM signals could detect this. A few initial models were considered and it was found that the problem is complex as the magnetic flux path is influenced by the 3D crack shape such that under certain conditions the deeper branching crack may not be detected (preferred flux path around the sides of the crack).

In the area of experiments using the ACFM pencil probe sensor:

- Grid scanning to construct the magnetic field mapping; check the actual minimum Bx value from the mapping to see if this can eliminate the effect of shallow vertical angle on the Bx signal in the case using a single scan measurement.

- Sensor lift-off control. The ACFM measurements carried out in the study were done using a sensor lift-off of 0 mm for understanding of signal responses to crack dimensions. Measurement using different sensor lift-off values controlled by a robotic arm could be investigated, as the sensor will typically be a certain (non-zero) lift-off to the rail surface in rail inspection (particularly high speed inspection).

- More multiple RCF cracks (different dimensions and arrangements) on samples taken from service should be inspected and corresponding modelling carried out to verify the measurements made in this work (e.g. to study whether the vertical angle compensation results in increased conservatism in vertical depth prediction, as discussed in section 7.2).

- ACFM measurements on heavy and severe RCF cracks (surface length greater than 20 mm, seen in Figure 2.7). RCF cracks in the light and moderate category have been studied in the present work. ACFM responses to heavily cracking cracks should be studied and the limitation in using ACFM for sizing crack dimensions should be identified. The influence of crack asymmetry and crack branching should be investigated and related to the proposed modelling activity (for branching cracks).

References

[1] E.E. Magel. Rolling Contact Fatigue: A Comprehensive Review, No. DOT/FRA/ORD-11/24. U.S. Department of Transportation, Federal Railroad Administration. 2011.

[2] D.F. Cannon, K.O. Edel, S.L. Grassie, K. Sawley. Rail defects: an overview, Fatigue & Fracture of Engineering Materials & Structures. 2003, 26 (10): 865-886.

[3] J.E. Garnham, D.I. Fletcher, C.L. Davis, F.J. Franklin. Visualization and modelling to understand rail rolling contact fatigue cracks in three dimensions, Proceedings of the Institution of Mechanical Engineers Part F-Journal of Rail And Rapid Transit. 2011, 225 (F2): 165-178.

[4] S.L. Grassie. Rolling contact fatigue on the British railway system: treatment, Wear. 2005, 258 (7-8): 1310-1318.

[5] Innotrack report. D4.5.5-Guidelines for management of rail grinding, TIP5-CT-2006-031415. 2006.

[6] C. Mandriota, M. Nitti, N. Ancona, E. Stella, A. Distante. Filter-based feature selection for rail defect detection, Machine Vision and Applications. 2004, 15 (4): 179-185.

[7] Q. Li, S. Ren. A real-time visual inspection system for discrete surface defects of rail heads, IEEE Transactions on Instrumentation and Measurement 2012, 61 (8): 2189-2199.

[8] R. Clark. Rail flaw detection: overview and needs for future developments, NDT & E International. 2004, 37 (2): 111-118.

[9] Innotrack report, D4.4.1-Rail Inspection Technologies, TIP5-CT-2006-031415. 2008.

[10] G. Garcia, J. Zhang. Application of ultrasonic phased arrays for rail flaw inspection, DOT/FRA/ORD-06/17 U.S. Department of Transportation, Federal Railroad Administration. 2006.

[11] S. Kenderian, B.B. Djordjevic, R.E. Green. Laser based and air coupled ultrasound as noncontact and remote techniques for testing of railroad tracks, Materials Evaluation. 2002, 60 (1): 65-70.

[12] J.L. Rose, M.J. Avioli, P. Mudge, R. Sanderson. Guided wave inspection potential of defects in rail, NDT & E International. 2004, 37 (2): 153-161.

[13] H. Thomas, T. Heckel, G. Hanspach. Advantage of a combined ultrasonic and eddy current examination for railway inspection trains, Insight-Non-Destructive Testing and Condition Monitoring. 2007, 49 (6): 341-344.

[14] M.P. Papaelias, C. Roberts, C.L. Davis. A review on non-destructive evaluation of rails: state-of-the-art and future development, Proceedings of the Institution of Mechanical Engineers, Part F: Journal of Rail And Rapid Transit. 2008, 222 (4): 367-384.

[15] M. Howitt. Bombardier brings ACFM into the rail industry, Insight. 2002, 44 (6): 379-382.

[16] M.P. Papaelias, M. Lugg, C. Roberts, C. Davis. High-speed inspection of rails using ACFM techniques, NDT & E International. 2009, 42 (4): 328-335.

[17] M.P. Papaelias, C. Roberts, C.L. Davis, B. Blakeley, M. Lugg. High-speed inspection of rolling contact fatigue in rails using ACFM sensors, Insight. 2009, 51 (7): 366-369.

[18] R. Pohl, A. Erhard, H.J. Montag, H.M. Thomas, H. Wustenberg. NDT techniques for railroad wheel and gauge corner inspection, NDT & E International. 2004, 37 (2): 89-94.

[19] J.W. Ringsberg, A. Bergkvist. On propagation of short rolling contact fatigue cracks, Fatigue & Fracture of Engineering Materials & Structures. 2003, 26 (10): 969-983.

[20] G. Nicholson, C. Davis. Modelling of the response of an ACFM sensor to rail and rail wheel RCF cracks, NDT & E International. 2012, 46: 107-114.

[21] G.L. Nicholson, H. Rowshandel, X.J. Hao, C.L. Davis. Measurement and modelling of ACFM response to multiple RCF cracks in rail and wheels, Ironmaking & Steelmaking. 2013, 40 (2): 87-91.

[22] G.L. Nicholson, A.G. Kostryzhev, X.J. Hao, C.L. Davis. Modelling and experimental measurements of idealised and light-moderate RCF cracks in rails using an ACFM sensor, NDT & E International. 2011, 44 (5): 427-437.

[23] Comsol Multiphysics, 5.0 ed.

[24] M. Vidaud, W.J. Zwanenburg. Current situation on rolling contact fatigue–a rail wear phenomenon, 9th Swiss Transport Research Conference, 2009, pp. 9-11.

[25] U. Zerbst, R. Lundén, K.-O. Edel, R.A. Smith. Introduction to the damage tolerance behaviour of railway rails–a review, Engineering Fracture Mechanics. 2009, 76 (17): 2563-2601.

[26] P. Pointner. High strength rail steels-The importance of material properties in contact mechanics problems, Wear. 2008, 265 (9): 1373-1379.

[27] H. Eden, J. Garnham, C. Davis. Influential microstructural changes on rolling contact fatigue crack initiation in pearlitic rail steels, Materials Science and Technology. 2005, 21 (6): 623-629.

[28] J. Kalousek, E. Magel. Achieving a balance: the magic wear rate, Railway Track & Structures. 1997, 93 (5): 50-52.

[29] K. Sawley, R. Reiff. Rail failure assessment for the office of the rail regulator, An assessment of railtrack's methods for managing broken and defective rails. Report of the Transportation Technology Centre Pueblo, Colorado, USA. 2000.

[30] H. Ghonem, J. Kalousek. Study of surface crack initiation due to biaxial compression/shear loading, Engineering fracture mechanics. 1988, 30 (5): 667-683.

[31] K. Johnson. The mechanics of plastic deformation of surface and subsurface layers in rolling and sliding contact, Key Engineering Materials,Trans Tech Publications, 1991, pp. 17-34.

[32] E. Magel, P. Sroba, K. Sawley, J. Kalousek. Control of rolling contact fatigue of rails, Center for Surface Transportation Technology, National Research Council Canada. 2005.

[33] J. Garnham, C. Davis. Very early stage rolling contact fatigue crack growth in pearlitic rail steels, Wear. 2011, 271 (1): 100-112.

[34] V. Dikshit, P. Clayton, D. Christensen. Investigation of rolling contact fatigue in a head-hardened rail, Wear. 1991, 144 (1-2): 89-102.

[35] H. Muster, H. Schmedders, K. Wick, H. Pradier. Rail rolling contact fatigue. The performance of naturally hard and head-hardened rails in track, Wear. 1996, 191 (1): 54-64.

[36] X. Zhan, S. Wang. Research on the improvement of rail head hardening technology on railway, Proceedings of the Eastern Asia Society for Transportation Studies, 2005, pp. 263-271.

[37] Track inspector rail defect reference manual, revision 2. U.S. Department of Transportation, Federal Railroad Administration. 2015.

[38] U. Zerbst, K. Mädler, H. Hintze. Fracture mechanics in railway applications-an overview, Engineering Fracture Mechanics. 2005, 72 (2): 163-194.

[39] U. Zerbst, M. Schodel, R. Heyder. Damage tolerance investigations on rails, Engineering Fracture Mechanics. 2009, 76 (17): 2637-2653.

[40] D. Fletcher, P. Hyde, A. Kapoor. Growth of multiple rolling contact fatigue cracks driven by rail bending modelled using a boundary element technique, Proceedings of the Institution of Mechanical Engineers, Part F: Journal of Rail and Rapid Transit. 2004, 218 (3): 243-253.

[41] J. Kalousek, K. Hou, E. Magel, K. Chiddick. The benefits of friction management: a third body approach, Proceedings of the World Congress on Railway Research Conference, Colorado Springs, 1996, pp. 461-468.

[42] R. Allen. Rail defect management: British practice, Proceedings of Internationales Symposium Schienenfehler, Brandenburg, Section 14. 2000.

[43] S. Bogdański, M.W. Brown. Modelling the three-dimensional behaviour of shallow rolling contact fatigue cracks in rails, Wear. 2002, 253 (1): 17-25.

[44] D. Fletcher, P. Hyde, A. Kapoor. Modelling and full-scale trials to investigate fluid pressurisation of rolling contact fatigue cracks, Wear. 2008, 265 (9): 1317-1324.

[45] E.K. Gebretsadik, A. Johansson, B. Pålsson, M. Ekh, J. Nielsen, M. Ander, J. Brouzoulis. Simulation of wheel-rail contact and damage in switches and crossings, Wear. 2011, 271 (1): 472-481.

[46] J.W. Ringsberg, T. Lindbäck. Rolling contact fatigue analysis of rails inculding numerical simulations of the rail manufacturing process and repeated wheel-rail contact loads, International Journal of Fatigue. 2003, 25 (6): 547-558.

[47] K.L. Johnson. Contact mechanics, Cambridge University Press, 1987.

[48] A.A. Shabana, K.E. Zaazaa, H. Sugiyama. Railroad vehicle dynamics: a computational approach, CRC press, 2007.

[49] A. Kapoor, F. Franklin, S. Wong, M. Ishida. Surface roughness and plastic flow in rail wheel contact, Wear. 2002, 253 (1): 257-264.

[50] M. Dembosky, A. Doherty, C. Urban, R. Walker, S. Gurule. Management of rolling contact fatigue (RCF) in the UK system: a systems solution, Proceedings of 7th World Congress on Railway Research, Montreal, Canada, 2006.

[51] M. Burstow. A model to predict and understand rolling contact fatigue in wheels and rails, Proceedings of the 7th World Congress on Railway Research (WCRR 2006), Montreal, Canada, 2006.

[52] J. Evans, M. Burstow. Vehicle/track interaction and rolling contact fatigue in rails in the UK, Vehicle System Dynamics. 2006, 44 (sup1): 708-717.

[53] G. Schleinzer, F. Fischer. Residual stresses in new rails, Materials Science and Engineering: A. 2000, 288 (2): 280-283.

[54] G. Schleinzer, F. Fischer. Residual stress formation during the roller straightening of railway rails, International Journal of Mechanical Sciences. 2001, 43 (10): 2281-2295.

[55] P. Webster, G. Mills, X. Wang, W. Kang, T. Holden. Residual stresses in alumino-thermic welded rails, The Journal of Strain Analysis for Engineering Design. 1997, 32 (6): 389-400.

[56] A. Skyttebol, L. Josefson. Numerical Simulation of Flash Butt Welding of Railway Rails, Chalmers tekniska högsk., 2004.

[57] A. Skyttebol. Continuous welded railway rails: Residual stress analyses, fatigue assessments and experiments, Chalmers University of Technology, 2004.

[58] A. Skyttebol, B. Josefson, J. Ringsberg. Fatigue crack growth in a welded rail under the influence of residual stresses, Engineering Fracture Mechanics. 2005, 72 (2): 271-285.

[59] T.S. Jun, F. Hofmann, J. Belnoue, X. Song, M. Hofmann, A.M. Korsunsky. Triaxial residual strains in a railway rail measured by neutron diffraction, Journal of Strain Analysis for Engineering Design. 2009, 44 (7): 563-568.

[60] T. Sasaki, S. Takahashi, Y. Kanematsu, Y. Satoh, K. Iwafuchi, M. Ishida, Y. Morii. Measurement of residual stresses in rails by neutron diffraction, Wear. 2008, 265 (9-10): 1402-1407.

[61] S. Srimani, J. Basu. An investigation for control of residual stress in roller-straightened rails, The Journal of Strain Analysis for Engineering Design. 2003, 38 (3): 261-268.

[62] Annual Return 2015, Network Rail. 2015.

[63] S. Kumar. Study of rail breaks: associated risks and maintenance strategies, Department of Civil and Environmental Engieering, Luleå Railway Research Center 2006.

[64] S. Kaewunruen, M. Ishida, S. Marich. Dynamic Wheel–Rail Interaction Over Rail Squat Defects, Acoustics Australia. 2015, 43 (1): 97-107.

[65] S. Pal, W.J. Daniel, M. Farjoo. Early stages of rail squat formation and the role of a white etching layer, International Journal of Fatigue. 2013, 52: 144-156.

[66] S. Pal, C. Valente, W. Daniel, M. Farjoo. Metallurgical and physical understanding of rail squat initiation and propagation, Wear. 2012, 284: 30-42.

[67] S.L. Grassie, D.I. Fletcher, E.G. Hernandez, P. Summers. Studs: a squat-type defect in rails, Proceedings of the Institution of Mechanical Engineers, Part F: Journal of Rail and Rapid Transit. 2011: 0954409711421462.

[68] S. Simon, A. Saulot, C. Dayot, X. Quost, Y. Berthier. Tribological characterization of rail squat defects, Wear. 2013, 297 (1): 926-942.

[69] S. Grassie. Squats and squat-type defects in rails: the understanding to date, Proceedings of the Institution of Mechanical Engineers, Part F: Journal of Rail and Rapid Transit. 2012, 226 (3): 235-242.

[70] Railtrack. Permanent way special instruction No. 4, Issue 2, 2002.

[71] D. Fletcher, A. Kapoor. Rapid method of stress intensity factor calculation for semi-elliptical surface breaking cracks under three-dimensional contact loading, Proceedings of the Institution of Mechanical Engineers, Part F: Journal of Rail and Rapid Transit. 2006, 220 (3): 219-234.

[72] M. Kaneta, Y. Murakami. Propagation of semi-elliptical surface cracks in lubricated rolling/sliding elliptical contacts, Journal of Tribology. 1991, 113 (2): 270-275.

[73] K.S. Eric Magel. Rail Surface Condition Alert – stage 1: Evaluation and calibration of surface crack measuring devices, CSTT-RYV-CAT-090. Centre for Surface Transportation Technology, National Research Council Canada. 2006.

[74] G. Girsch, R. Heyder. Advanced pearlitic and bainitic high strength rails promise to improve rolling contact fatigue resistance, 7th World Congress on Railway Research (WCRR2006), Montreal, Canada. 2006.

[75] R. Heyder, G. Girsch. Testing of HSH® rails in high-speed tracks to minimise rail damage, Wear. 2005, 258 (7): 1014-1021.

[76] S. Sawadisavi. Machine-vision inspection of railroad track,University of Illinois at Urbana-Champaign, 2009.

[77] E. Deutschl, C. Gasser, A. Niel, J. Werschonig. Defect detection on rail surfaces by a vision based system, Intelligent Vehicles Symposium, 2004 IEEE,IEEE, 2004, pp. 507-511.

[78] P. De Ruvo, E. Stella, A. Distante, M. Nitti, F. Marino. A Real Time Visual Inspection System for Railway Maintenance: Automatic Rail Detection and Tracking, The Open Cybernetics & Systemics Journal. 2008, 2: 57-67.

[79] F. Marino, A. Distante, P.L. Mazzeo, E. Stella. A real-time visual inspection system for railway maintenance: Automatic hexagonal-headed bolts detection, IEEE Transactions on Systems Man and Cybernetics Part C-Applications and Reviews. 2007, 37 (3): 418-428.

[80] L. Jie, L. Siwei, L. Qingyong, Z. Hanqing, R. Shengwei. Real-time rail head surface defect detection: A geometrical approach, 2009 IEEE International Symposium on Industrial Electronics. 2009: 769-774.

[81] M. Singh, S. Singh, J. Jaiswal, J. Hempshall. Autonomous rail track inspection using vision based system, Proceedings of the 2006 IEEE International Conference on Computational Intelligence for Homeland Security and Personal Safety, 2006, pp. 56-59.

[82] P. Babenko. Visual inspection of railroad tracks,Citeseer, 2009.

[83] E. Resendiz, J.M. Hart, N. Ahuja. Automated visual inspection of railroad tracks, IEEE Transactions on Intelligent Transportation Systems. 2013, 14 (2): 751-760.

[84] P.E. Mix. Introduction to nondestructive testing: a training guide, John Wiley & Sons, 2005.

[85] Innotrack report, D4.4.2-Operational evaluation of an inspection demonstrator (phase 1: laboratory and static tests), TIP5-CT-2006-031415. 2009.

[86] D. Bray. Detection of flaws in used railroad rail by ultrasonic inspection techniques, NDT International. 1979, 12 (5): 217-223.

[87] Olympus NDT, Advances in Phased Array ultrasonic technology applications, Olympus NDT, 2007.

[88] F. Lanza di Scalea, P. Rizzo, S. Coccia, I. Bartoli, M. Fateh, E. Viola, G. Pascale. Non-contact ultrasonic inspection of rails and signal processing for automatic defect detection and classification, Insight-Non-Destructive Testing and Condition Monitoring. 2005, 47 (6): 346-353.

[89] J.L. Rose, Y. Cho. A guided wave approach to defect detection under shelling in rail, NDT & E International. 2009, 42 (3): 174-180.

[90] P. Cawley, M. Lowe, D. Alleyne, B. Pavlakovic, P. Wilcox. Practical long range guided wave inspection-applications to pipes and rail, Materials Evaluation. 2003, 61 (1): 66-74.

[91] R.S. Edwards, C. Holmes, Y. Fan, M. Papaelias, S. Dixon, C.L. Davis, B.W. Drinkwater, C. Roberts. Ultrasonic detection of surface-breaking railhead defects, Insight. 2008, 50 (7): 369-373.

[92] Y. Fan, S. Dixon, R.S. Edwards, X. Jian. Ultrasonic surface wave propagation and interaction with surface defects on rail track head, NDT & E International. 2007, 40 (6): 471-477.

[93] R.S. Edwards, S. Dixon, X. Jian. Characterisation of defects in the railhead using ultrasonic surface waves, NDT & E International. 2006, 39 (6): 468-475.

[94] A. Chabhaz, M. Brassard, A. Pelletier. Mobile inspection system for rail integrity assessment, Proceedings of the 15th World Conference of Non-Destructive Testing, Roma, Italy. 2000.

[95] M. Rosli, R.S. Edwards, Y. Fan. In-plane and out-of-plane measurements of Rayleigh waves using EMATs for characterising surface cracks, NDT & E International. 2012, 49: 1-9.

[96] S. Kenderian, D. Cerniglia, B.B. Djordjevic, G. Garcia, S. JIAN, M. Snell. Rail track field testing using laser/air hybrid ultrasonic technique, Materials Evaluation. 2003, 61 (10): 1129-1133.

[97] S. Kenderian, B.B. Djordjevic, D. Cerniglia, G. Garcia. Dynamic railroad inspection using the laser-air hybrid ultrasonic technique, Insight-Non-Destructive Testing and Condition Monitoring. 2006, 48 (6): 336-341.

[98] N.A. Thakkar, J.A. Steel, R. Reuben, G. Knabe, D. Dixon, R. Shanks. Monitoring of rail-wheel interaction using acoustic emission (AE), Advanced Materials Research. 2006, 13: 161-168.

[99] A.A. Pollock. Loading and stress in acoustic emission testing, Materials evaluation. 2004, 62 (3): 326-333.

[100] A.G. Kostryzhev, C.L. Davis, C. Roberts. Detection of crack growth in rail steel using acoustic emission, Ironmaking & Steelmaking. 2013, 40 (2): 98-102.

[101] P. Yılmazer, A. Amini, M. Papaelias. The structural health condition monitoring of rail steel using acoustic emission techniques,University of Birmingham, 2012.

[102] N.A. Thakkar. Monitoring of rail/wheel interaction using acoustic emission,Heriot-Watt University, 2009.

[103] N. Craven, O.G. Bewes, B.A. Fenech, R. Jones. Responding to the Environmental Noise Directive by demonstrating the benefits of rail grinding on the Great Britain's railway network, Proceedings of the Institution of Mechanical Engineers, Part F: Journal of Rail and Rapid Transit. 2013: 0954409713494948.

[104] M. Papaelias, A. Amini, Z. Huang, P. Vallely, D.C. Dias, S. Kerkyras. Online condition monitoring of rolling stock wheels and axle bearings, Proceedings of the Institution of Mechanical Engineers, Part F: Journal of Rail and Rapid Transit. 2014: 0954409714559758.

[105] A. Amini, M. Entezami, M. Papaelias. Onboard detection of railway axle bearing defects using envelope analysis of high frequency acoustic emission signals, Case Studies in Nondestructive Testing and Evaluation. 2016.

[106] D. Jiles. Review of magnetic methods for nondestructive evaluation (Part 2), NDT International. 1990, 23 (2): 83-92.

[107] Y. Li, G.Y. Tian, S. Ward. Numerical simulation on magnetic flux leakage evaluation at high speed, NDT & E International. 2006, 39 (5): 367-373.

[108] Y. Li, J. Wilson, G.Y. Tian. Experiment and simulation study of 3D magnetic field sensing for magnetic flux leakage defect characterisation, NDT & E International. 2007, 40 (2): 179-184.

[109] J. García-Martín, J. Gómez-Gil, E. Vázquez-Sánchez. Non-destructive techniques based on eddy current testing, Sensors. 2011, 11 (3): 2525-2565.

[110] L. Oukhellou, P. Aknin, J.-P. Perrin. Dedicated sensor and classifier of rail head defects, Control Engineering Practice. 1999, 7 (1): 57-61.

[111] M. Bentoumi, P. Aknin, G. Bloch. On-line rail defect diagnosis with differential eddy current probes and specific detection processing, European Physical Journal-Applied Physics. 2003, 23 (3): 227-233.

[112] H.-M. Thomas, M. Junger, H. Hintze, R. Krull, S. Rühe. Pioneering inspection of railroad rails with eddy currents, 15th World Conference on Non-Destructive Testing, Roma, Italy. 2000.

[113] R. Pohl, R. Krull, R. Meierhofer. A new eddy current instrument in a grinding train, 9th European Conference on NDT, Berlin, Germany. 2006.

[114] R. Krull, H. Hintze, M. Thomas, R. Pohl, S. RUHE. Eddy-current detection of head checks on the gauge corners of rails: Recent results, Proceedings of the International Conference and Exhibition Railway Engineering, London, UK. 2003.

[115] R. Meierhofer, R. Pohl. Head check measurement–a fully-operational system on a rail grinder, Proceedings of World Congress on Railway Research, Montreal, Canada. 2006.

[116] S. Burke. Crack depth measurement using eddy-current NDE, Non Destructive Testing Australia. 2002, 39 (1): 18-22.

[117] A. Lewis, D. Michael, M.C. Lugg, R. Collins. Thin‐skin electromagnetic fields around surface‐breaking cracks in metals, Journal of Applied Physics. 1988, 64 (8): 3777-3784.

[118] M. Lugg, D. Topp, M. Keynes. Recent developments and applications of the ACFM inspection method and ACSM stress measurement method, Proceedings of ECNDT. 2006.

[119] D. Topp, M. Smith. Application of the ACFM inspection method to rail and rail vehicles, Insight. 2005, 47 (6): 354-357.

[120] M.P. Papaelias, C. Roberts, C.L. Davis, M. Lugg, M. Smith. Detection and quantification in rails using ACFM technology, Insight. 2008, 50 (7): 364-368.

[121] L. Martin. The First 20 years of the AC field Measurement Technique, 17th World Conference on Non-Destructive Testing, Shanghai, China. 2008.

[122] W.D. Dover, C.C. Monahan. The Measurement of Surface-Breaking Cracks by the Electrical Systems Acpd/Acfm, Fatigue & Fracture Of Engineering Materials & Structures. 1994, 17 (12): 1485-1492.

[123] A. Raine, M. Lugg. A review of the alternating current field measurement inspection technique, Sensor Review. 1999, 19 (3): 207-213.

[124] F.C.R. Marques, M.V.M. Martins, D.A. Topp. Experiences in the use of ACFM for offshore platform inspection in Brazil, Insight. 2001, 43 (6): 394-398.

[125] J. Zhou, B. Wong, G. Seet. An ACFM Automated Crack Detection System Deployed By An Underwater Roving Vehicle, Journal of Nondestructive Testing. 2003, 8 (9): 1-6.

[126] D. Clifton, F. Mill, J. Esnaola, R. Kare, W.D. Dover. Diverless weld inspection and repair using ECM/ACFM techniques, Underwater Technology. 2000, 24 (4): 131-141.

[127] W. Dover, S. Dharmavasan, D. Topp, M. Lugg. Fitness for purpose using ACFM for crack detection and sizing and FACTS/FADS for analysis, Marine Structural Inspection, Maintenance, and Monitoring Symposium. 1991.

[128] W. Li, G.M. Chen, C.R. Zhang, T. Liu. Simulation analysis and experimental study of defect detection underwater by ACFM probe, China Ocean Engineering. 2013, 27 (2): 277-282.

[129] D.A. Topp, J.F. Burd, J.W. Martin, M. Lorenz. Use of the ACFM inspection method to reduce downhole drillstring failures, presented at Australia Oil & Gas Conference, 2001.

[130] M.J. Knight, F.P. Brennan, W.D. Dover. Effect of residual stress on ACFM crack measurements in drill collar threaded connections, NDT & E International. 2004, 37 (5): 337-343.

[131] M. Smith, R. Sutherby. The detection of pipeline SCC flaws using the ACFM technique, Insight. 2005, 47 (12): 765-768.

[132] W. Li, X.a. Yuan, G. Chen, X. Yin, J. Ge. A feed-through ACFM probe with sensor array for pipe string cracks inspection, NDT & E International. 2014, 67: 17-23.

[133] T.P. Sattar, H.L. Rodriguez, J. Shang, B. Bridge. Automated NDT of floating production storage oil tanks with a swimming and climbing robot, Climbing and Walking Robots, Springer Berlin Heidelberg. 2006: 935-942.

[134] M.P. Papaelias, C. Roberts, C. Davis, M. Lugg, M. Smith. Detection and quantification of rail contact fatigue cracks in rails using ACFM technology, Insight-Non-Destructive Testing and Condition Monitoring. 2008, 50 (7): 364-368.

[135] M. Papaelias, M. Lugg. Detection and evaluation of rail surface defects using alternating current field measurement techniques, Proceedings of the Institution of Mechanical Engineers, Part F: Journal of Rail and Rapid Transit. 2012: 0954409712444840.

[136] M.P. Papaelias, M.C. Lugg, C. Roberts, C.L. Davis. High-speed inspection of rails using ACFM techniques, NDT & E International. 2009, 42 (4): 328-335.

[137] H. Rowshandel, G.L. Nicholson, C.L. Davis, C. Roberts. A robotic approach for NDT of RCF cracks in rails using an ACFM sensor, Insight. 2011, 53 (7): 368-376.

[138] H. Rowshandel, G.L. Nicholson, C.L. Davis, C. Roberts. An integrated robotic system for automatic detection and characterisation of rolling contact fatigue cracks in rails using an alternating current field measurement sensor, Proceedings of the Institution of Mechanical Engineers, Part F: Journal of Rail and Rapid Transit. 2013: 0954409713486778.

[139] H. Rowshandel, M. Papaelias, C. Roberts, C. Davis. Development of autonomous ACFM rail inspection techniques, Insight. 2011, 53 (2): 85-89.

[140] H. Rowshandel. The development of an autonomous robotic inspection system to detect and characterise rolling contact fatigue cracks in railway track,University of Birmingham, 2014.

[141] D. Mirshekar-Syahkal, R.F. Mostafavi. 1-D probe array for ACFM inspection of large metal plates, IEEE Transactions on Instrumentation and Measurement. 2002, 51 (2): 374-382.

[142] C. Guo-ming, L. Wei, W. Ze-Xin. Structural optimization of 2-D array probe for alternating current field measurement, NDT & E International. 2007, 40 (6): 455-461.

[143] S. Sadeghi, D. Mirshekar-Syahkal. A Combined ACFM-SMFM System for Real-Time Detection and Sizing of Surface Cracks in Metals, Review of progress in quantitative nondestructive evaluation, Springer US. 1991: 2113-2120.

[144] R. Kare. Crack Monitoring Using ACFM, Fracture of Nano and Engineering Materials and Structures, Springer Netherlands2006, pp. 1021-1022.

[145] C. Low, B. Wong. Defect evaluation using the alternating current field measurement technique, Insight-Non-Destructive Testing and Condition Monitoring. 2004, 46 (10): 598-605.

[146] B. Blakeley, M. Lugg. Application of ACFM for inspection through metal coatings, Insight. 2010, 52 (6): 310-315.

[147] W. Li, G.M. Chen, X.K. Yin, C.R. Zhang, T. Liu. Analysis of the lift-off effect of a U-shaped ACFM system, NDT & E International. 2013, 53: 31-35.

[148] W. Li, G.M. Chen, W.Y. Li, Z. Li, F. Liu. Analysis of the inducing frequency of a U-shaped ACFM system, NDT & E International. 2011, 44 (3): 324-328.

[149] J.M.C. Munoz, F.P.G. Marquez, M. Papaelias. Railroad inspection based on ACFM employing a non-uniform B-spline approach, Mechanical Systems and Signal Processing. 2013, 40 (2): 605-617.

[150] A. Noroozi, R.P.R. Hasanzadeh, M. Ravan. A fuzzy learning approach for identification of arbitrary crack profiles using ACFM technique, IEEE Transactions on Magnetics. 2013, 49 (9): 5016-5027.

[151] G.L.N. H. Rowshandel, C.L. Davis. Characterisation of Clustered Rolling Contact Fatigue Cracks in Rails using a Machine Learning Approach.

[152] D. Michael, A. Lewis, M. McIver, R. Collins. Thin-skin electromagnetic fields in the neighbourhood of surface-breaking cracks in metals, Proceedings of the Royal Society of London A: Mathematical, Physical and Engineering Sciences, The Royal Society. 1991, 434 (1892): 587-603.

[153] S. Sadeghi, D.M. Syahkal. Surface potential distributions due to eddy currents around long cracks in metals, induced by U-shaped current-carrying wires, IEEE Transactions on Magnetics. 1991, 27 (1): 674-679.

[154] R.F. Mostafavi, D. Mirshekar-Syahkal. AC fields around short cracks in metals induced by rectangular coils, IEEE Transactions on Magnetics. 1999, 35 (3): 2001-2006.

[155] S. Thompson, B. Tanner. The magnetic properties of pearlitic steels as a function of carbon content, Journal of Magnetism and Magnetic Materials. 1993, 123 (3): 283-298.

[156] G. Nicholson, H. Rowshandel, M. Papaelias, C. Davis, C. Roberts. Sizing and tomography of rolling contact fatigue cracks in rails using NDT technology-potential for high speed application, Proceeding of the 9th World Conference on Railway Research, Lille, France. 2011.

[157] R. Collins. The development of the ACPD and ACFM techniques at UCL, Nondestructive Testing of Materials. 1995, 8: 65-74.

[158] T. Liou, C. Hsiao, C.-C. Cheng, N. Chang. Depth measurement of notches as models for shallow cracks in concrete, NDT & E International. 2009, 42 (1): 69-76.

[159] R.S. Edwards, C. Holmes, Y. Fan, M. Papaelias, S. Dixon, C. Davis, B. Drinkwater, C. Roberts. Ultrasonic detection of surface-breaking railhead defects, Insight-Non-Destructive Testing and Condition Monitoring. 2008, 50 (7): 369-373.

[160] J. Wang, N. Yusa, H. Pan, M. Kemppainen, I. Virkkunen, H. Hashizume. Discussion on modeling of thermal fatigue cracks in numerical simulation based on eddy current signals, NDT & E International. 2013, 55: 96-101.

[161] S. Baby, T. Balasubramanian, R. Pardikar, M. Palaniappan, R. Subbaratnam. Time-of-flight diffraction (TOFD) technique for accurate sizing of surface-breaking cracks, Insight-Non-Destructive Testing and Condition Monitoring. 2003, 45 (6): 426-430.

[162] M. Silk, B. Lidington. The potential of scattered or diffracted ultrasound in the determination of crack depth, Non-destructive Testing. 1975, 8 (3): 146-151.

[163] V.K. Kinra, B.Q. Vu. Diffraction of Rayleigh waves in a half‐space. II. Inclined edge crack, The Journal of the Acoustical Society of America. 1986, 79 (6): 1688-1692.

[164] B. Dutton, A. Clough, M. Rosli, R.S. Edwards. Non-contact ultrasonic detection of angled surface defects, NDT & E International. 2011, 44 (4): 353-360.

[165] M.V. Felice, A. Velichko, P.D. Wilcox. Accurate depth measurement of small surface-breaking cracks using an ultrasonic array post-processing technique, NDT & E International. 2014.

[166] M. Ravan, S. Sadeghi, R. Moini. Using a wavelet network for reconstruction of fatigue crack depth profile from AC field measurement signals, NDT & E International. 2007, 40 (7): 537-544.